

Approved for public release,
distribution unlimited

Air Force Office of Scientific Research

Project Monitor: Capt. Charles H. Ward, Ph.D.

COMBUSTION SYNTHESIS OF NIOBIUM INTERMETALLICS AND COMPOSITES

Final Report

Period Cover: April 1, 1995- March 30, 1996

J. A. Sekhar, G. K. Dey, D. Carr, and V. Gupta

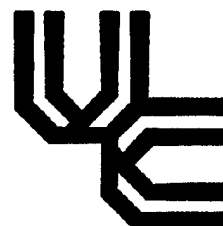
International Center for Micropyrretics
Department of Materials Science and Engineering
University of Cincinnati
Cincinnati, Ohio 45221-0012

Telephone: (513) 556-3105 Fax: (513) 556-2653

AIR FORCE OF THE UNITED STATES
NOTICE OF
This card
approves
1st
3000000000
STIMMO Program

10

DTIC QUALITY INSPECTED 2



19971003 042

REPORT DOCUMENTATION PAGE

Form Approved
OMB No. 0704-0188

Public reporting burden for this collection of information is estimated to average 1 hour per response, including the time for reviewing instructions, searching existing data sources, gathering and maintaining the data needed, and completing and reviewing the collection of information. Send comments regarding this burden estimate or any other aspect of this collection of information, including suggestions for reducing this burden, to Washington Headquarters Services, Directorate for Information Operations and Reports, 1215 Jefferson Davis Highway, Suite 1204, Arlington, VA 22202-4302, and to the Office of Management and Budget, Paperwork Reduction Project (0704-0188), Washington, DC 20503.

| | | | | |
|---|--|---|---|--|
| 1. AGENCY USE ONLY (Leave blank) | | 2. REPORT DATE April 1, 1997 | 3. REPORT TYPE AND DATES COVERED Final 04/01/95 - 03/30/96 | |
| 4. TITLE AND SUBTITLE COMBUSTION SYNTHESIS OF NIOBIUM INTERMETALLICS AND COMPOSITES | | | 5. FUNDING NUMBERS AFOSR-F49620-93-1-0200 | |
| 6. AUTHOR(S) J. A. Sekhar, G. K. Dey, D. Carr and V. Gupta | | | | |
| 7. PERFORMING ORGANIZATION NAME(S) AND ADDRESS(ES) International Center for Micropyretics Contact: Professor J. A. Sekhar Department of Materials Science and Engineering University of Cincinnati P.O. Box 210012 412B Rhodes Hall Cincinnati, OH 45221-0012 | | | 8. PERFORMING ORGANIZATION REPORT NUMBER ICM-037 | |
| 9. SPONSORING/MONITORING AGENCY NAME(S) AND ADDRESS(ES) Air Force Office of Scientific Research Capt. C. H. Ward, AFOSR/INC 110 Duncan Avenue, Bolling AFB, DC 20332-001 | | | 10. SPONSORING/MONITORING AGENCY REPORT NUMBER | |
| 11. SUPPLEMENTARY NOTES This report contains work on Nickel Aluminide composites made by Micropyretic Synthesis. | | | | |
| 12a. DISTRIBUTION/AVAILABILITY STATEMENT Approved for public release, distribution unlimited | | | 12b. DISTRIBUTION CODE | |
| 13. ABSTRACT This report describes studies carried out on the various aspects of micropyretic synthesis on Ni and Nb aluminides. The effect of process parameters like compaction pressure, diluents, preheat temperature, and particle size on the process and on the synthesized product have been examined theoretically as well as experimentally. Models have been developed to explain the effect of the aforementioned process variables on the synthesis process by postulating on the mechanism of the process. A good agreement had been found between model predictions and the observed experimental results. Micropyretic synthesis is a process in which alloying occurs at a local level at a very rapid rate. In a process of this nature, the homogeneity of the resulting microstructure in terms of phase content and composition is important. Despite the fact that homogeneity of the microstructure is important in products made by this process, no many studies have been carried out to examine this aspect. In this report, the synthesized microstructure has been examined by detailed electron microscopy. One of the highlights of the study is the result of that the compositional and microstructural homogeneity of the micropyretically synthesized product is unusually uniform, thus establishing the process as potentially useful for aircraft alloys. Continued on next page. | | | | |
| 14. SUBJECT TERMS Micropyretic Synthesis, Nickel Aluminide, Processing Maps | | | 15. NUMBER OF PAGES 125 Pages | |
| | | | 16. PRICE CODE | |
| 17. SECURITY CLASSIFICATION OF REPORT UNCLASSIFIED | 18. SECURITY CLASSIFICATION OF THIS PAGE UNCLASSIFIED | 19. SECURITY CLASSIFICATION OF ABSTRACT UNCLASSIFIED | 20. LIMITATION OF ABSTRACT | |

Abstract continued.

The fabrication of NiAl with better mechanical properties by the process of micropyretic synthesis has been attempted. A large number of alloying additions have been made in order to develop a tough alloy. NiAl when alloyed with Fe, Cr and V has been found to show considerable improvement in fracture toughness. Improvement in fracture toughness has been found in the case of NiAl alloyed with Ti and Nb. The effect of a second combustion reaction on the synthesis process and the microstructure has been examined in the case of NiAl alloyed with Ti and B.

The mechanism of synthesis of the alloys from elemental powders in micropyretic synthesis has been examined in great detail. An attempt has been made to study the mechanism of the micropyretic synthesis of the multicomponent alloys by arresting the combustion front. A detailed microstructural study has been carried out around frozen combustion front in order to establish the sequence of formation of the product phase from elemental powders. These studies have been carried out in the case of NiAl and Nb₄₅Ti₄₀Al₁₅.

The report thus delves into the entire spectrum of aspects associated with the process of micropyretic synthesis of intermetallic compounds. It deals with the effect of process variables, theoretical study of the process, examination of mechanism of synthesis, property evaluation and examination of the microstructure.

*This report contains information
on Nickel Aluminides*

Abstract

This report describes studies carried out on the various aspects of micropyretic synthesis on Ni and Nb aluminides. The effect of process parameters like compaction pressure, diluents, preheat temperature, and particle size on the process and on the synthesized product have been examined theoretically as well as experimentally. Models have been developed to explain the effect of the aforementioned process variables on the synthesis process by postulating on the mechanism of the process. A good agreement has been found between model predictions and the observed experimental results.

Micropyretic synthesis is a process in which alloying occurs at a local level at a very rapid rate. In a process of this nature, the homogeneity of the resulting microstructure in terms of phase content and composition is important. Despite the fact that homogeneity of the microstructure is important in products made by this process, not many studies have been conducted to examine this aspect. In this report, the synthesized microstructure has been examined by detailed electron microscopy. One of the highlights of the study is the result that the compositional and microstructural homogeneity of the micropyretically synthesized product is unusually uniform, thus establishing the process as potentially useful for aircraft alloys.

The fabrication of NiAl with better mechanical properties by the process of micropyretic synthesis has been attempted. A large number of alloying additions have been made in order to develop a tough alloy. NiAl when alloyed with Fe, Cr and V has been found to show considerable improvement in fracture toughness. Improvement in fracture toughness has been found in the case of NiAl alloyed with Ti and Nb. The effect of a second combustion reaction on the synthesis process and the microstructure has been examined in the case of NiAl alloyed with Ti and B.

The mechanism of synthesis of the alloys from elemental powders in micropyretic synthesis has been examined in great detail. An attempt has

been made to study the mechanism of the micropyretic synthesis of the multicomponent alloys by arresting the combustion front. A detailed microstructural study has been conducted around frozen combustion front in order to establish the sequence of formation of the product phase from elemental powders. These studies have been carried out in the case of NiAl and $\text{Nb}_{45}\text{Ti}_{40}\text{Al}_{15}$.

The report thus delves into the entire spectrum of aspects associated with the process of micropyretic synthesis of intermetallic compounds. It deals with the effect of process variables, theoretical study of the process, examination of mechanism of synthesis, property evaluation and examination of the microstructure.

Table of Contents

| | |
|--|------------|
| <i>Abstract</i> | <i>i</i> |
| <i>Table of Contents</i> | <i>iii</i> |
| <i>List of Figures</i> | <i>vi</i> |
| <i>List of Tables</i> | <i>xii</i> |
| I. Introduction | 1 |
| I. 2 MICROPYRETIC SYNTHESIS PROCESS | 3 |
| I. 2. 1 Underlying Principles | 3 |
| I. 2. 2 Ignition and Combustion | 7 |
| I. 2. 4 Processing Variables | 10 |
| I. 2. 5 Applications | 11 |
| I. 3 MICROPYRETIC SYNTHESIS OF INTERMETALLIC COMPOUNDS | 12 |
| II. The Effect of Different Process Parameters on the Synthesis Process | 14 |
| II. 1 Effect of particle size | 14 |
| II. 2 Relationship Between Combustion Parameters and Dimensional Changes | 19 |
| II. 3 Numerical Models | 26 |
| II. 4 Processing Maps | 28 |
| II. 5 Conclusions | 29 |
| III. Fabrication of Tough NiAl | 33 |
| III. 1 Introduction | 33 |
| III. 2 Experimental | 35 |
| III. 3 Results and Discussions | 38 |
| III. 3. 1 Density and Porosity | 38 |
| III. 3. 2 Mechanical Properties | 39 |

| | |
|--|-----------|
| III. 3. 3 Microstructure of Specimens Synthesized without Preheat | 42 |
| III. 3. 3. 1 Microstructure before Deformation | 42 |
| III. 3. 3. 2 Microstructure after Deformation | 46 |
| III. 3. 4 The effect of Preheat | 48 |
| III. 3. 5 Effect of Diluents and Effect of Particle Size | 58 |
| III. 4 Conclusions | 61 |
| IV. Micropyretic Synthesis of NiAlTiB alloys | 62 |
| IV. 1 Introduction | 62 |
| IV. 2 Experimental | 63 |
| IV. 3 Results and Discussions | 64 |
| IV. 3. 1 Effect Of Ti and B on the Combustion Process | 64 |
| IV. 3. 2 Microstructures and Phases | 65 |
| IV. 3. 2. 1 Microstructure without preheat | 66 |
| IV. 3. 2. 1. 1 X-ray diffraction results | 66 |
| IV. 3. 2. 1. 2 Microstrutural Examination | 67 |
| IV. 3. 2. 2 The Effect of Preheating on the Microstructure and Nature of the Phases | 68 |
| IV. 3. 2. 2. 1 X-ray diffraction results | 68 |
| IV. 3. 2. 2. 2 Microstructure of the Preheated Specimen | 69 |
| IV. 3. 3 Fractography | 70 |
| IV. 4 Conclusions | 72 |
| V. Micropyretic Synthesis of NiAlTiNb alloys | 73 |
| V. 1 Introduction | 73 |
| V. 2 Experimental | 75 |
| V. 3 Results and Discussions | 77 |
| V. 3. 1 Combustibility of the alloys | 77 |

| | |
|---|------------|
| V. 3. 2 Phases and microstructures | 78 |
| V. 3. 2. 1 X-ray diffraction results | 78 |
| V. 3. 2. 2 Microstructures | 80 |
| V. 3. 3 Fracture toughness | 82 |
| V. 3. 4 Fracture Behavior | 84 |
| V. 3. 5 Oxidation Behavior of the Alloys | 86 |
| V. 4 Conclusions | 87 |
| VI. Mechanism of Synthesis | 88 |
| VI. 1 Introduction | 88 |
| VI. 2 Experimental | 89 |
| VI. 3 Results and Discussions | 90 |
| VI. 3. 1 Mechanism of synthesis of NiAl | 90 |
| VI. 3. 2 Mechanism of synthesis of Nb ₄₅ Al ₁₅ Ti ₄₀ | 100 |
| VI. 4 Conclusions | 106 |
| VII. References | 107 |

List of Figures

Fig. I. 1 Schematic diagram of a typical micropyretic synthesis process.

Fig. I. 2 A representation of the adiabatic temperature calculation for the synthesis of MoSi_2 from its elements.

Fig. II. 2 Effect of the compaction pressure on the initial porosity of the unreacted green compact.

Fig. II. 3 Dependence of the longitudinal elongation on the compaction pressure for various initial temperatures of the unreacted specimens. (a) Ni + 50 at.% Al composition and (b) Ti + 50 at.% C, Ni + 25 at.% Al, and Ni + 75 at.% Al compositions.

Fig. II. 4 Processing map for green porosity as a function of the compaction pressure (in MNm^{-2}) and the Si content (in wt%). The constants in the map are the Ni, Al and Si particle sizes, which are -100 mesh, -325 mesh and -325 mesh respectively. The processing for all the compositions is carried out at room temperature, without any preheating.

Fig. II. 5 Processing map for combustion velocity as a function of the compaction pressure (in MNm^{-2}) and the Si content (in wt%). The constants in the map are the Ni, Al and Si particle sizes, which are -100 mesh, -325 mesh and -325 mesh respectively. The processing for all the compositions is carried out at room temperature, without any preheating.

Fig. II. 6 Processing map for final porosity as a function of the compaction pressure (in MNm^{-2}) and the Si content (in wt%). The constants in the map are the Ni, Al and Si particle sizes, which are -100 mesh, -325 mesh and -325

mesh respectively. The processing for all the compositions is carried out at room temperature, without any preheating.

Fig. II. 7 Processing map for knoop hardness as a function of the compaction pressure (in MNm^{-2}) and the Si content (in wt%). The constants in the map are the Ni, Al and Si particle sizes, which are -100 mesh, -325 mesh and -325 mesh respectively. The processing for all the compositions is carried out at room temperature, without any preheating.

Fig. III. 1 Schematic diagram of the set up used for micropyretic synthesis in inert atmosphere. The different components of the set up are 1. quartz tube 2. alumina boat 3. induction coil 4. thermocouples 5. specimen.

Fig. III. 2 Optical microstructure of the alloy 3 after synthesis without preheat.

Fig. III. 3 Bright field micrograph showing the arrangement of dislocations in the alloy 3 synthesized without preheat. Dislocations with $b=\langle 100 \rangle$ and $b=\langle 111 \rangle$ can be seen.

Fig. III. 4 (a) EDS spectrum from the grain interior and (b) EDS spectrum grain boundary showing the similarity in composition of the two regions in a specimen of alloy 3 synthesized without preheat (c) Bright field micrograph showing a grain boundary. No second phase particle can be seen at the boundary.

Fig. III. 5 Optical micrograph showing the microstructures of alloy 3 synthesized after different amounts of preheat (a) 513 K and (b) 673 K.

Fig. III. 6 (a) Bright field electron micrograph showing dislocations of $b=\langle 100 \rangle$ type in alloy 1 synthesized after preheating. Particles of Al oxide can also be seen. (b)

Bright field electron micrograph showing a grain boundary. No particles can be seen at this boundary.

Fig. III. 7 (a) Bright field electron micrograph showing screw dislocations of $b=\langle 111 \rangle$ types. Debris of screw dislocations, jogs leading to the formation of edge dislocations and particles of the Al oxide phase can also be seen in the micrograph. (b) Bright field electron micrograph showing the presence of dislocation loops. (c) Bright field electron micrograph showing a grain boundary devoid of any particles.

Fig. III. 8 (a) Bright field electron micrograph showing particles of the V_2NiAl phase at the grain boundary of a specimen of alloy 3 synthesized after preheating. (b) EDS spectrum from the particles at the grain boundary. (c) Bright field electron micrograph showing an array of dislocations with dislocation debris emanating from a grain boundary. (d) Bright field electron micrograph showing interacting arrays of $b=\langle 100 \rangle$ type dislocations. Screw dislocations with double image can also be seen. (e) Bright field electron micrograph showing a long screw dislocation of $b=\langle 111 \rangle$ type pinned at several places.

Fig. III. 9 Schematic diagram showing the use of the copper plates for stopping the reaction front. The position of the thermocouples are indicated by different numbers.

Fig. III. 10 Temperature profiles generated across the length of the sample. The numbers indicate the position of the thermocouples.

Fig. III. 11 Optical microstructure of the end of the sample at which ignition has been done.

Fig. IV. 1 Microstructure of the NiAlTiB alloy after synthesis without any preheat.

Fig. IV. 2 Microstructure of the NiAlTiB alloy after synthesis with preheat. (a) preheat temperature 473 K (b) preheat temperature 623 K.

Fig. IV. 3 Fractograph showing the fractured surface of the NiAlTiB alloy synthesized without preheat.

Fig. V. 1 Equiaxed grains of the NiAl phase in the microstructure of NiAl.

Fig. V. 2 Equiaxed grains of the NiAl phase in the microstructure of alloy 3. The presence of a second phase can be seen at the grain boundaries.

Fig. V. 3 (a) Micrograph showing thick grain boundary phase in alloy 4. EDS point count analysis (Figure (b)) indicated that this is the NiAlNb phase.

Fig. V. 4 Fractograph showing the fracture surface of the different alloys.

Fig. V. 5 Plots showing the rate of oxidation of different alloys at a temperature of 1100 C.

Fig. VI. 1 Schematic diagram showing the use of the copper plates for stopping the reaction front. The position of the thermocouples are indicated by different numbers.

Fig. VI. 2 Temperature profiles generated across the length of the sample. The numbered position indicate the position of the thermocouples.

Fig. VI. 3 Optical microstructure of the end of the sample at which ignition has been done.

Fig. VI. 4 (a) SEM micrograph showing the powder region (left), synthesized region (right) and the stopped combustion front (indicated by an arrow) (b) SEM micrograph of the powder region (c) SEM micrograph showing the end of the partially reacted region. (d) SEM micrograph showing the microstructure towards the end of the partially reacted region (e) EDS spectrum from a region marked on the micrograph shown in (d), (f) Micrograph showing the microstructure of a region closer to the stopped reaction front (g) EDS spectrum from a region marked on the micrograph shown in (f), (h) Micrograph showing the shrinkage of the Ni cores (i) Micrograph showing a large Ni particle at the stopped reaction front.

Fig. VI. 5 Cross section of the synthesized specimen showing region A and region B.

Fig. VI. 6 Schematic diagram showing the specimen and the different regions formed after synthesis.

Fig. VI. 7 SEM image of a region in region B showing the Nb and Ti bearing regions (a) backscattered image (b) Secondary electron image (c) Nb X-ray map (d) Ti X-ray map (e) Al X-ray map.

Fig. VI. 8 (a) Secondary electron image of region A (b) Nb X-ray map (c) Ti X-ray map (d) Al X-ray map.

Fig. VI. 9 (a) TEM micrograph from Ti rich area in region B (b) Diffraction pattern from Ti rich area, zone axis $[0001]$ Ti_3Al (c) Diffraction pattern from the Nb rich area, zone axis $[\sim 133]$ Nb_3Al .

Fig. VI. 10 Diffraction pattern from region A, zone axis $[\sim 112]$ B2.

Fig. VI. 11 SEM micrograph showing the boundary between the unreacted powders and region B.

List of Tables

Table I. 1 Adiabatic temperatures and heat of formation (reaction) of some selected exothermic reactions ($T_0 = 298 \text{ K}$)

Table I. 2 Examples of materials Produced by Combustion Synthesis

Table III. 1 Purity and Particle Size of the Powders Used

Table III. 2 Alloy Compositions and Densities

Table III. 3 Porosity, Grain Size, Hardness and Fracture Toughness of the Alloys

Table III. 4 Combustion temperature and Propagation velocity

Table IV. 1 Purity and Particle size of the Powders Used

Table IV. 2 Combustion temperature and Propagation velocity

Table IV. 3 Adiabatic temperatures and heat of formation (reaction) of some selected exothermic reactions ($T_0 = 298 \text{ K}$)

Table V. 1 Purity and Particle size of the Powders Used

Table V. 2 Combustion temperature and Propagation velocity

Table V. 3 Table showing X-ray diffraction results

Table V. 4 Hardness and Fracture Toughness of the Alloys

Table VI. 1 Purity and Particle size of the Powders Used

I. Introduction

In recent years, an alternative processing technique, termed micropyretic synthesis, has received considerable attention as a means for synthesizing and, in some cases, simultaneously densifying a variety of monolithic and composite intermetallics and ceramics [1-25]. Micropyretic synthesis is a powder processing technique involving the use of self-sustaining exothermic reactions between elemental and/or compound powders. In this technique, reactant powders are pressed into a compact and ignited using an external heat source. Once initiated, initial reactants will spontaneously convert into product(s), due to the exothermic heat of reaction. Over the past two decades, extensive research work has been done in this area and a basic understanding of the process has been developed both experimentally [5-13] and theoretically [14-17, 26-31].

Fig. I.1 shows the schematic diagram of a typical micropyretic synthesis process. An exothermic reaction,



is considered here. The powder compact containing reactants A and B is heated at one end with an external heat source. Once the reaction is initiated, the temperature of the reaction zone increases very rapidly due to the self-generated exothermic heat. Because of the temperature difference between this reaction zone and the zone adjacent to it, heat is conducted into the adjacent zone. The temperature of this adjacent zone increases up to the ignition temperature and a self-sustained reaction begins. This process of ignition, reaction (combustion), and heat transfer continues within the

compact and creates a self-propagating combustion wave (reaction zone) moving through the compact, leading to the product (AB) formation.

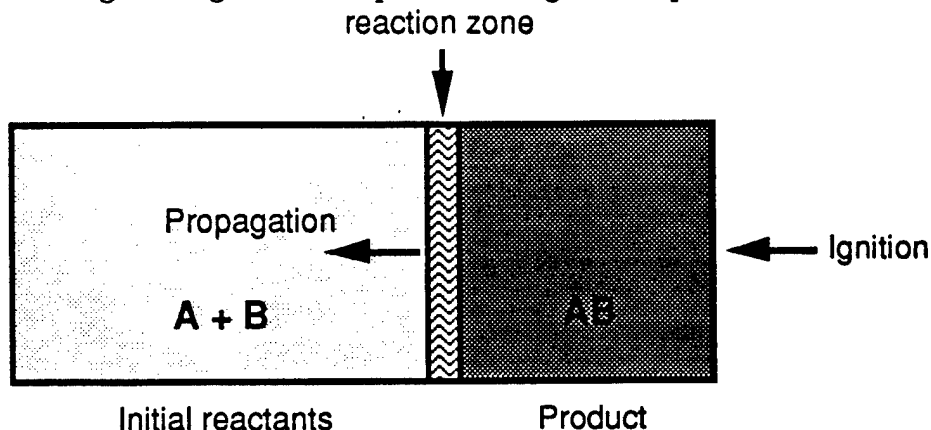


Fig. I. 1 Schematic diagram of a typical micropyretic synthesis process.

Micropyretic synthesis as a means of materials processing, presents an attractive alternative to the conventional powder metallurgy techniques. The uniqueness and attractiveness of this process include self-generation of energy, high reaction temperatures (1500 to 4000 °C), short processing times (a few seconds to a few minutes), high temperature gradients, and high heating and cooling rates. These unique and attractive features determine the advantages of the process. Major advantages can be listed as:

- substantial energy savings due to self-generation of energy by the reaction itself;
- low investment cost since no high temperature furnaces or complex processing equipment are required;
- high productivity due to short processing times;
- high-purity products since volatile impurities evaporate at high reaction temperatures;
- more reactive, metastable products due to high cooling rates.

Additionally, the micropyretic synthesis process can be used to make net shape components [21, 24]. The exothermic heat released by reaction itself makes it possible to develop the process for one-step manufacture of components.

This section of the report is directed toward reviewing the literature on the current state of developments of this technology, with special attention on the processing of composite materials. A brief description of the fundamentals and salient features involved in the micropyretic synthesis process is presented first. The types of reactions used for the synthesis of composite materials are then described. Finally, the processing, microstructures, and properties of the composite materials are discussed.

I. 2 MICROPYRETIC SYNTHESIS PROCESS

I. 2. 1 Underlying Principles

Chemical reactions that are accompanied by the release of thermal energy are referred to as exothermic reactions. The underlying principles of micropyretic synthesis are rather simple and are associated with the nature of the exothermic reactions. The micropyretic synthesis process is based on the effective utilization of the thermal energy of the exothermic reactions. The "driving force" for the self-sustaining synthesis process is the energy evolved by the conversion of the reactants to the product. However, to support such a self-sustaining synthesis process, the chemical reactions must be sufficiently exothermic. The exothermicity of the reaction is measured by the so-called adiabatic temperature.

The adiabatic temperature, T_{ad} , is the maximum temperature that can possibly be attained in the reaction system due to the self-generated heat from

the exothermic reactions. This can be calculated theoretically by assuming the system to be an adiabatic one. Considering the process shown in Fig. I. 1, the total heat released during the reaction is given by

$$\Delta H^0 = \Delta H_{f, T_0}^0 + \int_{T_0}^{T_{ad}} C_p (\text{product, solid}) dT \quad \text{I (2)}$$

where $\Delta H_{f, T_0}$ is the heat of formation at T_0 and C_p is the heat capacity of the solid product phase. Since the process is assumed to be adiabatic, $\Delta H^0 = 0$, therefore,

$$-\Delta H_{f, T_0}^0 = \int_{T_0}^{T_{ad}} C_p (\text{product, solid}) dT \quad \text{I (3)}$$

This equation indicates that T_{ad} is strongly dependent on the temperature T_0 at which the heat of formation is calculated. Typically, adiabatic temperatures are calculated on the basis of room temperature (298 K) since enthalpies of formation (or reaction) are commonly tabulated at 298 K. It should be noted that Eq. I. 3 is only valid when the adiabatic temperature (T_{ad}) is lower than the melting temperature (T_m) of the product. However, in a large number of cases the product may be partially or wholly melted. In such cases, the latent heat of fusion of the product should be considered. When the adiabatic temperature is greater than the melting temperature, the heat capacity of the liquid product should be considered. Therefore, when $T_{ad} = T_m$

$$-\Delta H_{f, T_0}^0 = \int_{T_0}^{T_m} C_p (\text{product, solid}) dT + v \Delta H_m \quad \text{I.(4)}$$

and when $T_{ad} > T_m$

$$-\Delta H^\circ_{f, T_0} = \int_{T_0}^{T_m} C_p (\text{product, solid}) dT + \Delta H_m + \int_{T_m}^{T_{ad}} C_p (\text{product, liquid}) dT \quad \text{I.(5)}$$

where n is the fraction of the product which is in the liquid state ($0 < n < 1$) and ΔH_m is the enthalpy of the fusion of the product at its melting temperature. Fig. I. 2 shows a representation of this type of calculation for the synthesis of MoSi_2 from its elements. The calculated adiabatic temperatures for some selected exothermic reactions are given in Table I. 1.

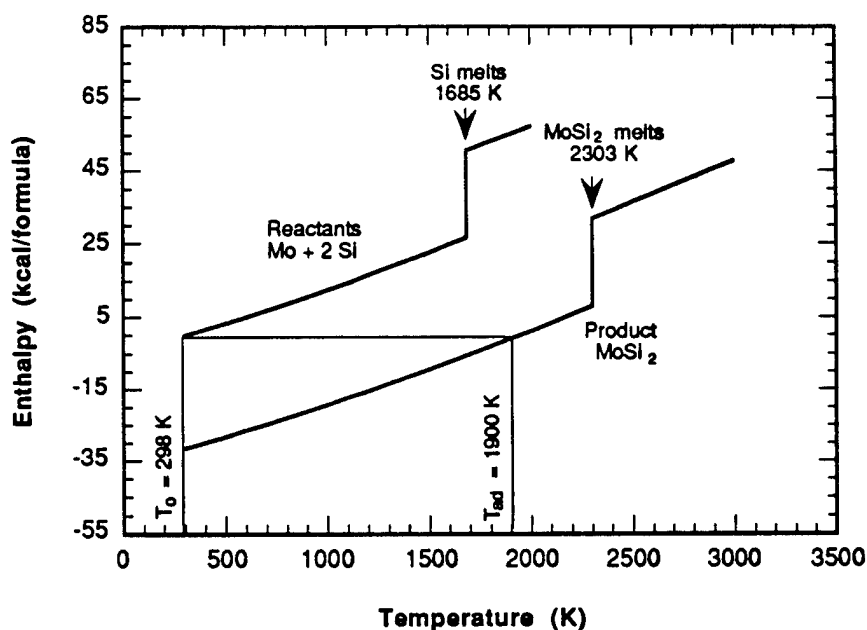


Fig. I. 2 A representation of the adiabatic temperature calculation for the synthesis of MoSi_2 from its elements.

As a measure of the reaction exothermicity, the adiabatic temperature provides useful information on ascertaining whether or not the synthesis of a

self-sustaining unless $T_{ad} \geq 1800$ K (highly exothermic) [6]. For those reactions with $T_{ad} < 1800$ K (weakly exothermic), the addition of external energy (preheating) prior to the initiation of combustion reaction may be required to support the micropyretic synthesis process.

I. 2. 2 Ignition and Combustion

In general, the micropyretic synthesis process consists of the following steps: mixing of initial reactants, cold-pressing of reactant mixtures, ignition of exothermic reaction, and combustion of reactant compacts. Most combustion reactions involve a mixture of two or more solid reactant powders (solid-solid reactions) although, in some cases, reactions may involve a solid powder with a gas such as nitrogen or hydrogen (solid-gas reactions). For solid-solid reactions, reactant mixing and cold-pressing steps are similar to those of conventional powder metallurgy methods. Therefore, only ignition and combustion are discussed here.

IGNITION: For the micropyretic synthesis process, the concept of ignition means that an exothermic reaction begins to become self-sustaining, i.e., the rate of heat generation by the reaction exceeds the rate of heat losses to the environment due to conduction, convection, and radiation. In order to achieve this, it is necessary to prevent any significant conversion of the reactants to the products below the ignition point. Therefore, initiation of a self-sustaining reaction requires the rapid energy input from an external source. Depending upon the degree of exothermicity, combustion reactions may be ignited in different ways. For highly exothermic reactions, the *wave propagation mode* is utilized. In this case, the reaction is ignited in only one part of the sample. Once initiated, the reaction can become self-sustaining

and will propagate through the reactant mixtures in the form of a combustion wave. The heat input required to start such reactions is relatively low and can be accomplished using a resistance heating coil, a torch, a electrical spark, a laser pulse, or other means. For weakly exothermic reactions, it is difficult to initiate and sustain in the form of a self-propagating combustion wave. Normally, such reactions are ignited by using the *thermal explosion mode*. In this case, the sample is heated in a furnace, i.e., reaction is initiated simultaneously in all parts of the sample. The furnace may be kept at the ignition temperature or the sample may be heated in the furnace at a predetermined heating rate to the ignition temperature. The thermal explosion combustion synthesis is sometimes also referred to as reactive/reaction sintering [32]. Although the synthesized product phases obtained by the wave propagation and thermal explosion techniques are usually the same, there are differences in the final product density [33]. Weakly exothermic reactions can also be initiated by the so-called *chemical oven mode*. In this case the reactant mixtures are encapsulated in a highly exothermic reactant mixture [34]. The latter is then initiated through the wave propagation mode.

COMBUSTION: Once initiated, the reaction proceeds in a self-propagating combustion wave (reaction zone). The thickness of the combustion zone is usually in the range of 0.1 mm to 5.0 mm. As the combustion wave advances, reactants are converted to the product. The existence and propagation of the combustion wave depends on the processes of heat generation (through the chemical reaction) and heat dissipation (through heat transfer and heat loss). Any alternation of the processes (by changing the process variables) may results in the change of the combustion wave stabilities. So far, several

distinct combustion modes have been observed and are divided into two general categories: *stable* (or *steady-state*) and *unstable* (or *nonsteady-state*) combustions. In stable combustion, the combustion wave propagates with a planar or slightly curved front from the ignition surface at a fairly constant velocity through the reactant mixtures to the opposite surface where the reaction is completed. Temperature and species concentration profiles across the wave remain unchanged. Under the unstable mode the combustion wave displacement is not uniform with time. The two most often reported unstable modes are *oscillatory* and *spin* combustions. In the oscillatory mode, the combustion wave propagates in a succession of fast and slow movements with a definable frequency and a constant mean wave velocity. The frequency and velocity may be increased or decreased by changing the process variables. Oscillatory combustion usually results in a layered structure of the product [13, 35]. In the spin mode, the reaction occurs at a small spot on the outer surface of the compact, and this spot subsequently moves in a spiral path along the side surface of the unreacted section, leaving behind a bright trace which gradually merges with a similar trace from the previous turn. The combustion mode may be converted from stable to unstable or *vice versa* by changing the conditions. For example, the addition of an inert diluent to the reactants or an increase in the particle size of the reactants may cause the stable combustion reactions to become unstable. Conversely, an increase in the initial temperature of the reactants (preheating reactants) may cause the unstable combustion reactions to become stable. Studies on the phenomena of stable and unstable combustion have been attempted both experimentally [13,35-38] and theoretically [27, 28, 39].

I. 2. 4 Processing Variables

In order to obtain a product with the required properties and microstructures, it is important to understand the parameters that control the process. Some of the important processing variables are green compact density, reactant particle size, preheating and dilution. The influences of these variables on the nature of the combustion process are usually characterized by the combustion temperature (T_c) and wave propagation velocity (V). A recent review by Rice [40] detailed these influences.

GREEN COMPACT DENSITY: In general, at lower compact densities, the wave propagation velocity increased with increasing density. At higher compact densities, however, an increase in the density led to a decrease in the propagation velocity. Depending on the system, the propagation velocity reached a maximum at about 50-80% theoretical density. It is believed that the initial increase in the propagation rate with an increase in density is due to better contact between the reactant particles as well as the increase in the thermal conductivity of the green compact. Beyond about 70% density, the conductivity effect becomes dominating and more heat from the reaction is dissipated through conduction. This leads to a decrease in temperature adjacent to the reaction zone and hence an overall decrease in the reaction propagation velocity takes place.

REACTANT PARTICLE SIZE: An increase in the reactant particle size generally results in a decrease in the propagation velocity and extent of the reaction completion. It is generally known that the large reactant particle size leads to an increase in the local thermal conductivity, thus removing heat from the

reaction front and decreasing the wave propagation velocity. Fine reactant particles are desirable for difficult-to-combust systems.

PREHEATING AND DILUTION: Preheating of the green compact increases the combustion temperature and wave propagation velocity. The increase in the combustion temperature increase is an extra energy (due to preheating) is added to the system, while the energy evolved in the reaction remains constant. The wave propagation velocity increase is because it takes less energy to ignite the reaction in the adjacent layer. Conversely, the addition of diluents (non-reacting materials) into the reactant mixtures reduces the combustion temperature and the wave propagation velocity. Dilution of a reaction can be accomplished by either adding end product particles to reactants, excess of a reactant, or some inert filler. The effects of preheating and dilution on the combustion temperature and wave propagation velocity have been utilized for the determination of activation energy of the combustion process, as discussed in the previous section.

I. 2. 5 Applications

The major current application of micropyretic synthesis is as an alternative processing technique for the production of a variety of new materials. There are a large number of materials that have been produced by this technique [5-8]. Table 2 lists some selected examples of materials prepared by this method. Some of these, e.g. titanium carbides, titanium diborides, and molybdenum disilicides, etc., are being produced in a pilot plant [8]. The products by micropyretic synthesis can be in either powdered forms or highly dense bodies.

Additionally, several novel techniques based on the combustion synthesis process have been developed recently. One of the examples of such novel applications is the so-called "centrifugal-thermite process" adapted by Odawara *et al.* [41, 42] for the preparation of ceramic-lined and ceramic composite pipes. Another example is the pressurized combustion reaction process which has been developed for the welding/joining of ceramic-to-metal, ceramic composite-to-ceramic, and intermetallics-to-intermetallics [43-44].

Table I. 2 Examples of materials produced by combustion synthesis [6]

| | |
|-------------------|--|
| Borides | CrB, HfB ₂ , NbB ₂ , TaB ₂ , TiB ₂ , LaB ₆ , MoB ₂ |
| Carbides | TiC, ZrC, hC, NbC, SiC, B ₄ C, WC |
| Carbonitrides | TiC-TiN, NbC-NbN, TaC-TaN |
| Cemented carbides | TiC-Ni, TiC-(Ni, Mo), WC-Co, Cr ₃ C ₂ -(Ni, Mo) |
| Chalcogenides | MoS ₂ , TaSe ₂ , NbS ₂ , WSe ₂ |
| Composites | TiC-TiB ₂ , TiB ₂ -Al ₂ O ₃ , B ₄ C-Al ₂ O ₃ , TiN-Al ₂ O ₃ |
| Hydrides | TiH ₂ , ZrH ₂ , NbH ₂ |
| Intermetallics | NiAl, FeAl, NbGe, TiNi, CoTi, CuAl |
| Nitrides | TiN, ZrN, BN, AlN, Si ₃ N ₄ , TaN (cubic and hexagonal) |
| Silicides | MoSi ₂ , TaSi ₂ , ZrSi ₂ , Ti ₅ Si ₃ |

I.3 MICROPYRETIC SYNTHESIS OF INTERMETALLIC COMPOUNDS

Many intermetallic compounds particularly the aluminides in the Ni and Ti system are amenable to synthesis by the process of micropylretic synthesis because of their high adiabatic temperatures and high heat of

mixing. Besides those mentioned in the previous section, this process of synthesis offers the following very important advantages in the case of synthesis of intermetallic compounds.

1. It is rapid process of alloy making. A large number of alloys can be made in a short period of time and hence the process is ideally suited for situations where many alloys need to be made for optimization of properties.

2. The microstructure of the alloys generated by this process are very homogenous at a microscopic level therefore eliminating the need for homogenization heat treatments or the need for complex thermomechanical processes.

3. The desired stoichiometry can be readily and accurately achieved on a macro as well as microscopic level. This is because of accurate weighing of powders and the intimate mixing of the powders during milling. Most importantly there is no loss of low melting elements like Al which tend to vaporize in melting processes like arc melting.

4. The synthesized microstructure often has the equiaxed grain morphology, a most desirable microstructure from the view point of mechanical properties. In other alloy making processes, the alloy making has to be followed by thermomechanical treatments in order to break the cast structure and obtain equiaxed grain morphology.

II. THE EFFECT OF DIFFERENT PROCESSING PARAMETERS ON THE SYNTHESIS PROCESS

Micropyretic synthesis has several process variables. The size of the powder particles, the compaction pressure, the nature and amount of diluents and degree of preheat are to name a few. This chapter examines the effect of these variables on the process of synthesis. The effect of these variables on the properties have been established through processing maps. Using these maps it is possible to select process variables for obtaining optimum properties.

II. 1 Effect of Particle Size

The initial dispersion of reactants and the particle sizes determine the kinetics of synthesis of all powder metallurgical reactions including micropyretic/combustion synthesis [35, 45, 46]. It has been shown that both diffusion and capillary-controlled combustion are significantly dependent on the particle size of the melting reactants in solid-solid combustion reactions [45, 46]. In systems with a small amount of the low melting component, it is not recognized that the combustion rate is diffusion-controlled [13, 35] whereas capillary spreading is rate controlling in systems with a larger amount of low melting component. The particle size influences not only the propagation velocity [45] of the combustion front but also the uniformity and physical properties of the products formed [12, 13, 45].

The effect of the size of the lower melting component (Al) has been examined in the study by changing the Al particle size from 5 μm to 64 μm and finally to 151 μm while the Ni particle size was kept constant at 7.6 μm . It was observed that only the mixture having 5 μm Al particles was able to

ignite and propagate at the temperature of 523 K, whereas the mixtures with higher Al particle sizes were not ignitable even though the initial porosity of mixtures were similar. Prior to the combustion, the melting of the larger Al particles takes longer than the smaller ones. This gives time for the heat to dissipate thus significantly enhancing the heat loss. Therefore, mixtures which contained the larger Al particles were noted to be not ignitable. When the Al size was further decreased from 5.0 μm to submicron (average diameter: $0.8 \pm 0.4 \mu\text{m}$), it was noted that the propagation velocity and final porosity of the mixture with the submicron Al were similar to those of the mixture with 5 μm Al.

It has been reported that the propagation velocity is independent of the particle size of the low melting component (Al) in the diffusion-controlled region [46]. In this study all the studied mixtures were in the diffusion-controlled combustion region. In addition, the melting of the Al phase has been reported to be essential prior to the onset of the micropolyretic synthesis reaction [31, 35, 55]. Therefore, when the Al particle size is decreased to a critical value ($< 5 \mu\text{m}$ in this study), a further decrease in the Al particle size does not affect the propagation velocity or other properties of the synthesized products.

An increase in the Ni size decreased the initial porosity noticeably where as a similar increase in the Al particle size only slightly increased the porosity. The cause for this difference is probably because of the different characteristics of the Ni and Al particles. The Al particle is soft and is easily deformed, therefore, the initial porosity is only slightly dependent on the Al size. On the other hand, the Ni particle is harder than the Al particle, thus, the porosity is

strongly dependent on the size of the hard particle as different particle sizes strongly influence the packing density [47].

The combustion temperature was not found to be influenced by the Ni particle size. However, the cooling rate and the plateau temperature where the phase transformations take place were found to depend on the Ni particle size. For the mixtures with smaller Ni particle size after ignition, the temperatures first sharply increased to 1910 K, which is close to the melting point of the NiAl product (1912 K). Then the product NiAl started to melt, therefore, the temperature remained at this point for a while and then increased again. For mixture 3, which contains the large Ni particle, the plateau temperature is noted at 1725 K, which is close to the melting point of the Ni phase (1726 K). Prior to reaching the melting point of the product phase, 1912 K, it takes a longer time to melt the larger Ni particles than the smaller ones during the reaction. Thus, the temperature plateau for the mixture with the large Ni size is reduced to the melting point of the Ni particle. This also gives time for the heat to dissipate down the gradient in front of the combustion interface and the combustion peak temperature is therefore noted to be slightly lower.

Figure II. 1 shows a plot of the combustion temperature and the propagation velocity as a function of the Ni particle size and reveals that the combustion temperature and propagation velocity of the combustion front increase with a decrease in the Ni particle size. Normally, the propagation velocity is proportional to the combustion temperature [43, 44, 45]. However, the propagation velocity shows significant variation for mixtures 1 - 3 even though their combustion temperatures are noted to be similar. This is because the combustion takes place at a temperature corresponding to the melting

point of the synthesized product. At the melting point, an increase in the enthalpy in the system, which increases the combustion front propagation velocity, only increases the melted fraction of the synthesized product thus causing the combustion temperature to remain at the melting point.

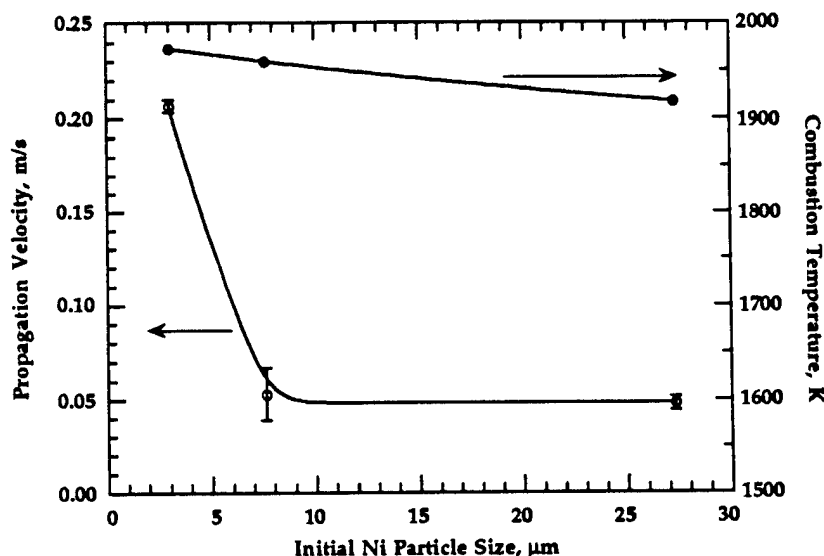


Fig. II. 1 Dependence of the propagation velocity and the combustion temperature on the Ni particle size.

It has been shown before [22] and for the present experiment that for a given initial porosity, the mixtures with larger Ni particle size display lower combustion temperature and velocity when compared with the smaller Ni particle mixtures. From theoretical kinetic consideration, the pre-exponential factor, K_0 , has been reported to relate with particle size: $K_0 \approx A_0 D_0 / r_0^2$, where A_0 is the correction factor, D_0 is the reference diffusion coefficient and, r_0 is the radius of the high melting point component [43]. An increase in the Ni particle size (r_0) decreases K_0 , therefore, slowing down the reaction kinetics and reducing the combustion temperature and the propagation velocity. The larger Ni size additionally decreases the initial porosity for a given

compaction pressure and further increases the reactant thermal conductivity. Increasing the Ni particle size also increases the product porosity and further decreases the thermal conductivity of the product. In other words, an increase in the Ni particle size, which decreases the product thermal conductivity and increases the reactant thermal conductivity, decreases the ratio of the product thermal conductivity to the reactant thermal conductivity. According to the analytical investigation in reference 45, a decrease in this ratio decreases the propagation velocity. Both the decrease in the pre-exponential factor, K_0 , and the ratio of product to reactant thermal conductivity with an increase in the Ni particle size led to a decrease in the propagation velocity.

Note from Figure II. 1 that the propagation velocity is only slightly dependent on the Ni particle size when the Ni size is initially decreased from 27.3 μm to 7.6 μm . This is because a decrease in the Ni size from 27.3 μm to 7.6 μm has a limited influence on the initial porosity and K_0 factor. When the Ni particle size is changed from 27.3 μm to 7.6 μm , the initial porosity only slightly increased from 34 % to 36 %. Therefore, such as a change of the initial porosity may not affect the thermal conductivity and thus propagation velocity. On the other hand, the mixture with 2.7 μm Ni particle has a much higher porosity (45 %), therefore, a significant change is noted in the thermal conductivity. In addition, decreasing Ni particle size to the 2.7 μm also dramatically increases the K_0 factor. When the particle size is decreased from 27.3 μm to 2.7 μm , the K_0 factor increases 83 times, as compared with 13 times when the decrease is from 27.3 μm to 7.6 μm . The influence of the porosity (thermal conductivity) and K_0 factor both become significant when the Ni particle size is decreased to 2.7 μm . This aids to explain the observation recorded above that the propagation velocity initially only changes slightly

and then increases dramatically when the Ni particle size is decreased from 27.3 μm to 2.7 μm .

It could be concluded that a change in the low melting component (Al particle) size is noted to have a limited influence on the micropyretic synthesis conditions. However, a change in the high melting component (Ni particle) size not only influences the combustion temperature and propagation velocity, but also affects the final porosity and grain size of the synthesized products. The combustion mode is also noted to change from stable to unstable when the Ni particle size is increased. It is noted that a diffusion type control mechanism is dominant for the rapid reaction sequence in the NiAl system. An atomistic mechanism of the Ni-Al micropyretic reaction is also proposed through a model [66]. Following this model, analytical expressions are developed to relate the variation of the Ni size and NiAl formation rate with the imposed processing conditions during the micropyretic synthesis. The mechanism of the final grain formation and the grain size changes with changes in the processing variables have been analyzed.

II. 2 Relationship Between Combustion Parameters and Dimensional Changes

For the development of processing maps for net shape products, it is important to understand the dimensional changes during micropyretic synthesis. Additionally, the information obtained from the dimensional changes will be scientifically interesting and challenging to correlate to the final porosity and the mechanical properties of the synthesized products. The relationship between the dimensional changes and the initial processing

parameters have been established. The systematic study of the influence of the processing and material parameters, including initial temperature, compaction pressure, Ni particle size, and chemical composition, on the dimensional changes of the synthesized product during micropyretic synthesis has been carried out. The relationship between the porosity change and elongation is also sought. From a knowledge of this relationship it is expected to tailor the dimensions of a synthesized product for proper design in an engineering application.

One of the features associated with micropyretic synthesis is that the synthesized product is porous. The porosity plays an important role towards determining the dimensional changes during micropyretic synthesis. It has been reported that the porosity may be attributed to the following factors: [58] (1) the molar volume change which accompanies the formation of the products; (2) the porosity present in the green unreacted compact; and (3) the adsorbed gases and moisture which redistribute during the reaction. The porosity of the product directly impacts on the final dimension and on the strength of the synthesized product [22, 48, 49-51]. Thus, it is important to understand how to make a reliable net-shaped product by controlling the product porosity.

Very few investigations have been reported on the dimensional changes of the net-shape product by micropyretic synthesis [21, 52, 53-55]. The first study of the correlation of the initial processing parameters with the dimensional changes and mechanical properties has been reported in our previous studies [48, 50]. Kumar [52] has shown a decrease in the elongation of synthesized MoSi_2 from 6.4% to 0% as the initial temperature of the reactants is increased from room temperature to 715 K. Rice [40] has reported that large

pores are commonly generated in a Ti-C product compact on account of outgassing during the reaction. He also indicates that a higher initial density and fine reactant particles may cause high dimensional changes in an unconstrained specimen [40].

The correlations of the processing parameters with the dimensional changes were analysed. In this study, strong exothermic system (Ti-B and Ti-C reactions) and weak exothermic system (Ni-Al reaction) were both chosen to study the dimensional changes for various compaction pressures, particle sizes, chemical compositions, and initial temperatures.

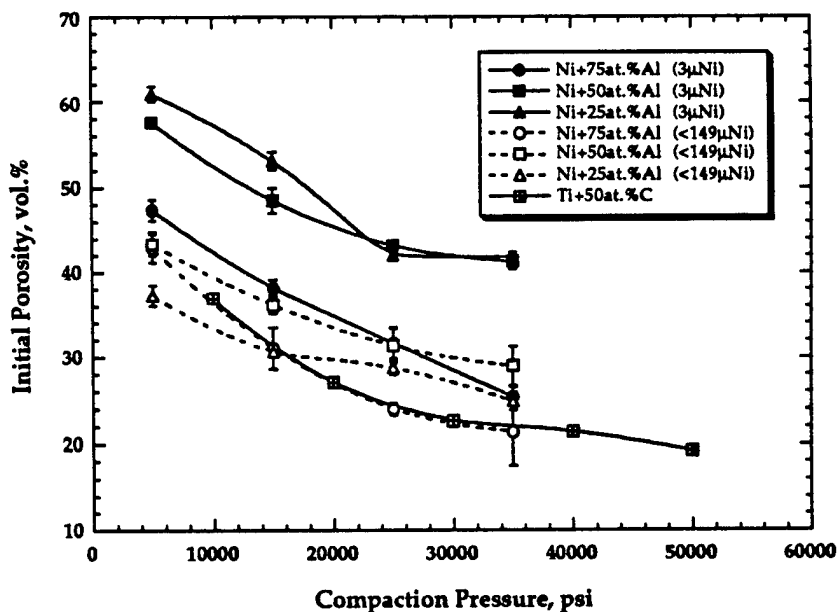
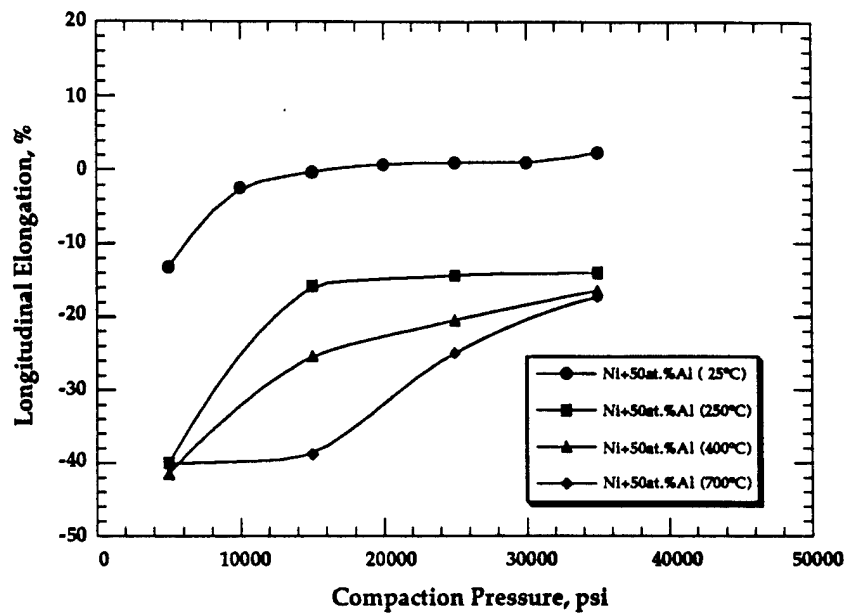


Fig. II. 2 Effect of the compaction pressure on the initial porosity of the unreacted green compact.

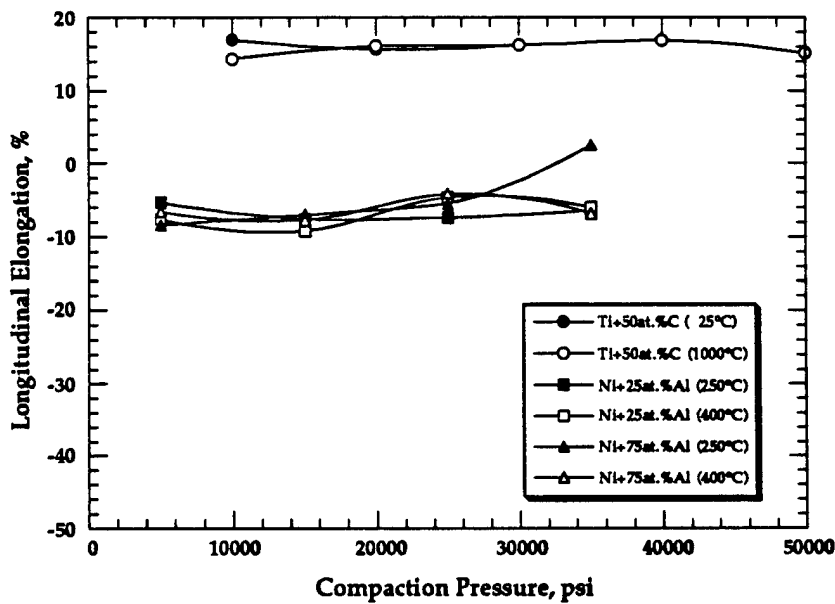
Figure II. 2 shows the effect of compaction pressure on the initial porosity of the studied compositions. Different compaction pressures may result in different initial porosity contents. Therefore, the compaction

pressure also influences the thermal conductivity of the unreacted compact and further affects the time to initiate combustion. A high compaction pressure leads to more efficient contact between the particles, thereby increasing the thermal conductivity. Thus, high compaction pressures increase the heat loss at the local ignition spot, resulting in a longer time being required to heat up the sample to the ignition temperature. It has been reported that the low melting point phase, namely the Al phase in the Ni-Al system, is required to be melted prior to the onset of combustion [4, 42, 43]. The specimen with the higher volume fraction of the Al phase is reported to require more energy for the melting of Al.

Figure II. 3 shows the dependence of longitudinal elongation on the compaction pressure for the Ni-Al and Ti-C systems. The longitudinal elongation is calculated from the length change before and after the reaction in the propagation direction. In the Ni + 50 at.% Al compositions (NiAl stoichiometry), the percentage of negative elongation (shrinkage and densification) is noted to increase as the compaction pressure decreases. The increased percentage of shrinkage in the Ni-Al system is reported to be related to the filling of the pores by the liquid Al prior to and during combustion [4, 25]. Nekrasov *et al.* [46] have shown that when the initial porosity is close to the volume fraction of the melted phase (*i.e.*, the Al phase in the Ni - Al system), the melted liquid phase will easily fill the pores. In the NiAl stoichiometric composition (Ni + 50 at.% Al), the volume fraction of Al phase is ~61 vol.%. Note from Figs. II. 2 that the sample with the lowest compact pressure contains the initial porosity value (59 vol.%). This value is close to the volume fraction of Al phase (61 vol.%). Thus, the specimen with the lowest compaction pressure has the largest shrinkage.



(a)



(b)

Fig. II. 3 Dependence of the longitudinal elongation on the compaction pressure for various initial temperatures of the unreacted specimens. (a) Ni + 50 at.% Al composition and (b) Ti + 50 at.% C, Ni + 25 at.% Al, and Ni + 75 at.% Al compositions.

In the Ti-C system, the combustion is violent and may cause severe thermal stresses and outgassing during the combustion. Many large pores are therefore generated and the specimen expands. In addition, the volume fraction of the Ti and the initial porosity are not at the optimum value. The thermal conductivity of the initial sample is known to severely influence the combustibility [17]. When the pressure exceeded 241 MPa (35000 psi), the thermal conductivity is enhanced and the heat loss is correspondingly increased, therefore the TiC compacts can not be ignited at room temperature (298 K).

When the initial temperature of the sample is increased, the combustion temperature is correspondingly increased and the shrinkage of the specimen is increased. If the initial temperature of the specimens in the NiAl is raised to 973 K, the reaction moves towards the thermal explosion combustion. The reaction is now at a higher temperature and more melted liquid easily flows outwards. The samples (ignited at 973 K) are noted to be severely distorted and shrinkage is higher when compared with the samples with the lower initial temperature. In the TiC stoichiometric compositions (Ti + 50 at.% C), it is noted that the nature of the combustion changes from the unidirectional wave propagation mode to the thermal explosion mode when the initial temperature reaches 1000°C. The samples have similar values of elongation even though they are ignited by different initial temperatures and combustion modes. It has been reported [7] that as the initial temperature increases from room temperature to 1340 K, the combustion temperature of the Ti-C reaction (close to the melting point of the TiC product) remains constant with the only increase in the melted fraction of the TiC product phase, from 33% to 100%. Thus, increased initial temperature does not help

to increase the combustion temperature. It may therefore be reasoned that the Ti-C samples with different ignition modes and initial temperatures when they have similar combustion temperatures, result in similar elongation.

The particle sizes of the reactants play an important role on the thermal conductivity and rate of reaction [42, 48]. It has been shown earlier that samples with a small reactant size have been reported to have a higher propagation velocity and combustion temperature. The larger particles also result in a lower initial porosity of the unreacted samples. The low initial porosity may decrease the propagation velocity. It has been seen that for the Ni-Al system for compositions with the same compaction pressure, the negative elongation (shrinkage) of a sample with fine Ni particles, $\sim 3 \mu\text{m}$, is higher than those with coarse Ni particles, -100 mesh ($< 149 \mu\text{m}$).

Elongation is of concern when designing for engineering applications. In the NiAl system, the shrinkage of the synthesized product is noted to relate to the propagation velocity for a given compaction pressure and reactant size. The higher propagation velocity, which is equivalent to the higher combustion temperature, may cause more liquid phase to form, further eliminating the pores and increasing the shrinkage. The knowledge of the propagation velocity, therefore, can be used to infer the elongation. The values of the intrinsic length change are calculated from the molar volume change, assuming that the expansion is isotropic and the reaction goes to completion. For the Ni-Al system, the elongation without the intrinsic volume change may also be plotted for engineering reference. The values of the compaction pressure and elongation of the product are easily measured in an experiment. If the compaction pressure is known, the initial porosity can be obtained, and the porosity change may be estimated from the measured

elongation. The final product porosity therefore may be calculated from the initial porosity and the porosity change. Thus, from a knowledge of the elongation and compaction pressure it is possible to infer the product's porosity and further tailor the dimensions and mechanical properties of a synthesized product [48] for proper design in an engineering application.

II. 3 Numerical Models

An improved analytical model for micropyretic synthesis is developed in this chapter. The features of the model include consideration of the thermophysical and chemical properties of both the reactants and products, as well as considerations of porosity for both reactants and products. An analysis of the variation of dimensionless velocity with the variation of dimensionless thermal conductivity, density and heat capacity is carried out. The equations for the combustion temperature and combustion velocity with the inclusion of non-reacting diluents and different thermophysical and chemical properties of the reactants and products is also developed. An equation considering non-melting reactant radius and the different thermophysical and chemical properties of the reactants and products is derived using a diffusion kinetic equation. Master plots for general solid-solid reaction systems, which relate dimensionless velocity, thermal conductivity, density and heat capacity are presented. Application of this model to the combustion synthesis of TiC has been carried out to study the variation of the combustion front motion in relation to the radius of carbon particles. A comparison of velocities for NiAl predicted by the model as a function of the reactant porosity is presented and compared with the experimentally determined value. The comparison is noted to be close except when the thin zone approximation is no longer valid.

A multi-dimensional numerical model for micropyrretic/combustion synthesis is developed and then applied to a special configuration in this chapter. The configuration is chosen to illustrate the differences between one dimensional and two dimensional combustion. The features of the model include the melting of each constituent of reactants and products and considerations of porosity for both reactants and products. Application of this model to the oscillatory combustion synthesis of TiB_2 has been carried out for the first time to study two dimensional combustion front movement. The model predicts higher hot-spot temperatures in a two-dimensional situation than those obtained in a one-dimensional experiment. Additionally, hot spots are noted to traverse along orthogonal directions. Some processing implications of such results are examined.

A numerical model for the combustion synthesis of a composite system accounting for porosity and dilution is developed. The model is used to study the effect of the variation of porosity on the combustion temperature, combustion velocity and the mode of combustion in the TiB_2 and TiC systems. A feature of the numerical formulation is that all of the reactants including the diluent and product may melt. The results show that the variation of porosity not only changes the combustion temperature and combustion velocity but also the nature of combustion. The results also show that the same values of combustion temperature and combustion velocities may be obtained at different porosities. The calculations of the frequencies of oscillations at various values of porosities were performed for the TiB_2 system. Results indicate that as the porosity values are decreased, the frequency of oscillations of the combustion front first increase and then decrease after reaching a maximum at a particular value of porosity. Thus it is

possible that the nature of the microstructure formed in two different cases of initial porosities may be different. There is a maximum in the value of combustion temperature and velocity with porosity. The consideration of porosity in the numerical calculation has revealed that the mechanism for the decrease in the velocity after reaching the maximum is different for the TiC and TiB₂ systems. In the TiC system the decrease in the velocity at low values of reactant porosity is due to the high value of thermal conductivity of the reactants. In the case of the TiB₂ system the decrease in the velocity at very low values of reactant porosity is mainly due to an increase in the value of product porosity. Unlike in the TiB₂ system, oscillations were not observed in the TiC system. The results presented in this article highlight the importance of considering the effect of porosity and diluents in the numerical calculations for modeling combustion synthesis and any subsequent analysis to obtain activation energies or predict microstructures.

II. 4 Processing Maps

From the above discussion, it is noted that the mechanical properties of the micropyrethically synthesized products are highly dependent on the final porosity. Thus, the complete understanding of the correlation of the final porosity with the various initial processing parameters is important because it can be used to infer the mechanical properties from the initial conditions. Processing maps are very versatile tools used for materials process design. They are plots mapping the initial processing conditions to the final properties of the materials produced. These maps are used to predict the final properties of the materials from the initial processing conditions. The processing maps which were introduced in reference 7 may be used to correlate several initial conditions with processing response parameters and

final properties. From the processing maps, the values of the porosity can be inferred for any combination of the compaction pressure, initial temperature, particle size and chemical composition.

Micropyretically synthesized products are influenced by the initial processing conditions like, the chemical composition, the compaction pressure, the diluent content and the reactant size [22, 25, 57]. Thus, processing maps can be developed by mapping the initial conditions to the final material properties like hardness and porosity.

The processing maps are shown in Figure II.4-II.7 for NiAl alloys with Si additions. Any two initial processing parameters are represented on the X and Y axis, and the final property is mapped on the Z-axis. In the present report, the Si wt% and the compaction pressure were chosen as the initial processing variables plotted on the X and Y axes. Green porosity, combustion velocity, final hardness and final materials porosity were the properties plotted along the Z-axis.

II Conclusions

The effect of particle size on the synthesis process has been shown. A change in the low melting component (Al particle) size is noted to have a limited influence on the micropyretic synthesis conditions. However, a change in the high melting component (Ni particle) size not only influences the combustion temperature and propagation velocity, but also affects the final porosity and grain size of the synthesized products.

The influences of various processing parameters on dimensional changes (property) and band spacing (microstructure) have been studied. The

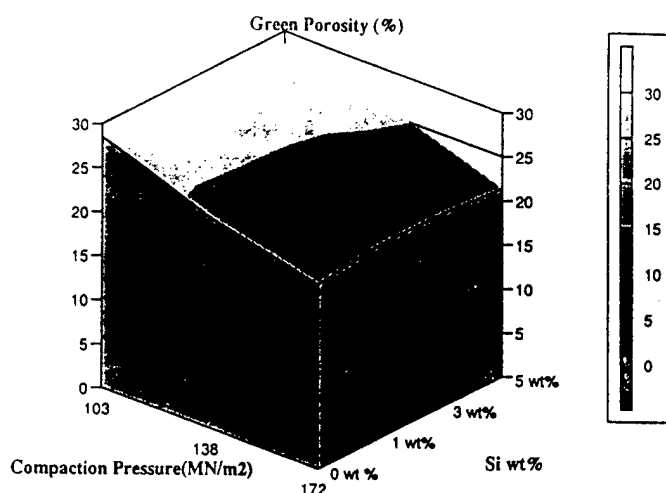


Fig. II. 4 Processing map for green porosity as a function of the compaction pressure (in MNm^{-2}) and the Si content (in wt%). The constants in the map are the Ni, Al and Si particle sizes, which are -100 mesh, -325 mesh and -325 mesh respectively. The processing for all the compositions is carried out at room temperature, without any preheating.

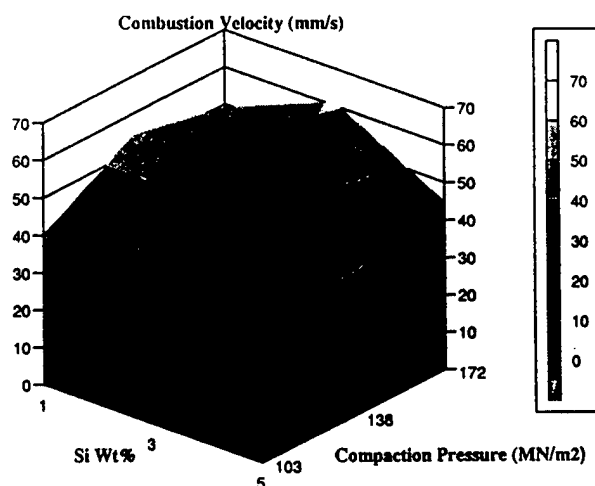


Fig. II. 5 Processing map for combustion velocity as a function of the compaction pressure (in MNm^{-2}) and the Si content (in wt%). The constants in the map are the Ni, Al and Si particle sizes, which are -100 mesh, -325 mesh and -325 mesh respectively. The processing for all the compositions is carried out at room temperature, without any preheating.

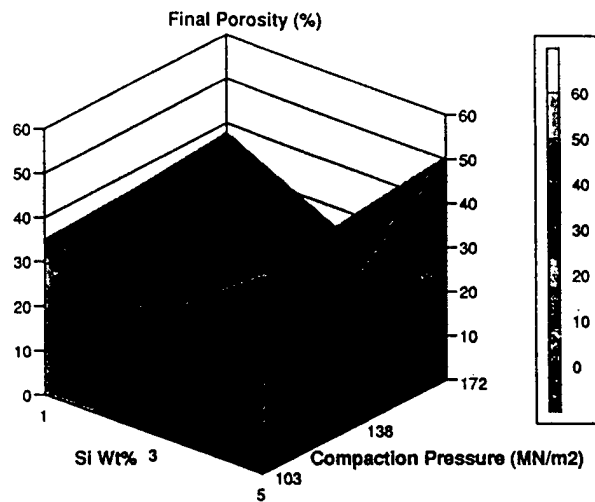


Fig. II. 6 Processing map for final porosity as a function of the compaction pressure (in MNm^{-2}) and the Si content (in wt%). The constants in the map are the Ni, Al and Si particle sizes, which are -100 mesh, -325 mesh and -325 mesh respectively. The processing for all the compositions is carried out at room temperature, without any preheating.

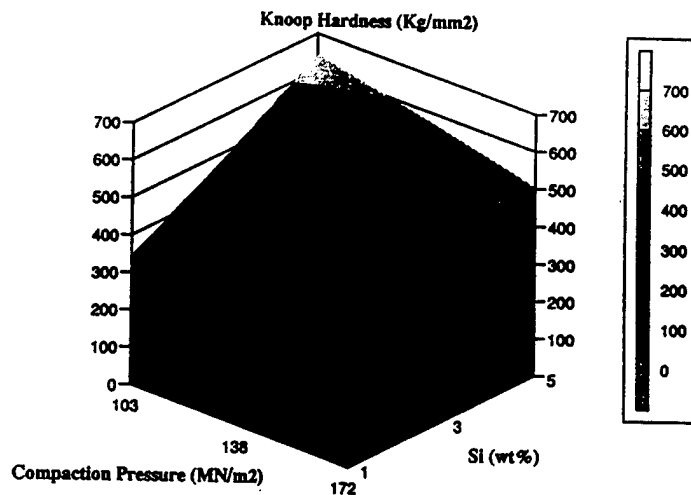


Fig. II. 7 Processing map for knoop hardness as a function of the compaction pressure (in MNm^{-2}) and the Si content (in wt%). The constants in the map are the Ni, Al and Si particle sizes, which are -100 mesh, -325 mesh and -325 mesh respectively. The processing for all the compositions is carried out at room temperature, without any preheating.

knowledge of the dimensional change and band spacing can be used to predict the final porosity and combustion instability, respectively. It has been shown that an increase in the propagation velocity increases the shrinkage and decreases the band spacing. An understanding of such relationships can be used to tailor net-shape products and to avoid non-homogeneous banded structures.

A systematic numerical investigation of the influences of the material and processing parameters on the temperature profiles for self propagating micropyretic synthesis has also been studied. The numerical results are aimed at understanding the effects of the various combustion parameters on the synthesis. In addition, from the established correlations of the property / microstructure with the propagation velocity, the calculated propagation velocity can be used to forecast dimensional changes and band spacing for various processing conditions.

Finally, processing maps have been created to encompass and collapse the results generated in this dissertation. These complete processing maps are developed by combining the experimental results and numerical modeling. The values of the maps lie in the predictability of final properties from any initial processing conditions.

III. MICROPYRETIC SYNTHESIS OF TOUGH NiAl ALLOYS

NiAl has been produced by micropyretic synthesis in a tougher state by adding Cr, V, and Fe. The mechanical properties and the fracture behavior of the alloys have been evaluated. The effect of different process variables like particle size, diluents and extent of preheat on the process of synthesis and microstructure have been ascertained. The microstructure of the alloys has been examined for chemical homogeneity and the defect structure. The sequence of steps leading to the formation of NiAl from elemental powders during the process of micropyretic synthesis has been determined.

III. 1 Introduction

Intermetallic compounds have attracted considerable attention in recent times because of their vast application potential in the aerospace industry [58]. The enormous application potential of the intermetallics especially aluminides stems from their many attractive properties, specially relatively low densities, high oxidation and corrosion resistance, combined with their ability to retain strength and stiffness at elevated temperatures [59, 60]. A considerable amount of work has already been done on the aluminides in the Ti-Al and the Ni-Al systems [61, 62]. Amongst the Ni aluminides, NiAl has emerged as a possible high temperature structural material because of its low density, high melting temperature, good thermal conductivity and excellent oxidation resistance. It has several advantages over superalloys and other intermetallics like Ni₃Al [63]. As is the case with other aluminides, NiAl has certain drawbacks, the most important being the lack of ductility at ambient temperatures. Several attempts have been made to alleviate the problem of room temperature brittleness in NiAl through modification of slip systems,

grain refinement, use of single crystals and microalloying with boron [64, 65]. Studies have shown that in addition to conventional casting and powder metallurgy fabrication techniques, micropyretic synthesis may also be used successfully to obtain net shapes in this alloy [13, 23]. Micropyretic synthesis has several advantages over other synthesis techniques, the most important ones being the possibility of direct net shape fabrication and enormous saving in energy spent on the fabrication and processing [22].

In the case of intermetallic compounds like NiAl, the examination of the effect of alloying additions, added with a view towards improving mechanical properties of the alloy, remains a study of paramount significance. In micropyretically synthesized alloys, the addition of a third alloying addition is likely to influence the micropyretic synthesis process and hence the properties of the alloy. In this study, the effect of minor alloying additions on the micropyretic synthesis of NiAl has been examined. These alloying additions have been made with the intention of improving the mechanical properties of the alloys. The influence of the following processing parameters on the process of synthesis of NiAl have been investigated in this article- particle size, diluents, and preheat. Although the effect of particle size and that of diluents have been examined by Li et al. [66, 67], the influence of preheat on the microstructure on the process of synthesis has not been examined before in any previous studies. An attempt has been made to study the mechanism of the micropyretic synthesis of the multicomponent alloys by arresting the combustion front by squeezing the specimen between two copper plates. A detailed microstructural study has been carried out around the frozen combustion front in order to establish the sequence of formation of the NiAl phase from the elemental powders of Ni and Al.

Micropyretic synthesis is a process in which alloying occurs at a local level at a very rapid rate. In a process of this nature, the homogeneity of the resulting microstructure in terms of phase content and composition is important. Despite the fact that the homogeneity of the microstructure is quite important in products made by this process, not many studies have been conducted to examine this aspect in other systems and none at all in NiAl. In this study, the synthesized microstructure has not only been examined using a SEM, the crystallographic defects present and compositional homogeneity of the microstructure have also been probed by a TEM. It is noted that the compositional and microstructural homogeneity of the microstructure synthesized product is unusually good. In order to ascertain the reasons for enhancement in ductility, the microstructure after deformation has been examined and compared with that before deformation. The deformed microstructure of polycrystalline NiAl having these alloying additions has not been done before. An examination of the deformed and undeformed microstructures of unalloyed or alloyed NiAl made by combustion synthesis has been done for the first time in this study.

III. 2 Experimental

High purity powders (purity and size indicated in Table III.1) were weighed accurately and mixed in a Spex model 8000 ball mill for twenty minutes without the addition of any liquid medium. Subsequently, the mixed powders were pressed into rectangular bar specimens in a double acting press at a pressure of 160 MPa. The pressed compacts were combusted in an inert atmosphere by igniting from one end. The chamber used for combustion is shown in Fig. III. 1. It comprised a quartz tube which could be evacuated and then filled with AR to maintain a steady flow over the

specimen. The specimen was placed on an alumina boat. The temperature of the specimen could be monitored by placing thermocouples at different parts of the specimen. Combustion was initiated by heating one end of the specimen by induction heating. In this study, synthesis was carried in air as well as in inert atmosphere of flowing argon (Figure III. 1). It was observed that argon reduces the oxidation of the specimen substantially during

Table. III. 1 Purity and Particle size of the Powders Used

| Element | Purity | Powder size |
|---------|--------|-----------------------------|
| Ni | 99.7 | 3 μm , -100 mesh |
| Al | 99.5 | -325 mesh |
| Cr | 99.0 | -325 mesh |
| Fe | 99.9 | 10 μm |
| V | 99.5 | -325 mesh |

synthesis. Argon was also found to influence the propagation of the reaction front. Two distinct situations could be identified- 1. the combustion front propagating in the same direction as the gas flow and 2. combustion front moving in a direction opposite to the direction of the gas flow. In the first situation, the gas flow had two opposite effects. The first effect was the quenching effect because it took away a lot of heat from the combustion front and slowed the front down. However, the gas flow and the front propagation direction being the same, the gas tends to heat the specimen slightly ahead of the front and can have a preheating effect. In both the cases of synthesis the effect of the gas as a quenching medium was quite severe and it resulted in considerable slowing down of the combustion front.

The dimensions of the specimen were found to change after synthesis. The combusted specimen were made uniform in dimension by grinding the surface. A notch was introduced in the specimen by means of a diamond saw.

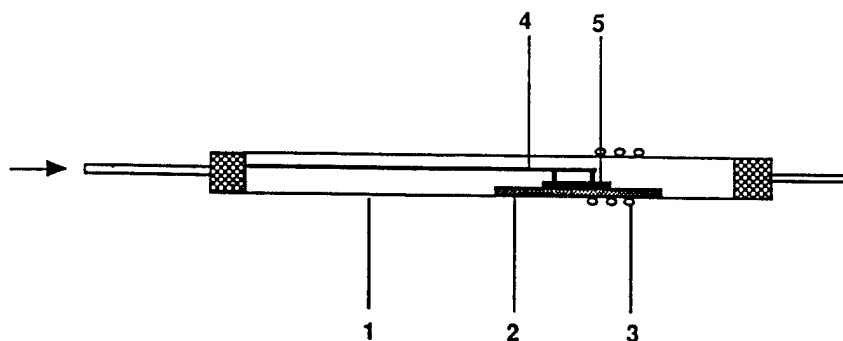


Fig. III. 1 Schematic diagram of the set up used for micropyretic synthesis in an inert atmosphere. The different components of the set up are 1. a quartz tube 2. an alumina boat 3. an induction coil 4. thermocouples and 5. specimen.

The fracture toughness was measured by the four point bend technique [68]. A Cambridge SEM equipped with a Princeton Gamma-Tech detector was used for the examination of the fracture surface and the microstructure. X-ray diffraction was carried out in a Philips diffractometer (model: X'pert) employing a Cu tube operating at 40 kV and 55 mA. The porosity of the combusted samples was measured using image analysis. Porosity values were used for calculating the density of the combusted material.

Specimens for TEM observation were made by two different techniques. The specimens synthesized with preheat were found to be more dense and thin foils for TEM examination could be made in these using the twin jet electropolishing technique using an electrolyte containing 10% perchloric acid and 90% methanol. The electrolyte temperature was kept below 240 K. In the case of specimens synthesized without preheat, due to the relatively higher amount of porosity, thin foils could not be made by the twin jet electropolishing technique. Specimens were, therefore, made by dimple

grinding followed by ion milling in a Gatan ion mill. Thin foils were examined in a Philips CM 20 electron microscope equipped with an EDAX microanalysis system.

III. 3 Results and Discussions

III. 3. 1 Density and Porosity

The compositions examined in this study are shown in Table III. 2. It may be noted that in the case of the binary and the ternary alloys, Ni powder of $\sim 3\mu\text{m}$ size was used. In the case of the quaternary alloy two different Ni powder sizes were used, namely $3\mu\text{m}$ and -100 mesh. These alloys have been referred to in the rest of the text as alloy 1 (NiAl), alloy 2 (Ni₅₀Al_{49.5}Fe_{0.5}), alloy 3 (Ni₅₀Al_{48.5}Cr_{0.5}Fe_{0.5}V_{0.5} made with $\sim 3\mu\text{m}$ Ni powder) and alloy 4 (Ni₅₀Al_{48.5}Cr_{0.5}Fe_{0.5}V_{0.5} made with -100 mesh Ni powder). Table III. 2 shows the green density and the final density values. The compacted samples had good handling strength. This was not surprising in view of the fact that the green density was high and the compact could be cold pressed to more than 60 % of the theoretical density.

Table III. 2 Alloy compositions and densities

| Alloy | Composition | Green Density | Density of the synthesized alloy as % of theoretical density |
|-------|--|---------------|--|
| 1 | Ni ₅₀ Al ₅₀ | 60 | 93 |
| 2 | Ni ₅₀ Al _{49.75} Fe _{0.25} | 65 | 92 |
| 3 | Ni ₅₀ Al _{48.5} Cr _{0.5} Fe _{0.5} V _{0.5} | 64 | 90 |
| 4 | Ni ₅₀ Al _{48.5} Cr _{0.5} Fe _{0.5} V _{0.5} | 65 | 87 |

III. 3. 2 Mechanical Properties

Hardness and fracture toughness were the two mechanical properties determined for the synthesized alloys. In the case of the quaternary alloy, mechanical property evaluation was carried out in the case of specimens made with the 3 μm Ni powder (alloy 3). The specimens made with larger Ni powders (alloy 4) were very porous and were therefore not found to be suitable for the determination of mechanical properties. No preheating before synthesis was done for specimens which were tested for mechanical properties. Specimens made by preheating were found to undergo considerable distortion in shape and were not used for property evaluation although these appeared to be denser. The hardness values for three alloys are shown in Table. III. 3. The hardness value of NiAl compares well with that determined in the case of NiAl made by other fabrication techniques. It can be seen that all three alloys have hardness values which are very close. The ductility of the alloys measured in compression are indicated in Table III. 3. The ductility is highest in the case of the alloy 2 and the lowest in the case of

Table III. 3 Porosity, Grain size, Hardness and Fracture Toughness of the Alloys

| | Porosity | Grain Size (μm) | Hardness (VPN) | Fracture Toughness ($\text{M Pa m}^{1/2}$) |
|---|----------|---------------------------------|-------------------|--|
| 1 | 7 | 30 | 310 | 6.0 |
| 2 | 8 | 28 | 325 | 9.5 |
| 3 | 10 | 29 | 330 | 8.5 |

unalloyed NiAl. The value of fracture toughness of the unalloyed NiAl observed in this study (6.0 $\text{MPa m}^{1/2}$) agrees well with that reported for this alloy made by other techniques [69] despite the presence of the pores. Earlier studies have shown that in the case of NiAl, ductility depends on the stoichiometry and that stoichiometric NiAl has the highest ductility as

compared with offstoichiometric compositions. Good fracture toughness obtained in this study despite the presence of pores is indicative of the fact that the exact stoichiometry which was aimed for had been achieved. Processing techniques like arc or induction melting often lead to loss of Al because of its lower melting point when compared with nickel. The process of micropyretic synthesis ensures good microstructural homogeneity and ease of achieving the desired composition. The fracture toughness was found to improve by the addition of small amounts of Fe, Cr and V (Table III. 3). The increase in fracture toughness was substantial when Fe was the only alloying addition.

Fracture was found to be a mixture of intergranular and transgranular modes (Figure III. 2). Although intergranular fracture could also be seen in all three alloys (indicated by arrows in Figure III. 2), most of the regions on the fractured surface showed a transgranular mode of fracture. The observation of a predominantly transgranular mode of fracture can be attributed to the fact that fracture had occurred during toughness testing. The fracture mode was found to be transgranular during toughness testing as opposed to intergranular which was seen during monotonic tensile testing [15, 16].

The appearance of the grains around the pores was similar to those away from the pores. The examination of the fracture surfaces did not present any evidence to suggest that the pores assisted crack nucleation or crack propagation. The presence of porosity may lead to a substantial increase in the fracture energy due to crack deflection [71]. The Young's modulus, however, decreases with increasing volume fraction of pores eventually leading to a decrease in the value of the fracture toughness and the strength [71]. It has been observed in some studies that the pores can indeed lead to an increase in

the value of fracture toughness e.g. in refractories, sapphire with small voids and reaction sintered Si_3N_4 bodies with substantial porosity [71]. In terms of deformability, NiAl bridges the gap between metals and ceramics [72] and

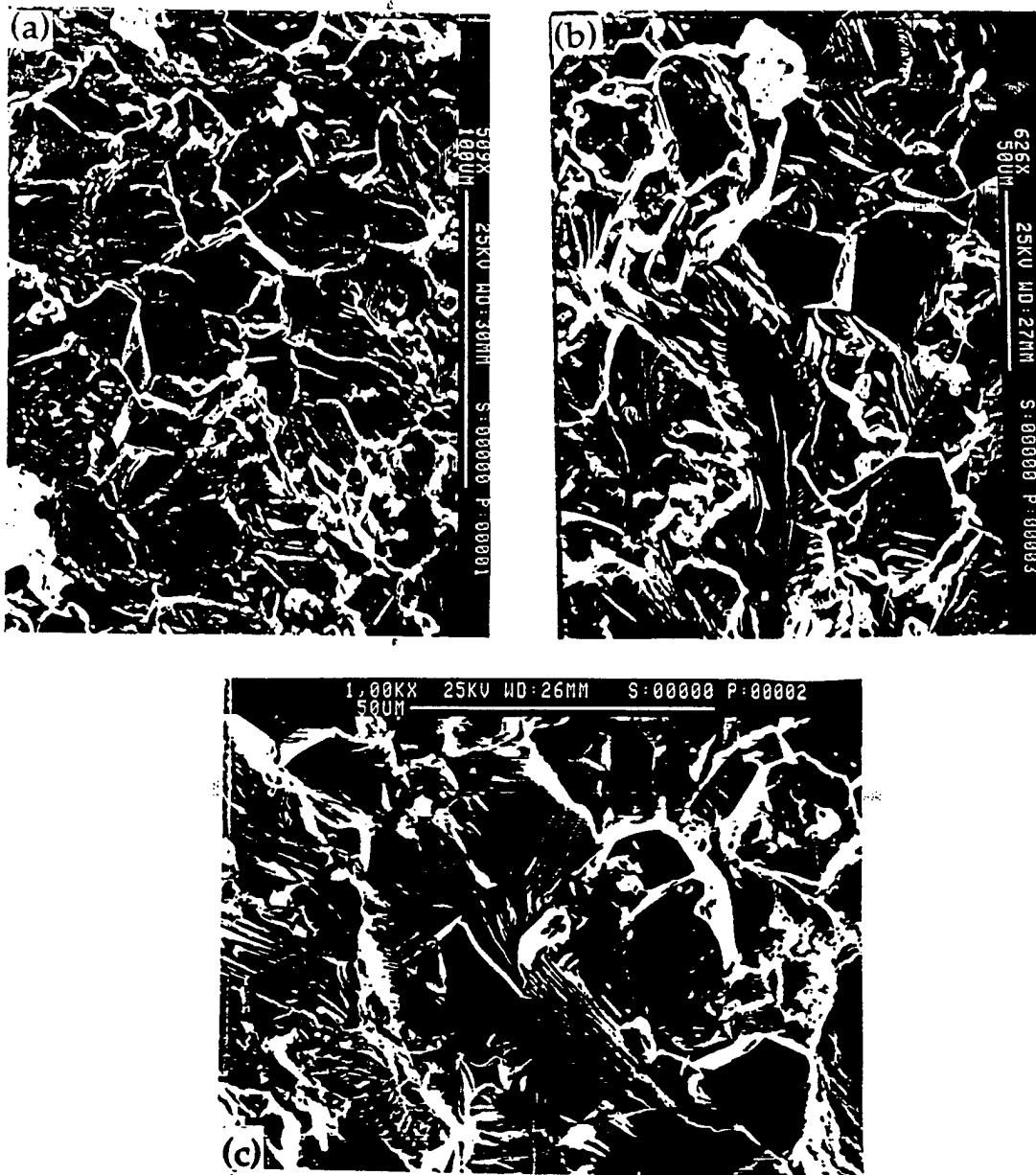


Fig. III. 2 Fractographs of the different alloys (a) alloy 1 (b) alloy 2 and (c) alloy 3, showing a mixture of intergranular and transgranular failures.

hence observations similar to the aforementioned increase in fracture toughness in the case of the ceramic materials can be made in the case of

NiAl. Li et al. [12] have observed high fracture toughness in the case of TiBCu alloys made by micropyretic synthesis when compared to sintered TiB₂, despite the presence of pores. Free Ti was present in some of the composition as a ductile phase in their study. They have attributed the increase in fracture toughness of the alloys due to the ductile phase and the decrease to the presence of porosity in the system. Li et al. [12] modeled the fracture toughness of the composite by considering the additive influence of the ductile phase reinforcement (Ashby model) and the residual porosity (exponential model). It is clear from their study and several other studies that with an increasing volume fraction of pores the strength of the synthesized alloy goes down. In this study, the increase in fracture toughness of the ternary and the quaternary alloys appears to be more due to the ductilization of the alloys.

III. 3. 3 Microstructure of Specimens Synthesized without Preheat

III. 3. 3. 1 Microstructure before Deformation

The microstructure of the alloys synthesized without preheat was examined with optical microscopy, SEM and TEM. The microstructures of the three alloys were identical when examined in the optical microscope and comprised equiaxed grains. The grain interior as well as the grain boundary appeared devoid of any second phase under the optical microscope. The small alloying additions did not bring about a very noticeable change in the grain size (Table III. 3). Figure III. 3 shows the microstructure of alloy 3. It is possible to have a difference in microstructure of micropyretically synthesized materials due to different amounts of preheat before combustion. This aspect will be discussed in more detail later in this report. In addition to the grains, pores of different sizes could be seen (Figure III. 3) in the microstructure of all

the alloys. The volume fraction of the pores was calculated by image analysis. The porosity values were used for determining the density of the synthesized alloys. The estimated porosities are indicated in Table III. 2.



Fig. III. 3 Optical microstructure of alloy 3 after synthesis without preheat.

The formation of a martensitic phase has been observed in NiAl alloys containing at least 61% Ni [73]. Although in this study, the amount of Ni was never so high in any of the alloys, the three alloying additions could have brought about the formation of the martensitic phase had these raised the M_s temperature significantly. However, X-ray diffraction from the alloys indicated the presence of the B2 phase alone. A very minor difference in the lattice parameter of the B2 phase present in the three alloys could be seen. Some studies have shown that Ni_3Al can have small amount of teragonality when present in certain superalloys [74]. Tetragonality in the B2 lattice can also develop as a result of alloying. However, selected area electron diffraction

(SAD) carried out in the TEM and X-ray diffraction did not reveal the presence of tetragonality. Convergent beam electron diffraction (CBED) is being carried out to detect the presence of tetragonality in the B2 lattice of the quaternary alloy. These results will be presented elsewhere [75].

TEM studies were carried out on specimens synthesized with and without preheat. These examinations were carried out with the specific aim of finding the nature of the defects, the identification of the phases by electron diffraction and estimation of composition of the microstructure using a very fine beam of electrons (microanalysis). Compositional microanalysis at such a fine level is likely to yield composition variations produced during the process of synthesis. Such studies on micropyretically synthesized materials have not been carried out before. Examinations of this nature are very important because the product is being made from powders of the elements by a process which involves mixing of the elements, melting and solidification, the three processes occurring over a very short period of time and over a very short distance under a very steep thermal and compositional gradient.

TEM examination of the specimens of alloy 3 indicated the presence of the dislocations of various types. Figure III. 4 (a) shows a bright field electron micrograph displaying mostly dislocations of the $b = \langle 100 \rangle$ type. In addition to these dislocations which were most numerous, dislocations could also be seen of the $b = \langle 111 \rangle$ type. These dislocations (indicated by an arrow) gave the characteristic double image as seen in other studies [76]. Also seen were dislocation loops and these were found to be dislocations of the $b = \langle 111 \rangle$ type (Figure III. 4 (b)). No substantial difference was observed in the nature or the arrangement of dislocations in the three alloys synthesized without preheat.

The nature of the dislocation was similar to that observed in the case of alloys made by other fabrication techniques [76-78]. The nature of the dislocations was found to be identical to those seen in the case of unalloyed NiAl indicating that the alloying additions did not bring about a substantial change in the nature of the dislocations. It was possible to see particles in some of the grains. The occurrence of these particles was very rare and electron diffraction revealed that these are complex oxides of Al, Ni and V. The grains were free



Fig. III. 4 (a) & (b) Bright field micrograph showing the arrangement of dislocations in the alloy 3 synthesized without preheat. Dislocations with $b=\langle 100 \rangle$ and $b=\langle 111 \rangle$ can be seen.

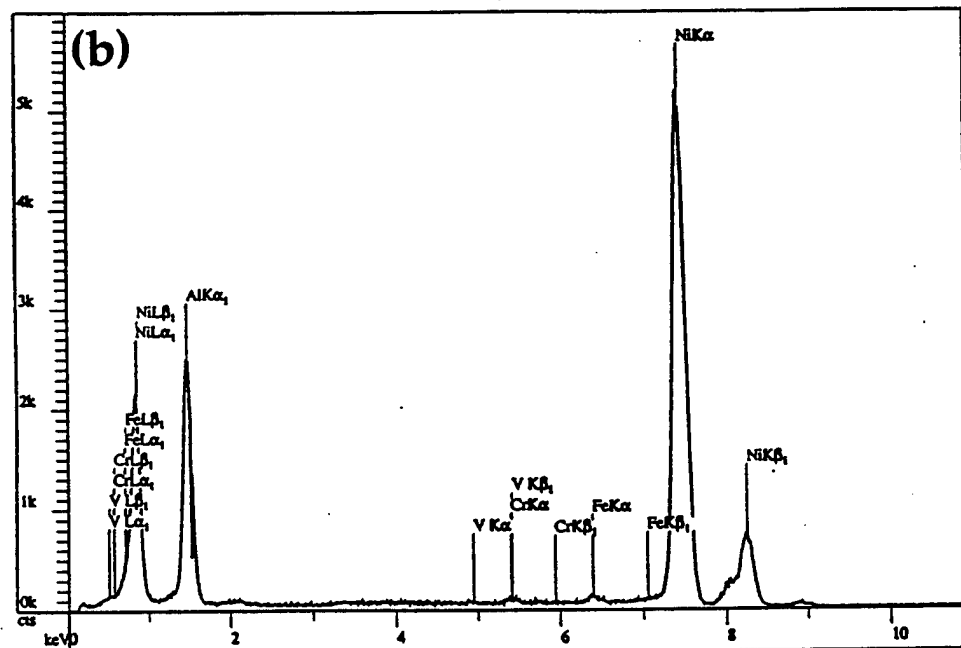
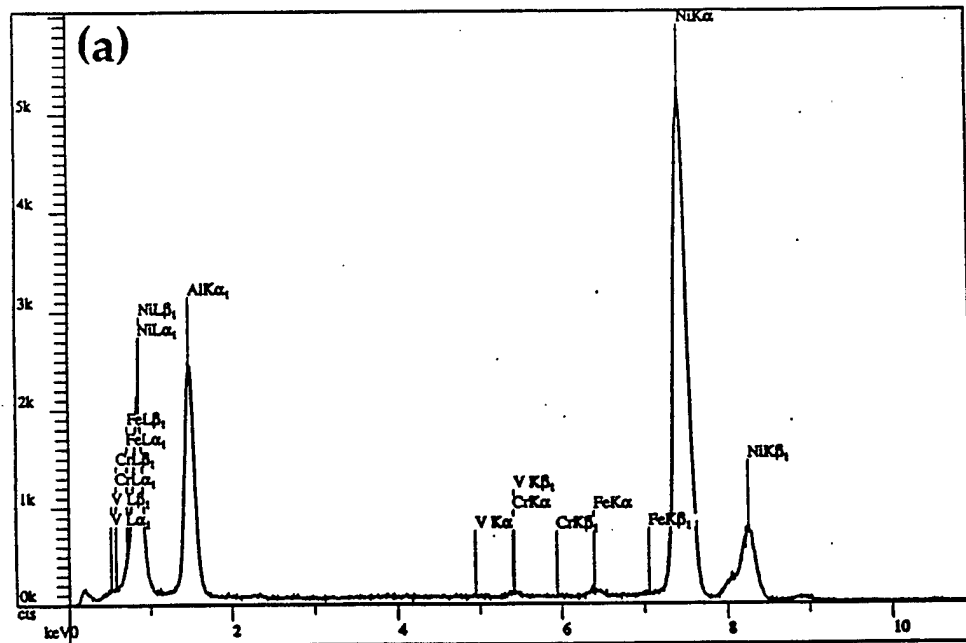
from any kind of mottling. These observations were suggestive of the fact that the alloying additions could be accommodated in the NiAl lattice as substitutional solid solution elements. The solubility of Cr in NiAl is known

to be low (1.5 wt % Cr) [79, 80]. This limit has not been exceeded in this study. The addition Fe was well within solubility limits in NiAl [81, 82]. The solubility of V is about 5 at% when substituted for Al and nil when substituted for Ni [83, 84]. In the alloys examined in this study, V substituted for Al and therefore it should not normally precipitate out although formation of a V bearing grain boundary precipitate phase was observed in the case of the preheated specimen. This aspect will be discussed later. EDS point count analysis at the center of the grains as well as at the boundary did not reveal any noticeable difference in the composition of the two regions (Figure III. 5(a) and (b)). The grain boundaries were free of any particles of a second phase (Figure 5(c)). These observations are indicative of the fact that the extent of segregation of the alloying additions during the process of synthesis is rather small at least in the specimen where preheating has not been done. The microstructure of alloy 2 and alloy 1 were very identical to that of the aforementioned microstructure of the alloy 3. The nature and arrangement of the dislocations were also identical. The grain boundaries did not contain particles of a second phase.

III. 3. 3. 2 Microstructure after Deformation

Darolia et al. [77] have observed an increase in ductility of the NiAl alloys due to addition of small amounts of Fe, Ga and Mo and have attributed the increase in ductility to the dislocation core structure interactions and electronic structure modifications [77]. In this study the increase in fracture toughness seems to stem from the enhancement of the ductility of the grains due to the aforementioned reasons. Higher ductility in NiAl has been found to be associated with higher fracture toughness [69]. Darolia et al. [77] in their study did not observe any difference in the arrangement of dislocations in the

unalloyed and the microalloyed NiAl. In this regard, the observations made in this study are identical to that of Darolia et al [77]. The alloying additions to NiAl made in this study, particularly Cr and V, are good choices for lowering the ordering energy of NiAl, thereby making $\langle 111 \rangle$ slip easier [65,85]. The



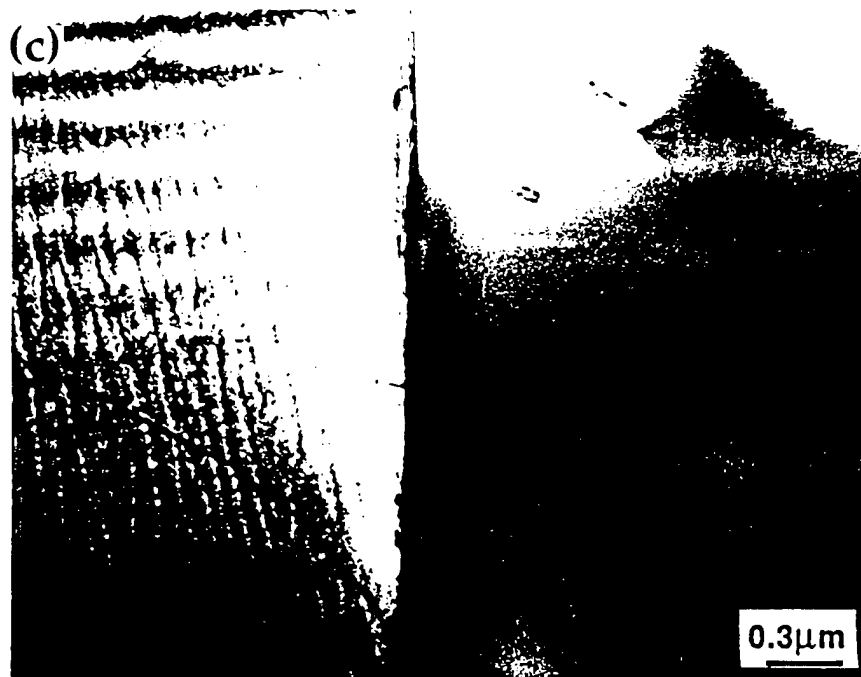


Fig. III. 5 (a) EDS spectrum from the grain interior. (b) EDS spectrum grain boundary showing the similarity in composition of the two regions in a specimen of alloy 3 synthesized without preheat. (c) Bright field micrograph showing a grain boundary. No second phase particle can be seen at the boundary.

observations made in this study as well as in some other recent studies, indicate that $\langle 111 \rangle$ slip does not occur in NiAl despite the addition of Cr and V [79,86]. Similarly, the addition of Fe also did not bring about the occurrence of $\langle 111 \rangle$ slip, an observation consistent with those made in other studies [77, 82].

III. 3. 4 The Effect of Preheat

A separate set of experiments were carried out to see the effect of preheat on the microstructure. The microstructures of specimens preheated at the following temperatures were examined after the synthesis - 1. 513 K and 2. 673 K. These microstructural examinations were carried out with the specific aim

of identifying the effect of preheat on the following factors- porosity, grain morphology and the nature of the phase formation.

Preheat was found to have a significant effect on the porosity of the specimen. With increasing preheat, the amount of porosity was substantially reduced. This behavior is not surprising in view of the fact that the preheat has the effect of increasing the extent of melting during the synthesis process as discussed. With increasing preheat, the nature of the porosity distribution was also found to change. While in the unpreheated samples the pores were small (average size = 15 μm) and the pores were uniformly distributed, in the samples with significant amount of preheat the pores were found to be larger and were not uniformly distributed.

Li et al. [66] have considered the effect of preheating on the combustion temperature and velocity. It could be noted by Li et al. [67] that up to an initial temperature of 920 K, the adiabatic reaction temperature remained the same with the only change being the molar melted fraction of the product phase from 42% to 100%. This contention is consistent with the observations made in this study that the amount of the molar melted fraction was found to increase with the amount of preheat. Normally, an increase in the initial temperature increases the enthalpy in the system and leads to an enhancement in the propagation velocity although the combustion temperature remains the same. The increase in the enthalpy on account of increasing the initial temperature is only used by the system to increase the melted fraction of the product phase. Thus, the temperature is noted to remain constant even though the enthalpy and the propagation velocity are increased.

The microstructure was found to change substantially with preheating in both the alloys. The microstructure of the NiAl specimen combusted without preheat has equiaxed grains (Figure III. 3). As the extent of preheat increased, the microstructure was found to change from equiaxed to dendritic. Figure III. 6(a) shows the microstructure of a specimen which has been combusted after preheating the specimen to a temperature of 513 K. This microstructure when compared with that of a unpreheated specimen shows some differences. At many places, the grains have a dendrite like appearance which is primarily seen in the form of curved boundaries. These will be referred to as dendritic equiaxed grains. Some of the dendritic equiaxed grains seemed to be internally divided into sub-grains by boundaries, the nature of which is not known. The size of the grains was found to vary and the average size of the dendritic equiaxed grains was found to be approximately 40 μm which is larger than that in the case of the unpreheated samples. On further preheating of the specimen to 673 K, the microstructure changed to a completely dendritic morphology as shown in the Figure III. 6(b). The change of the microstructure from equiaxed to dendritic is not only indicative of increased fraction of the melting product but also different conditions of solidification after synthesis. The presence of dendritic microstructure was suggestive of extensive melting and solidification at a fairly slow rate. Li et al. [74] have observed solidification at rapid rates during synthesis under conditions which make combustion unstable. In the present study, since these experiments were carried out in particle size ranges which give rise to stable combustion, the dendritic microstructure observed was very different from that observed by Li et al. [13] in their studies.

A detailed investigation of the microstructures of the specimens

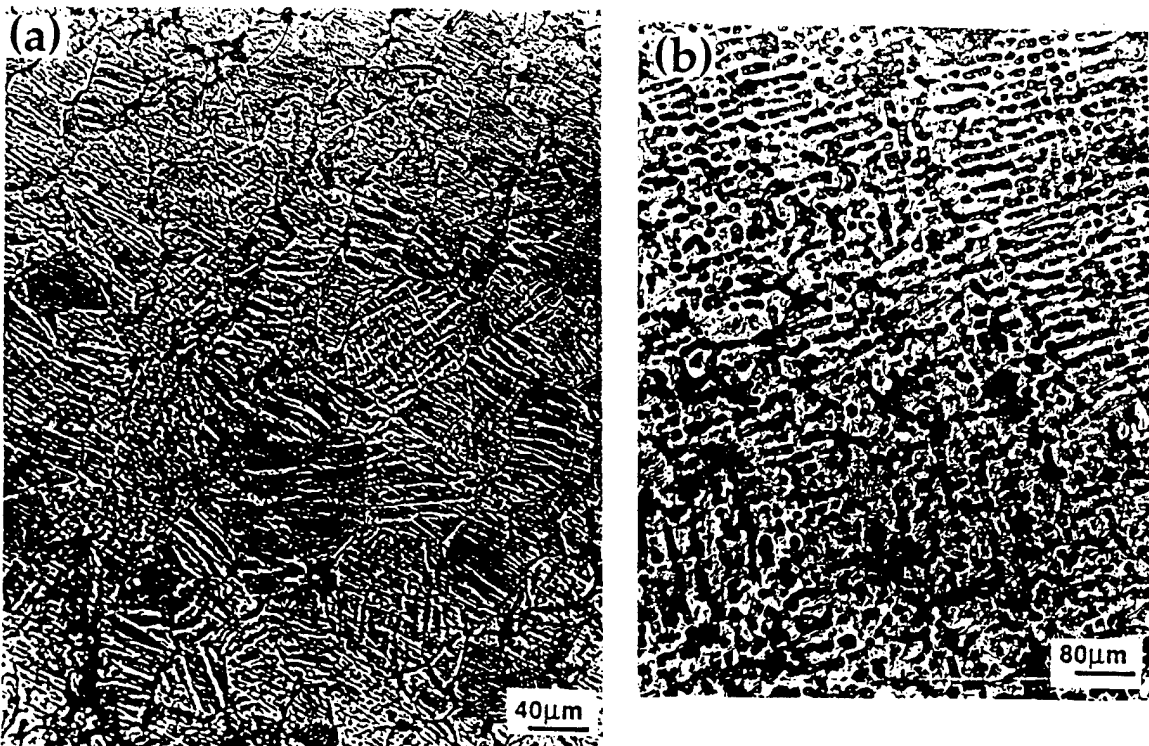


Fig. III. 6 Optical micrograph showing the microstructures of alloy 3 synthesized after different amounts of preheat (a) 513 K and (b) 673 K.

synthesized after preheating was carried out in the electron microscope. In the case of alloy 1, the grains were found to contain some dislocations (Figure III. 7(a)). These were identified to be of the $b = \langle 100 \rangle$ type and were mostly found on the $\{100\}$ slip planes. The bent nature of these dislocations was suggestive of the fact that these are glissile dislocations. It was also possible to see some particles inside the grains. Electron diffraction from these particles revealed that these particles are of a complex oxide of Al and Ni. The presence of no other phase could be seen inside the grains or at the grain boundaries (Figure III. 7(b)).

In alloy 2 the microstructure was identical to that of the alloy 1 in that it comprised the single phase matrix (Figure III. 8(a)). It was possible to see stray

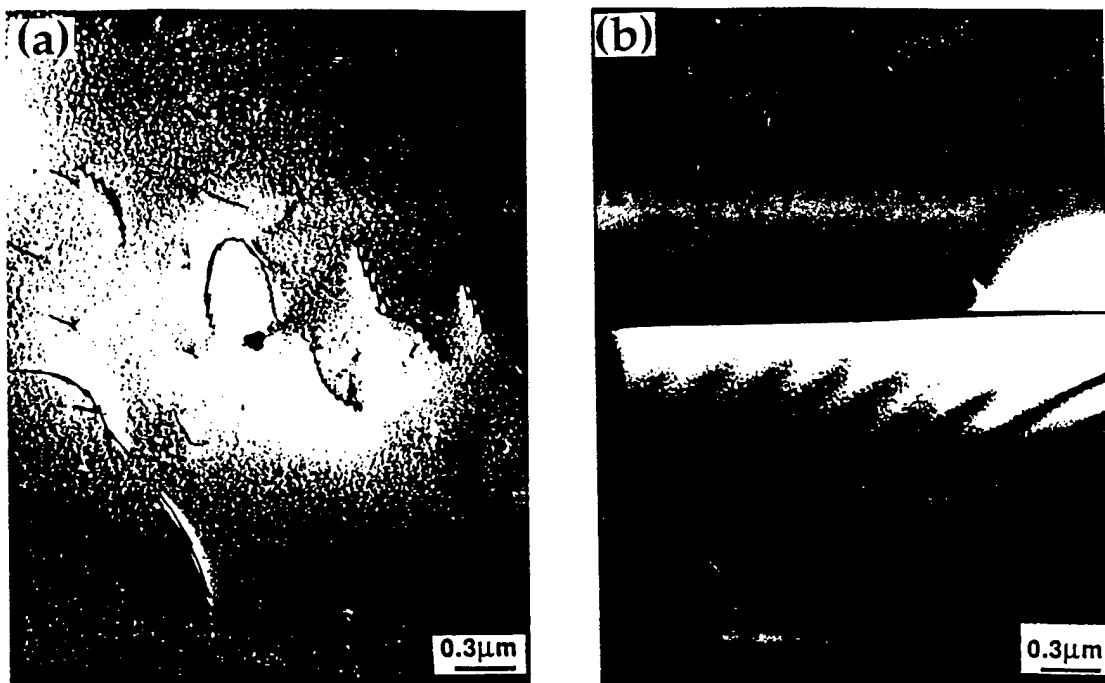


Fig. III. 7 (a) Bright field electron micrograph showing dislocations of $b=\langle 100 \rangle$ type in alloy 1 synthesized after preheating. Particles of a complex oxide phase can also be seen. (b) Bright field electron micrograph showing a grain boundary. No particles can be seen at this boundary.

particles in some grains. The number of such particles was rather small and these could not be seen in all the grains. These were similar in identity to those seen in the other alloys. It was possible to see a wide variety of dislocations inside the grains including dislocation loops (Figure III. 8(b)). Several types of dislocation loops have been observed in NiAl [69]. The Burgers vectors of these dislocation loops is $\langle 100 \rangle$ and these dislocations are edge dislocations lying on the $\{001\}$ plane. The loops observed had rounded corners which is very common in NiAl [69] and have their segments parallel to the $\langle 100 \rangle$ direction. Parallel dislocations of the $\langle 111 \rangle$ type could also be seen in large numbers (Figure 8 (a)). Although, these were mostly screw in nature, these could undergo cross slip, generating edge segments (Figure III. 8(c)). This led to the generation of dislocation debris which can also be seen in Figure III. 8(a)). The grain boundaries in this alloy were found to be clean

and devoid of any particles (Figure III. 8(c)). A point EDS count at the boundary as well as inside the grains indicated that the composition of these regions were almost identical. This is indicative of the fact that there is no large scale segregation of Fe during the synthesis process.

TEM analysis of alloy 3 indicated the presence of small particles inside the grains. These particles were complex oxides of the type seen in the other two alloys. The number of these particles was very small and there were grains where these could not be seen at all. In addition to these particles inside the grains, it was also possible to see particles at some of the grain boundaries (Figure. 9(a)). Electron diffraction from these particles indicated that these are of the $V(FeCr)$ phase. A point EDS analysis from these particles is shown in Figure 9(b). It can be seen that the particles are of a vanadium rich phase. These had a plate shaped morphology.



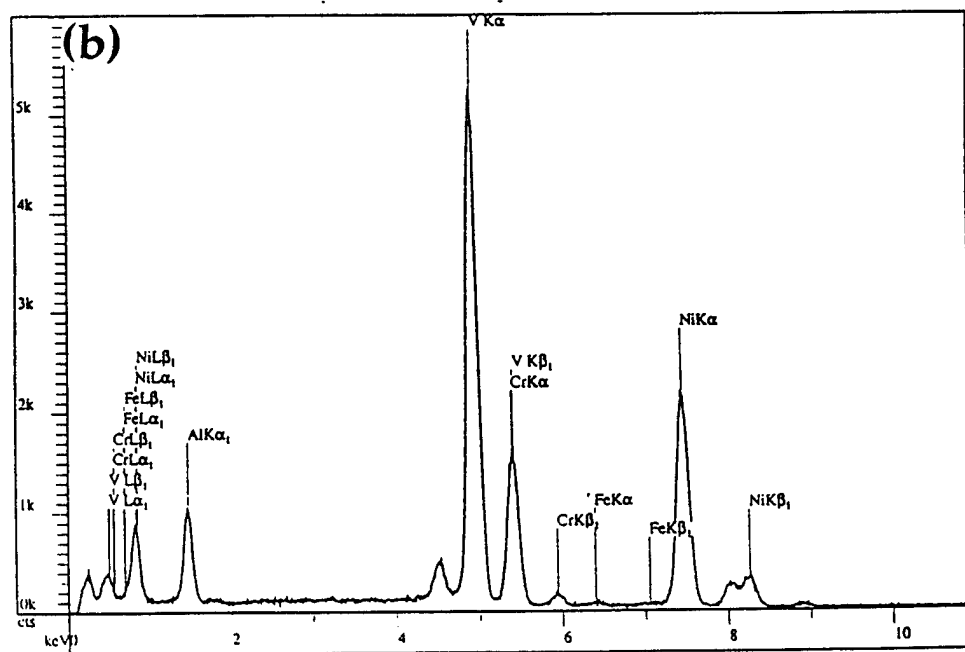


Fig. III. 8 (a) Bright field electron micrograph showing screw dislocations of $b=\langle 111 \rangle$ types. Debris of screw dislocations, jogs leading to the formation of edge dislocations and particles of the complex oxide phase can be seen in the micrograph. (b) Bright field electron micrograph showing the presence of dislocation loops. (c) Bright field electron micrograph showing a grain boundary devoid of any particles.

Quaternary alloy of the composition examined in this study has not been studied before. It is therefore, not possible to compare the nature of the precipitates with those seen previously. An EDS analysis close to the grain boundaries also indicated that despite the presence of these particles the composition of the regions close to the grain boundary were almost identical to those present at the grain interior. In many instances piles of dislocations were found to emanate from the grain boundaries (Figure III. 9(c)). The nature of the dislocations was found to be very similar to those seen in the case of the other two alloys. Mostly dislocations with Burgers vector $b=\langle 100 \rangle$ were seen. These formed arrays in many instances with the arrays having a tendency to intersect each other (Figure III. 9(d)). Screw dislocations giving the

typical double image (Figure III. 9(e)) and dislocation debris and loops could also be seen at many places (Figure III. 9(c)).

The specimens examined in this study indicate that dislocations are always present in the alloy in the as synthesized state whether combusted with or without preheat. The dislocations could have originated from three sources namely (1) growth dislocations (2) dislocations originating due to the stress developed during the process of synthesis and (3) accidental introduction during thin foil preparation. A survey of the microstructures of the as cast NiAl suggests that dislocations do form during the process of casting [87]. However, the density of dislocations encountered in a as cast state is less than that observed in this study. It is well known that micropyretic synthesis occurs under a steep temperature gradient and can therefore lead to the generation of severe stresses during the process of synthesis. The amount of dislocations present in the specimens obtained after preheat were more in number as compared to those present in the unpreheated specimen. This lends support to the fact that many of these dislocations may be growth dislocations. It is also interesting to compare the extent of segregation on a microscopic scale as a function of preheat. It is more meaningful to do this comparison in the case of the multicomponent alloy. Observations made in this study suggest that the microstructure generated in the specimen without preheat had fewer or no second phase particles at the grain boundaries as compared to those seen in the case of specimens with preheat. This is presumably because of the fact that in the case of specimens without preheat, the formation and solidification of the NiAl phase occurs at a very fast rate allowing very little time for segregation of the elements to the grain



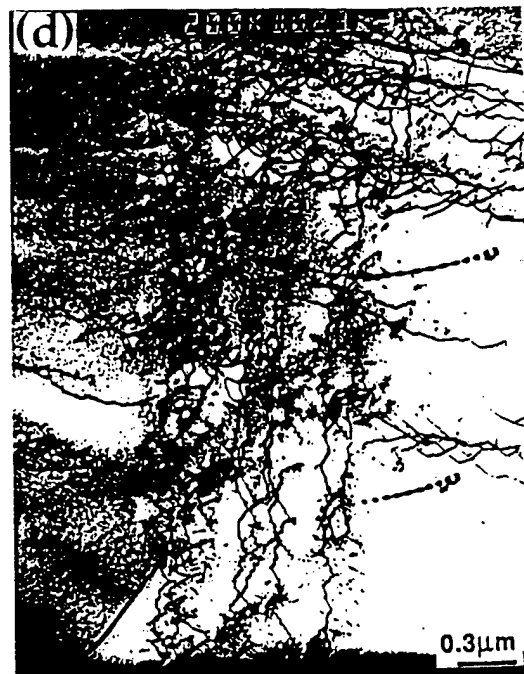


Fig. III. 9 (a) Bright field electron micrograph showing particles of the V(FeCr) phase at the grain boundary of a specimen of alloy 3 synthesized after preheating. (b) EDS spectrum from the particles at the grain boundary indicating that these are rich in V. (c) Bright field electron micrograph showing an array of dislocations with dislocation debris emanating from a grain boundary. (d) Bright field electron micrograph showing interacting arrays of $b=\langle 100 \rangle$ type dislocations. Screw dislocations with double image can also be seen. (e) Bright field electron micrograph showing a long screw dislocation of $b=\langle 100 \rangle$ type pinned at several places.

boundaries and formation of the second phase particles. In the case of specimens made with preheat, the specimens cooled down more slowly allowing enough time for segregation and formation of the second phase particles at the grain boundaries.

The effect of preheat on grain size was examined. It could be seen that increasing the amount of preheat has the effect of increasing the grain size although a comparison of the grain size was difficult because of the fact that in a dendritic grain morphology, the grain size is very difficult to measure. It could be seen that the grain size increased with increasing amounts of preheat. The reason for this occurrence is the fact that with increasing preheat, the cooling rate after combustion decreases. A lower cooling rate normally results in a lower undercooling and fewer nucleation events. As a result, larger grain sizes are observed for specimens which have been preheated more.

III. 3. 5 Effect of Diluents and Effect of Particle Size

The velocity of propagation of the reaction front and peak temperature achieved are indicated for the different compositions in Table III. 4. These measurements have been carried out in an inert atmosphere. The velocity measurements have been carried out for all the three compositions with fixed particle sizes in order to see the effect of the diluents on these parameters. It was observed that with the addition of the diluents, the velocity of the front increased slightly. In order to see the effect of particle size, the Ni particle size alone was changed in the case of the multicomponent alloy. The velocity of the front was found to decrease with the increase in the Ni particle size (Table III. 4). The effect of diluents on the micropyretic synthesis of NiAl has been

examined in considerable detail by Li et al. [66]. In their study, they have concluded that an increase in the amount of the diluent decreases the exothermic energy, hence, the combustion temperature and velocity are expected to decrease with the addition of the diluent. They showed that an increase in the amount of diluents from 5 at% to 15 at% reduced the combustion temperature from 1895 K to 1862 K, and decreased the propagation velocity from 0.167 m/s to 0.146 m/s. The effect of the diluents will depend on their nature and the amount of the diluents. It has been

Table III. 4 Combustion temperature and Propagation velocity

| Alloy | Combustion temperature K | Propagation Velocity m/s |
|-----------------------|--------------------------|--------------------------|
| 1 | 1905 | .20 |
| 2 | 1910 | .30 |
| 3 | 1915 | .35 |
| 3 (40 μm) | 1900 | .10 |

observed in this study, as well as a companion study [88], that small additions of ternary alloying elements can lead to the stabilization of the combustion front and lead to an increase in the velocity of the front. Li et al. [66] in their theoretical study have examined the influence of adding NiAl as a diluent on the rate of combustion and concluded that the addition of NiAl has the effect of slowing down the combustion process. In this study, however, the addition of the diluent had the effect of accelerating the combustion front. This may be because of the fact that NiAl, as diluent, is also the product of the synthesis process and therefore unlikely to participate in the process of synthesis, whereas the diluents like Fe, Cr and V are active participants in the process of

combustion reaction. Further, by addition of the diluents like Fe, Cr and V, the fluidity as well as the thermal conductivity is effected. An increase in the fluidity of the first melting Al would make it easier for it to pass through the intricate pores in the samples and to contact the nickel particles to react with these.

Li et al. [66] have reported that when smaller sized nickel powder particles were used for making the green samples, the combustion wave propagated without any preheating [66]. However, for samples made with larger nickel powder particles ($< 142 \mu\text{m}$), preheating was required. This happened because of the fact that when a small particle size was used there was larger surface area present. This resulted in more contact between the Ni and Al powder particles leading to higher reaction surface and complete propagation of the reaction front. In case of larger Ni particles, surface contact between the Ni and Al particles is less leading to lower thermal conductivity, which slows down the propagation of the front. An increase in the particle size leads to a decrease in the plateau temperature during the synthesis process because of the longer time required for the melting of the larger Ni particles [66]. The peak temperature is also lower in the case of the larger Ni particle size [66]. In this study, it could be observed that the combustion front was unstable and extinguished itself when NiAl was combusted using a nickel powder of the size -100 mesh, an observation similar to that made by Li et al. [66]. However, when Fe, Cr and V were added as diluents, the combustion proceeded to completion even when a larger Ni powder size (-100 mesh) was used. As stated earlier, this is presumably due to the following three factors; increase in the fluidity as well as the thermal conductivity and increase in exothermicity by the addition of the diluents. The velocity of the

front was, however, smaller in the case of alloy 4 as compared to that in the case of alloy 3 showing the influence of the Ni particle size.

III. 4 Conclusions

Based on the observations made in this study, the following conclusions are made

1. Alloying additions like Cr, V, and most importantly Fe in very small amounts can improve the fracture toughness of the micropyretically synthesized alloys noticeably. The increase in fracture toughness is due to the enhancement in ductility of the alloys brought by these alloying additions. The fracture mode of the alloys, however, was not significantly influenced by these alloying additions.
2. The rate of micropyretic synthesis is influenced considerably by the small additions of Fe, Cr and V which increase the rate noticeably.
3. The microstructures of the three alloys were not found to be substantially different when synthesized under the same conditions of preheat. Unlike composition, preheat was found to substantially influence the microstructure. Increasing amounts of preheat transformed the grain morphology from equiaxed to dendritic. In addition to the morphology of the grains, preheating also influenced the extent of segregation of the alloying additions and the phase formation at the grain boundaries.
4. The compositional homogeneity across grains of the microstructures was found to be very good when examined by EDS. The nature of the dislocations was found to be similar to that observed in conventionally produced NiAl.

IV. MICROPYRETIC SYNTHESIS OF NiAl CONTAINING Ti AND B

The effect of the two alloying additions, Ti and B, on the process of synthesis and the microstructure of the alloy has been examined. It has been observed that the combustibility of the quaternary alloy is very good despite the addition of substantial quantities of diluents because of an additional combustion reaction between Ti and B. The microstructure of the alloy has been found to comprise the NiAl and the Ti B₂ phases. The microstructure of this alloy has been compared with that of unalloyed NiAl and some interesting differences have been observed. The effect of preheat prior to synthesis has been examined. It has been observed that preheat can not only change morphology of the phases, it can also influence the nature of the phases present in the alloy. The mechanism of synthesis of the two phases microstructure from elemental powders has been established by stopping the combustion front and by carrying out detailed microstructural characterization around the stopped combustion front.

IV.1 Introduction

Several alloying additions have been done to NiAl to improve its ductility. Ti is known to impart ductility to B₂ structures [89]. Ti additions have been done to NiAl to improve ductility of the alloy and some success has been achieved in improving the fracture toughness of the intermetallic compound. Additions of B and Ti in the alloy Fe₃Al has led to the improvement of the high temperature strength and refinement of grain size [90]. In an analogous manner, it is hoped that the addition of Ti and B to NiAl will improve the mechanical properties by forming borides or improving the grain boundary strength [91]. In this study, the micropyretic synthesis of NiAl

with Ti and B additions has been carried out. Diluents have been found to influence the combustibility of the alloys in various ways depending upon the nature of the diluents and their amounts. The effect of the two alloying additions Ti and B on the process of synthesis and the microstructure of the alloy has been examined by determining the peak temperature and the velocity of the combustion front in this study. Despite the fact that Ti is present in a substantially large quantity as a diluent, it has been observed that the combustibility of the quaternary alloy is slightly superior to that of binary NiAl because of an additional combustion reaction between Ti and B. Preheat can have a profound influence on the microstructure of the alloy as has been clearly demonstrated in Chapter III. The effect of preheat prior to synthesis on the process of synthesis of NiAlTiB has been examined. It has been observed that preheat can not only change the morphology of the phases, but it can also influence the nature of the phases present in the alloy and the distribution of porosity. The exact stoichiometry of the alloy studied is $\text{Ni}_{45}\text{Al}_{45}\text{Ti}_8\text{B}_2$.

IV. 2 Experimental

High purity powders (purity and size indicated in Table IV. I) were weighed accurately and mixed in a Spex model 8000 ball mill for twenty minutes without addition of any liquid medium. Subsequently, the mixed powders were pressed into rectangular bar specimens in a double acting press at a pressure of 25000 psi. The pressed compacts were combusted in an inert atmosphere by igniting from one end. The dimensions of the specimen were found to change after synthesis. The fracture surfaces were examined in a SEM. Xray diffraction was carried out in a Siemens diffractometer (model: D500) employing a Cu tube operating at 40 kV and 30 mA. The porosity of the

combusted samples was measured using image analysis. Porosity values were used for calculating the density of the combusted material.

The temperature of the specimen could be monitored by placing thermocouples at different parts of the specimen. Combustion was initiated by heating one end of the specimen by induction heating. In the case of specimen preheated before combustion, preheating of the specimen before synthesis was done in a furnace.

Table. IV. I Purity and Particle Size of the Powders Used

| Element | Purity | Powder size |
|---------|--------|-------------------|
| Ni | 99.7 | 3 μm , |
| Al | 99.5 | -325 mesh |
| Ti | 99.0 | -325 mesh |
| B | 95.9 | 10 μm |

IV. 3 RESULTS AND DISCUSSION

IV. 3. 1 Effect Of Ti and B on the Combustion Process

The rate of the combustion reaction and the combustion temperature are fairly well studied for NiAl [22, 23, 25, 66, 67]. The effect of the size of the Ni particles on the combustion reaction and temperature has also been well studied [66]. The effect of the addition of the diluents on the rate of the combustion process has been examined in some of the studies and it has been shown that the addition of diluents in very small quantities can significantly influence the rate of the combustion process [75, 88, 92]. However, when the amount of the diluents has been increased considerably, the rate of the combustion reaction has been found to reduce substantially. The reason for this observation seems to be the following. The addition of the diluents in very small quantities can lead to a substantial reduction of the green porosity and hence can improve particle compact substantially. The particles of the

diluents being of a different size and size distribution fill the interstices in the green compact. This leads to an increase in the combustibility of the specimen due to better particle contact. However, the addition of the diluent in a large quantity can lead to a reduction of the exothermicity of the combustion reaction itself. In this study, the amount of the amount of the diluent added, particularly Ti, was not small. The slight increase of the reaction velocity and the reaction temperature as compared to binary NiAl meant that the exothermicity of the reaction has increased. Subsequent microstructural examination comprises the NiAl and the TiB₂ phase. The adiabatic temperature of formation of the TiB₂ phase is quite high (Table IV. II). The formation of the TiB₂ phase increases the exothermicity of the combustion reaction in this alloy.

IV. 3. 2 Microstructures and Phases

It has been shown in recent studies that the extent of preheat can have

Table IV. 2 Combustion temperature and Propagation velocity

| Alloy | Combustion Temperature (K) | Propagation Velocity (m/s) |
|---------|----------------------------|----------------------------|
| NiAl | 1905 | .20 |
| NiAlTiB | 1940 | .30 |

Table IV. 3 Adiabatic temperatures and heat of formation (reaction) of some selected exothermic reactions ($T_0 = 298$ K).

| Reaction | $-\Delta H_{298}$ (kJ) | T_{ad} (K) |
|--|------------------------|--------------|
| Ti + 2B \rightarrow TiB ₂ | 315.9 | 3190 |
| Ni + Al \rightarrow NiAl | 118.4 | 1912 |

profound influence on the microstructure and mechanical properties of the micropyrethically synthesized alloys [92, 93]. The extent of preheat has not only been found to influence the morphology of the grains but these have also been found to influence the nature of the phases present [92]. A detailed account of how the extent of preheat influences the aforementioned parameters in the case of the NiAl with Fe, Cr and V addition has been given in chapter III. In this chapter, similar examinations have been carried out in the case of NiAl containing Ti and B. The microstructural examination has been carried out in the case of the specimens obtained without as well as with preheat.

IV. 3. 2. 1 Microstructure Without Preheat

IV. 3. 2. 1. 1 X-ray Diffraction Results

The important intense peaks in the x-ray diffractogram of the specimen obtained without preheat could be indexed in terms of the NiAl phase which has the B2 structure and a lattice parameter of $a = 0.290$ nm. This parameter is slightly different from that of unalloyed NiAl. Ti is likely to substitute for Ni as well as Al in the NiAl lattice [69]. In either case, the substitution will lead to change in the lattice parameter because of the difference in the size of the atoms. The solubility of Ti in NiAl is 5 at% [69]. The addition of Ti to NiAl leads to the formation of the Ni_2AlTi phase once the amount of Ti exceeds the solubility limit. The structure of the NiAl and the Ni_2AlTi phases are very similar. Ni_2AlTi is also known as the Heusler or B' phase and forms by further ordering on the Al sites of the CsCl structure by Ti. In this study the amount of Ti added was less than required for the formation of the Ni_2AlTi phase. It should be noted that only a part of the Ti is going to the NiAl lattice. A substantial part of it is consumed in the formation of the TiB_2 phase. B is

likely to occupy the interstitial positions in the NiAl lattice because of size of the B atom [69]. However, when B is being added along with Ti, it will try to form TiB₂ rather than alloy with NiAl. X-ray diffraction results indicate that TiB₂ is forming, although the amount of TiB₂ does not appear to be very large.

IV. 3. 2. 1. 2 Microstructural Examination

In the case of the NiAl alloy with Ti and B addition, the unpreheated specimen showed a multiphase microstructure comprising a matrix of the NiAl phase (Figure IV. 1). The grains of this phase did not have a equiaxed morphology as seen in the case of NiAl. Instead, the grains had a spherical morphology and at the junction of these grains a mixture of phases appeared to be present. It is interesting to note that the morphology of the grains is spherical. Spherical grain morphologies can be obtained in binary NiAl once specimens have been preheated (see chapter III). It appears that the effect of adding Ti and B on the microstructure of micropyretically synthesized NiAl is the same as preheating of the binary alloy. The effect of preheating is to add additional enthalpy in addition to that obtained by the combustion reaction. This results in a higher volume fraction of the melted product and as a result it solidifies into a dendritic microstructure. In the case of NiAl with B and Ti addition, the effect of the Ti and B is to add additional enthalpy by the formation of the TiB₂ phase. It can be inferred that due to higher heat input, the microstructure changes to the spherical or the dendritic form as compared to the equiaxed microstructure seen in the binary NiAl.

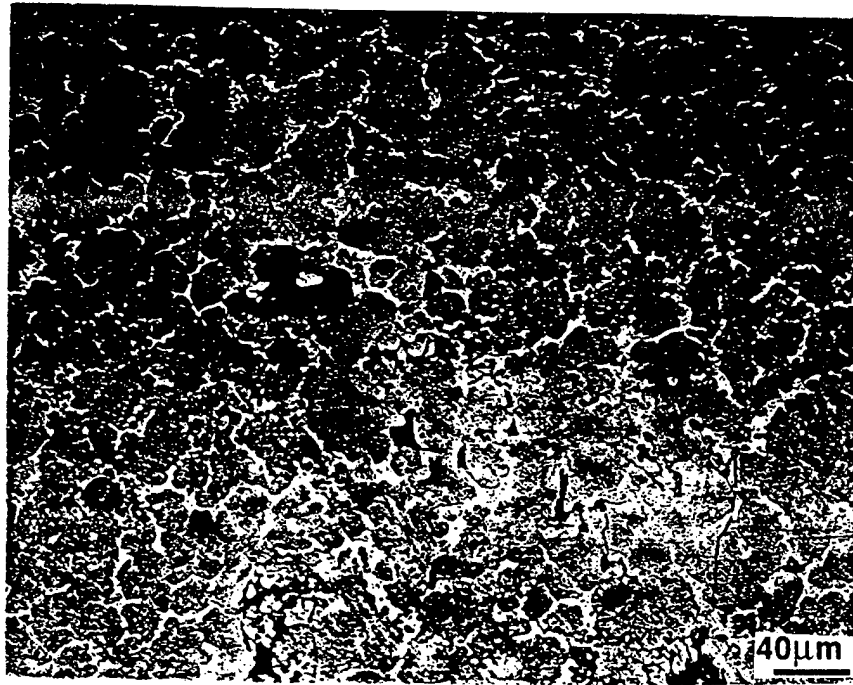


Fig. IV. 1 Microstructure of the NiAlTiB alloy after synthesis without preheat.

IV. 3. 2. 2 The Effect of Preheating on the Microstructure and Nature of the Phases

In chapter III of this report, it has been shown that preheating of the specimen prior to synthesis influences the volume fraction of pores present in the specimen. It has been seen in chapter III that preheating not only influences the morphology of the grains, but also the extent of segregation of the alloying additions in the microstructure. The extent of preheating before synthesis therefore assumes considerable significance, especially in a two phase microstructure of the type encountered in this alloy. In order to examine the effect of preheat, combustion of the specimens was carried out after heating these to 473 K and 623 K in this study.

IV. 3. 2. 2. 1 X-ray Diffraction Results

Analysis of x-ray diffractograms from the samples preheated at two different temperatures indicated that the phases forming were NiAl, TiB and TiB₂. A difference in the lattice parameter of the B2 phase present in the

samples preheated to two different temperatures could be seen. The lattice parameter of the NiAl phase in the unpreheated specimen was found to be higher than that in the preheated specimen. This is because of the fact that in the unpreheated specimen, the post synthesis solidification occurs at a very rapid rate leading to a supersaturation of the NiAl lattice with Ti and B, whereas in the case of the preheated specimen, the extent of melting is much larger. These conditions also call for solidification at a much slower rate. The solidification at slower rate allows the Ti and B to segregate out of the matrix and form the TiB and the TiB₂ phases. It is interesting to note that in the case of Ti and B containing alloys, the identity of the phases forming during synthesis change with preheating. The formation of the TiB phase could not be seen in the unpreheated specimen. In chapter III of this report, it has been shown that preheating of the specimen prior to synthesis has a profound influence on the microstructure. Li et al. [66] have shown in their studies on NiAl alloys that preheating increases the melted volume fraction of the product. An increase in the melted volume fraction of the product is likely to change the extent of solidified microstructure. The formation of the Ni₂AlTi phase could not be observed in the preheated specimen.

IV. 3. 2. 2. 2 Microstructure of the Preheated Specimen

473 K preheat: In the case of the NiAl alloy with Ti and B addition, the preheated specimen showed a multiphase microstructure comprising a matrix of the NiAl phase (Figure IV. 2 (a)). The grains of this phase had a spherical morphology and at the junction of these grains a mixture of phases could be seen. The grains of the NiAl phase showed faults running across the length of the grain. In many grains the faults were found to be running in two directions. These faults were indicative of the formation of the

martensitic phase, however this contention could not draw support from the x-ray diffraction results.

623 K preheat: In the specimens with this extent of preheat the microstructure had a dendritic appearance (Figure IV. 2(b)), with the dendrite boundaries decorated with a second phase. The dendritic matrix phase was not found to have any faults in them. It can be inferred from the aforementioned observations that the extent of preheat is largely responsible not only for changing the morphology of the phases but also for introducing faults.

SEM along with EDS, were used to determine the extent of Ti in the grains of the unpreheated specimen. It could be seen that the extent of enrichment of Ti in the NiAl is large, but not to an extent expected from the composition of the alloy. This is presumably due to the formation of the TiB₂ phase which consumes some amount of the Ti.

A comparison of the volume fraction of the pores in the unpreheated specimens with that in the preheated specimens showed that the preheated specimen had fewer number of pores. The pores were larger in size in the later as compared to the average pore size in the former.

IV. 3. 3 Fractography

Fracture morphology of the fractured surface of the unpreheated specimen showed mostly transgranular failure although features suggestive of intergranular failure could also be seen at many places (Figure IV. 3). This when compared with the fracture morphology of the unalloyed NiAl, differs considerably because of the fact that the unalloyed NiAl showed mostly

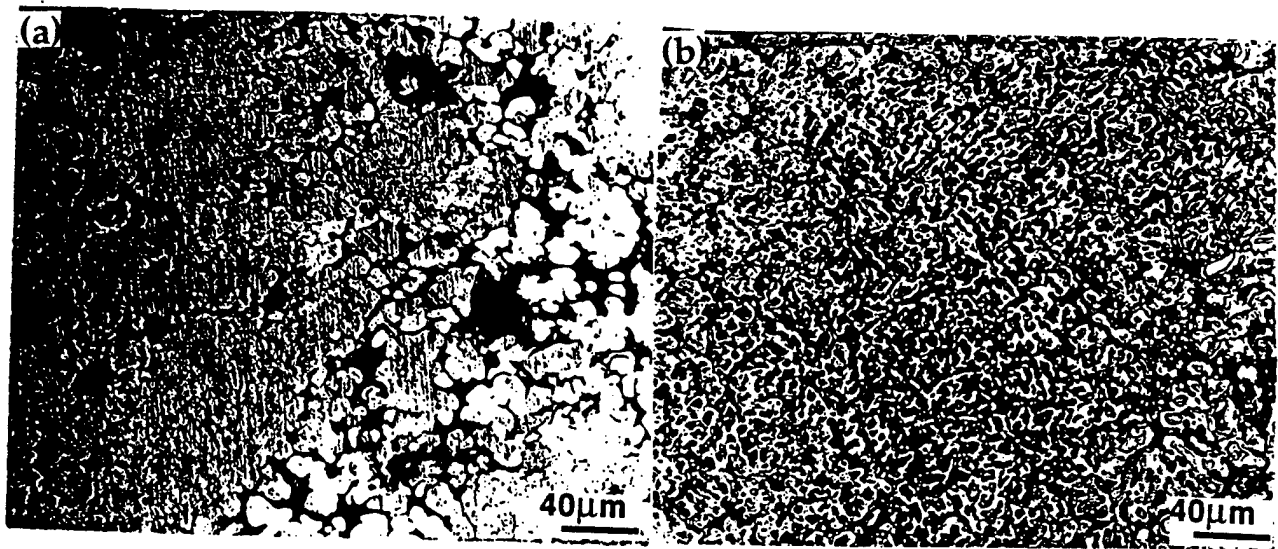


Fig. IV. 2 Microstructure of the NiAlTiB alloy after synthesis with preheat. (a) preheat temperature 473 K, (b) preheat temperature 623 K.

intergranular failure in tension. The addition of Ti and B to NiAl therefore has been seen to change the fracture mode from intergranular to transgranular. Similar observations has been made in the case of the addition of B to NiAl by George et al. [94]. George et al. [94] have concluded that grain boundaries in NiAl are intrinsically weak and B must be strengthening the grain boundaries leading to transgranular failure. However, it has been suggested by some workers that the effect of B was to suppress plastic deformation and eliminate the opportunity for intergranular fracture to initiate, rather than actually strengthen the boundaries. The observation of transgranular fracture in this study is in keeping with the fact that the fracture mode for NiAl alloys is predominantly transgranular whenever fracture occurs significantly before yielding.

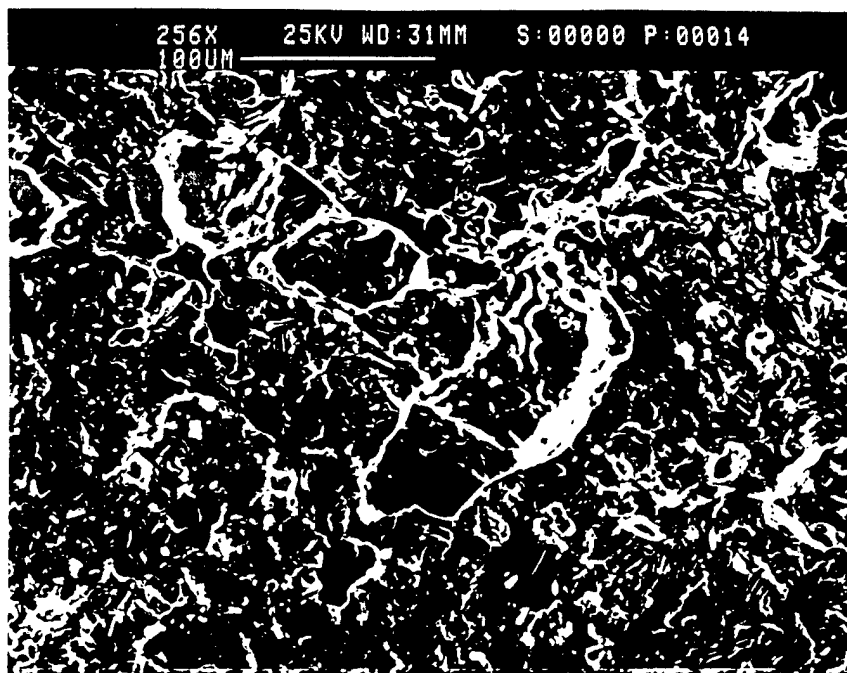


Fig. IV. 3 Fractograph showing the fractured surface of the NiAlTiB alloy synthesized without preheat.

IV. 4 Conclusions

The microstructure of the alloys studied in this work after micropyretic synthesis was quite different from that of binary NiAl because of the additional heat generated by the second reaction between the Ti and B. The extent of preheat has a profound influence on the microstructure and the nature of phases present in the micropyretically synthesized alloy. Ti and B participate in the formation of the TiB_2 phase and the solid solution strengthening of the matrix phase. These also lead to a change in the fracture morphology from intergranular to transgranular.

V. MICROPYRETIC SYNTHESIS OF NiAl WITH Ti AND Nb ADDITIONS

Several micropyretically synthesized complex intermetallics with B2 structure were studied. The alloys contained Ni, Al, Ti and Nb and were noted to possess high fracture toughness and oxidation resistance. In addition to the matrix B2 phase, each alloy was found to contain a variety of other phases. Some of these phases were found to be new. A correlation of the amount of the major alloying additions with the fracture toughness and oxidation resistance was established. Fracture toughness values greater than $12 \text{ M Pa m}^{1/2}$ were obtained with excellent oxidation resistance.

V. INTRODUCTION

Considerable amount of research has been done in the field of Ni aluminides and Ti aluminides. Besides poor ambient temperature ductility, the aluminides in the Ti and Ni systems suffer from lack of very high temperature creep resistance and can not meet the requirements made by advanced propulsion systems. As a result, it has been necessary to study other intermetallic compounds which have higher melting points and therefore potentially improved mechanical properties. Nb_3Al is one such system and hence it is being studied in considerable detail [95]. Nb_3Al exhibits the A15 crystal structure and although it has high temperature strength, it is very brittle at ambient temperatures [96]. The brittleness of the alloy stems from the fact that it has a limited number of operating slip systems [96]. Studies have shown that by alloying it is possible to induce a crystal structure transition to a structure which will permit the operation of more number of slip systems rendering the alloy ductile. In some of the earlier studies in this alloy involving melt spun ribbons, higher dislocation density has been

observed after the structure changed to the B2 form [97]. It was therefore realized that the B2 structure in this alloy will be ductile. In order to stabilize the B2 structure in this alloy, which otherwise has a A15 structure, alloying additions were attempted and it was found that Ti is a B2 stabilizer. It is well known that Ti bearing B2 structures are quite ductile. With this point in view, ternary Nb-Al-Ti alloys have been developed and these have been found to show considerable ductility at ambient temperatures [97]. The development of these Nb-Al-Ti alloys has created quite a sensation because these have all the advantages of intermetallic compounds, but do not suffer from brittleness at ambient temperatures [98]. Because of this very attractive combination of properties, which otherwise is quite difficult to achieve, these alloys have acquired considerable significance and are being investigated very vigorously. It is interesting to note that where as NiAl has a B2 structure and is extremely brittle at room temperature, the alloy Nb₄₅Al₁₅Ti₄₀ with a similar structure is ductile. The alloys of the Nb₄₅Al₁₅Ti₄₀ type are likely to have a poor oxidation resistance due to the high amount of Nb. It has been the endeavor of this study to find suitable mixes of elements in these two alloys (namely NiAl and Nb₄₅Al₁₅Ti₄₀) with the view to obtaining an alloy which can be synthesized micropyretically and will have good fracture toughness and oxidation resistance.

It was observed that although the addition of the Nb and Ti to NiAl lead to a decrease in the combustibility, the alloy mixtures remained quite combustible even after having 60% of the ingredients of Nb₄₅Al₁₅Ti₄₀ alloy by weight. On increasing the proportion of the Nb₄₅Al₁₅Ti₄₀ alloy to 80%, combustion could be carried out only by preheating. In the Nb₄₅Al₁₅Ti₄₀

alloy, the combustion could not be carried out well even after considerable preheating.

X-ray diffraction showed that most of the alloys in the series made, have a major volume fraction of a phase with B2 structure. A variety of phases were found to coexist with this B2 phase in the microstructure. The amount of the B2 phase was found to be highest on the extremes of the compositions i.e. unalloyed NiAl and Nb₄₅Al₁₅Ti₄₀ and decreased in the intermediate composition ranges.

In the Nb₄₅Al₁₅Ti₄₀, the combustion reaction was found to occur in two stages. The first stage was found to lead to the formation of two intermetallic phases, whereas the second stage led to the formation of the B2 phase. The mechanical properties like hardness and fracture toughness, have been determined in the series of alloys. It could be seen that although the alloys having higher amounts of Nb were better from the view point of fracture toughness, the alloys richer in nickel had superior oxidation resistance.

V. 2 Experimental

High purity powders (purity and size indicated in Table V. I were weighed accurately and mixed in a Spex model 8000 ball mill for twenty minutes without the addition of any liquid medium. Subsequently, the mixed powders were pressed into rectangular bar specimens in a double acting press at a pressure of 160 MPa. The pressed compacts were combusted in an inert atmosphere by igniting from one end. The chamber used for combustion has been discussed in chapter III. It comprised a quartz tube which could be evacuated and then filled with Ar to maintain a steady flow over the specimen. The specimen was placed on an alumina boat. The

temperature of the specimen could be monitored by placing thermocouples at different parts of the specimen. Combustion was initiated by heating one end of the specimen by induction heating. In this study, synthesis was carried in air as well as in an inert atmosphere of flowing argon. It was observed that argon substantially reduces the oxidation of the specimen during synthesis.

V. I Purity and Particle size of the Powders Used

| Element | Purity | Powder size |
|---------|--------|-----------------|
| Ni | 99.7 | 3 μm |
| Al | 99.5 | -325 mesh |
| Nb | 99.7 | -325 mesh |
| Ti | 99.0 | -325 mesh |

The dimensions of the specimen were found to change after synthesis. The combusted specimens were made uniform in dimension by grinding the surface. A notch was introduced in the specimen by means of a diamond saw. The fracture toughness was measured by the four point bend technique [14]. A Cambridge SEM equipped with a Link detector was used for the examination of the fracture surface and the microstructure. X-ray diffraction was carried out in a Philips diffractometer (model: X'pert) employing a Cu tube operating at 40 kV and 55 mA. The porosity of the combusted samples was measured using image analysis. Porosity values were used for calculating the density of the combusted material.

Specimens for TEM observation were made by two different techniques. The specimens synthesized with preheat were found to be more dense and thin foils for TEM examination could be made in these using the twin jet electropolishing technique using an electrolyte containing 10% perchloric acid and 90% methanol. The electrolyte temperature was kept below 240 K. In the case of specimens synthesized without preheat, due to the relatively higher

amount of porosity, thin foils could not be made by the twin jet electropolishing technique. Specimens were, therefore, made by dimple grinding followed by ion milling in a Gatan ion mill. Thin foils were examined in a Philips CM 20 electron microscope equipped with an EDAX microanalysis system.

V. 3 Results and Discussion

V. 3. 1 Combustibility of the Alloys

NiAl is known to undergo combustion with considerable ease even without any preheating of the powder compact. This aspect is well documented in chapter III of this report. On the other hand, the alloy Nb₄₅Al₁₅Ti₄₀ was found to combust only after a considerable amount of preheating. The addition of diluents in very small amounts has the effect of increasing the velocity of the combustion front. This effect has been observed in several studies and discussed in detail in the previous two chapters. The effect of the addition of the diluents on the rate of the combustion process has been examined in some of the studies and it has been shown that addition of diluents in very small quantities can significantly influence the rate of the combustion process. However, when the amount of the diluents is increased considerably, the rate of the reaction has been found to reduce substantially. The reasons for this kind of behavior has been explained in the earlier chapters. The combustion velocities and the peak temperatures for the different reactions are shown in the Table V. 2. The reaction velocities have been found to reduce with increasing amounts of Nb and Ti added to NiAl. There is also a reduction in the value of the peak temperature. A correlation between the peak temperature and the microstructure has been discussed later. In the alloys containing more of Nb and Ti than Ni and Al, combustion

was found to occur only by preheating. In the alloys completely free of Ni, combustion occurred in an unstable manner only after considerable amount of preheating.

V. 2 Combustion Temperature and Propagation velocity

| Composition | Combustion temperature (K) | Propagation Velocity (m/s) |
|---|----------------------------|----------------------------|
| Ni ₅₀ Al ₅₀ | 1905 | .20 |
| Ni ₅₀ Al _{49.25} Nb _{.5} Ti _{.25} | 1915 | .17 |
| Ni _{49.25} Al _{49.5} Nb _{.75} Ti _{.5} | 1920 | .15 |
| Ni _{43.5} Al _{44.5} Nb _{6.5} Ti _{5.5} | 1910 | .12 |
| Ni _{36.25} Al _{37.75} Nb _{13.75} Ti _{12.25} | 1890 | .10 |
| Ni _{25.5} Al ₃₂ Nb _{22.5} Ti ₂₀ | 1870 | .07 |
| Ni _{13.75} Al _{24.5} Nb ₃₃ Ti _{29.25} | 1853 | .05 |
| Nb ₄₅ Al ₁₅ Ti ₄₀ | 1840 | .04 |

V. 3. 2 Phases and Microstructures

V. 3. 2. 1 X-ray Diffraction Results

Before analyzing the nature of the phases actually present in the specimen, it is worth exploring the nature of the expected phases in the alloys examined in this study. The solubility of Ti in NiAl is 10 at% and that of Nb is 5 at%. The other binary, ternary and quaternary phases expected are the following: Nb₂Ni, NbNi, Al_{4.6}Ni_{23.4}Nb₂₄, AlNbNi, AlNbNi₂, Al_{.5}Nb_{.5}Ni₃ besides a large number of phases in the NiTi system [99, 100]. It has been apprehended that addition of Nb to NiAl is likely to lead to the formation of

the sigma phase in the alloys and the formation of this phase can severely impair the properties of the alloys [101]. The X-ray diffraction results from the alloys are shown Table V. III. The alloys having a very small amount of Ti and Nb have the B2 phase as the major phase. The phase making its appearance seems to be the AlNbNi phase which has a hexagonal structure [100]. The lattice parameter of the B2 phase has been found to increase systematically as Ti and Nb additions have been done. In the alloys containing more of Ti and Nb, the nature of the phases was found to undergo a change. The B2 phase which is expected in the Nb₄₅Al₁₅Ti₄₀ alloy started to appear. The amount of this B2 phase was found to increase in the alloys as more of Ti and Nb were added. Finally the last alloy almost completely comprised of the B2 phase having a lattice parameter of $a = .325$ nm.

V. III Table showing X-ray diffraction results

| Composition | Nature of Phases |
|---|------------------------------------|
| Ni ₅₀ Al ₅₀ | B2 |
| Ni ₅₀ Al _{49.25} Nb _{.5} Ti _{.25} | B2 and AlNbNi |
| Ni _{49.25} Al _{49.5} Nb _{.75} Ti _{.5} | B2 and AlNbNi |
| Ni _{43.5} Al _{44.5} Nb _{6.5} Ti _{5.5} | B2 and AlNbNi |
| Ni _{36.25} Al _{37.75} Nb _{13.75} Ti _{12.25} | AlNbNi and very small amount of B2 |
| Ni _{25.5} Al ₃₂ Nb _{22.5} Ti ₂₀ | AlNbNi and small amount of B2 |
| Ni _{13.75} Al _{24.5} Nb ₃₃ Ti _{29.25} | AlNbNi and B2 Nb |
| Nb ₄₅ Al ₁₅ Ti ₄₀ | B2 |

V. 3. 2. 2 Microstructures

The microstructures of the NiAl alloy synthesized without any preheating is known to comprise of equiaxed grains. This microstructure has been examined with optical microscope and TEM and the results have been discussed in considerable detail in chapter III. The addition of very small amounts of Nb and Ti was not found to create any change in the optical microstructure (Figure V. 1). Equiaxed grains of NiAl phase continued to be visible in the microstructure as the matrix phase. The presence of no other phase could be seen, although X-ray diffraction showed that a second phase was present. When the amount of Nb and Ti was increased, the presence of a second phase could be seen at the grain boundaries (Figure V.2). X-ray diffraction as well as EDS point count analysis, showed that this phase is the AlNbNi phase. In the specimens having higher amount of the elements, Nb and Ti, the thickness of the grain boundary phase was quite large (Figure V. 3(a)). EDS point count analysis (Figure V.3. (b)) indicated that this is the AlNbNi phase. In alloys having higher amounts of the elements Nb and Ti, complex microstructures could be seen. Two of these microstructures are shown in Figures V.3 (c) and (d). In the alloys having Nb and Ti as major alloying additions, the B2 phase could be seen as the matrix phase. In the last alloy, the B2 phase was the only phase in the microstructure. The mechanism of formation of the single phase B2 microstructure in this alloy from the alloying additions is discussed in Chapter VI of this report. The microstructure of this alloy, as obtained by micropyretic synthesis was compared with that obtained from the conventional casting route and considerable similarity between the two microstructures could be seen. An

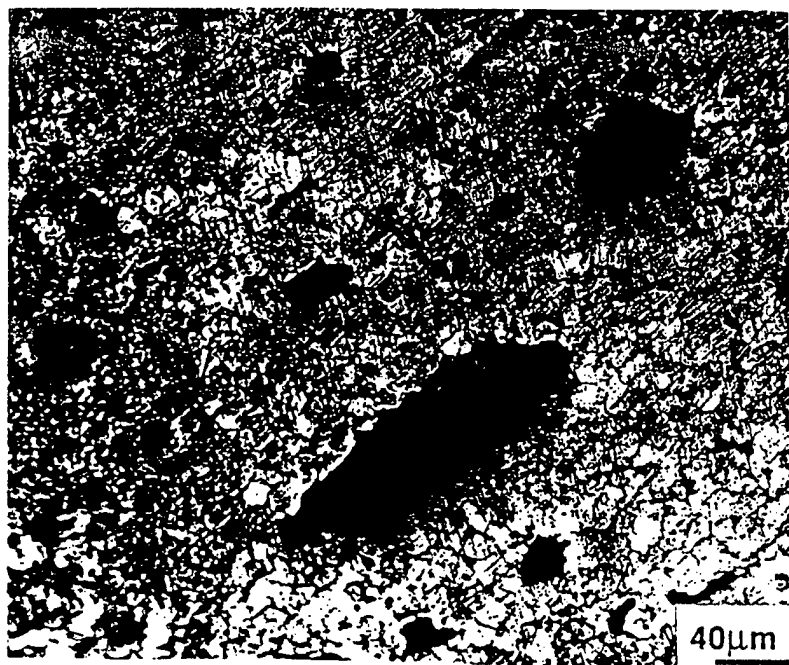


Figure V. 1 Equiaxed grains of the NiAl phase in the microstructure of NiAl.

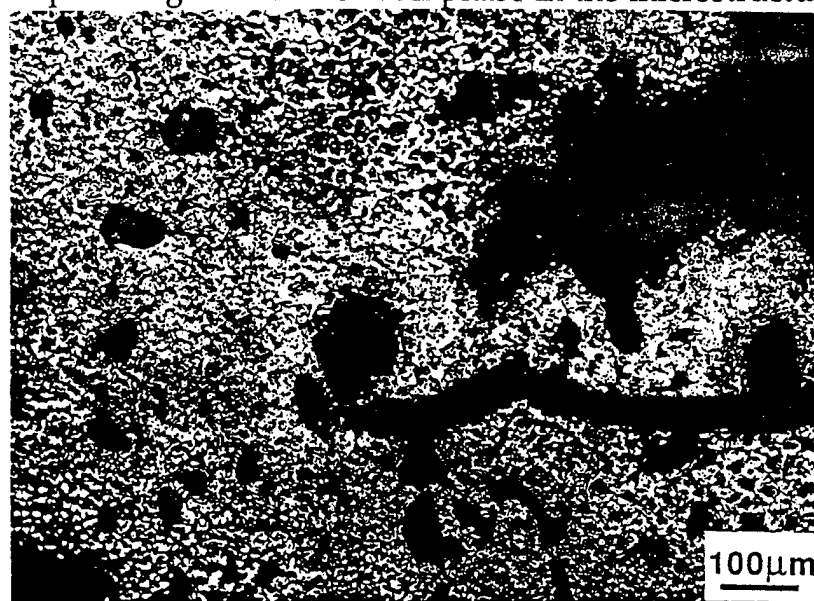


Figure V.2 Equiaxed grains of NiAl phase in the microstructure of alloy 3.
The presence of a second phase can be seen at the grain boundaries.

electron diffraction pattern from the micropyrethically synthesized microstructure is shown in Figure V. 3. (e).

V. 3. 3 Fracture Toughness

The fracture toughness of the alloys are shown in Table V. 4. It can be seen that the fracture toughness increases initially with the addition of the alloying elements Nb and Ti. The highest value of fracture toughness observed is 12, which is quite good when compared to that of the binary NiAl. It may be noted that high fracture toughness values have also been also observed by Petzow et al. [102] in their studies involving NiAl with Nb and Ti additions.

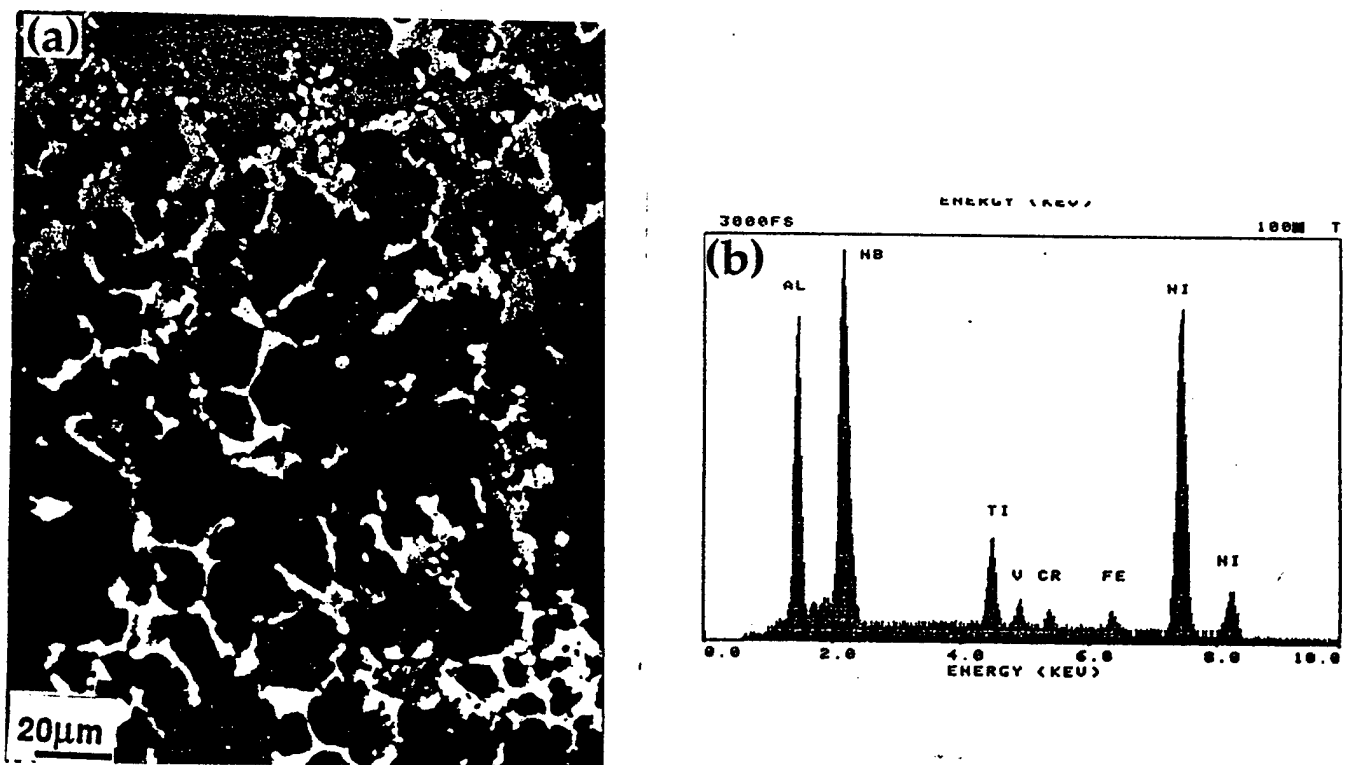


Fig. V. 3 (a) Micrograph showing thick grain boundary phase in alloy 4. (b) EDS point count analysis indicated that this is the NiAlNb phase.

Although the micropyrethically synthesized alloys have pores, their fairly good fracture toughness value is almost comparable to that obtained by

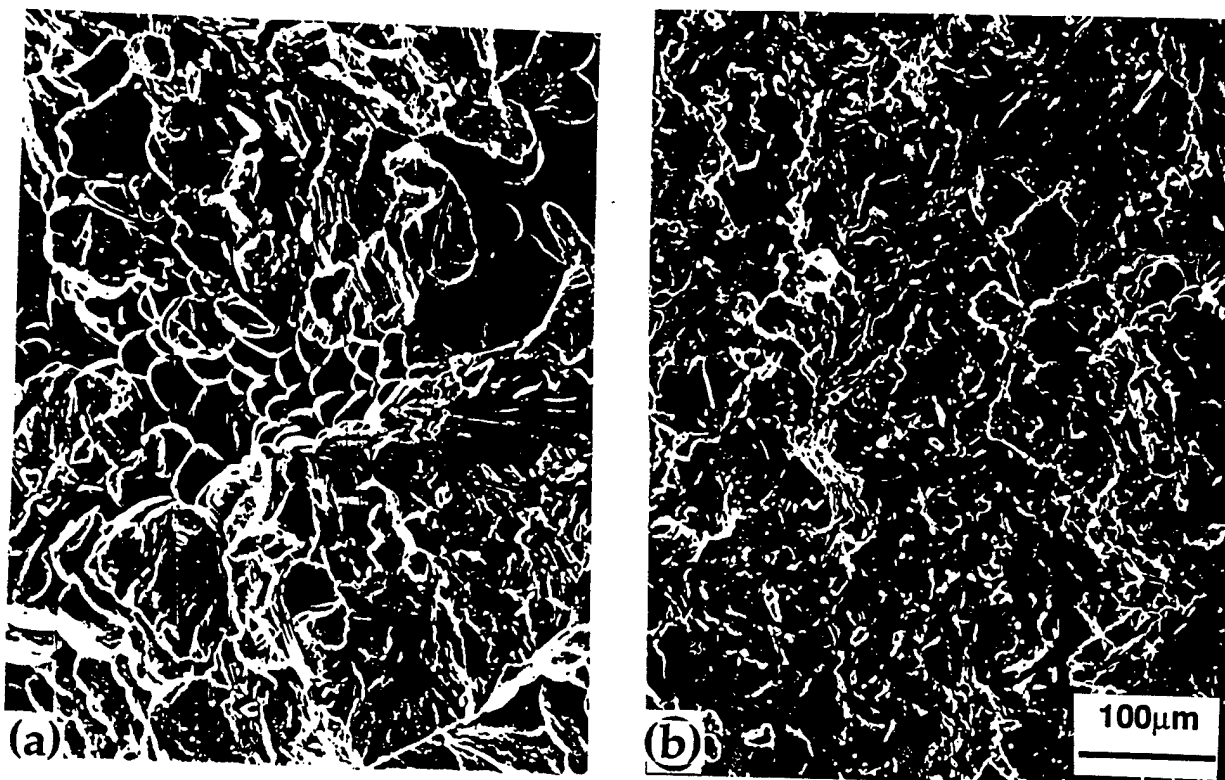
Petzow et al. [102] in their studies. The reasons for the observation of good fracture toughness, despite the presence of pores has been discussed in considerable detail in Chapter III. The enhancement of the fracture toughness of the alloys on alloying is presumably due to the increase in the ductility of the alloys. This contention is based on the observations made in the case of Fe, Cr and V additions to NiAl in Chapter III. In NiAl, the increase in ductility has been found to be associated with an increase of the fracture toughness. On increase of the Nb and Ti content further, the fracture toughness was found to fall substantially. This is not surprising when the microstructure of the alloy is considered. In the alloys containing higher amounts of the Nb and Ti, the microstructure shows a near contiguous layer of a second phase at the grain boundaries. The presence of a second phase in this nature will lead to intergranular failure and also a reduction in the fracture energy. The examination of the fracture surface confirmed the fact that the fracture mode changed from the transgranular to the intergranular form of fracture. This aspect has been discussed in the next section of this chapter.

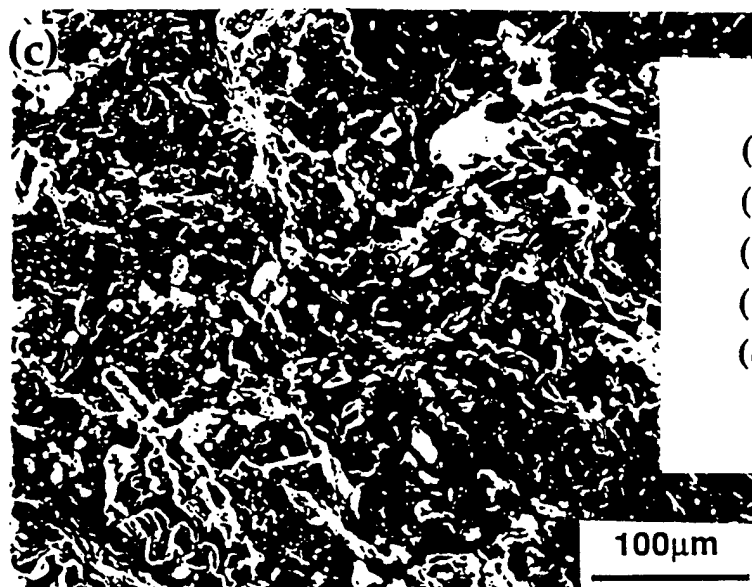
Table V. 4 Hardness and Fracture Toughness of the Alloys

| Composition | Hardness (VPN) | Fracture Toughness (M Pa m ^{1/2}) |
|---|-------------------|---|
| Ni ₅₀ Al ₅₀ | 310 | 6.0 |
| Ni ₅₀ Al _{49.25} Nb _{.5} Ti _{.25} | 300 | 8.0 |
| Ni _{49.25} Al _{49.5} Nb _{.75} Ti _{.5} | 305 | 12.5 |
| Ni _{43.5} Al _{44.5} Nb _{6.5} Ti _{5.5} | 350 | 5.0 |
| Ni _{36.25} Al _{37.75} Nb _{13.75} Ti _{12.25} | 336 | 6.8 |

V. 3. 4 Fracture Behavior

The fracture behavior of the alloys was examined in considerable detail. The fracture morphology of the alloys was found to change substantially with the microstructure and hence the alloying additions. Unalloyed NiAl is known to show transgranular failure during fracture toughness testing. In this study it was observed that the addition of a small amount of Ti and Nb did not change the fracture morphology to any observable extent. The fracture morphology continued to show a transgranular brittle failure (Figure V. 4). With the addition of more of Ti and Nb, it was observed that the specimens had a pronounced tendency to show intergranular failure (Figure V. 4). This is not surprising in view of the fact that in the microstructure, the grain boundary phase has started to form. The tendency to undergo intergranular failure continued to increase as the amount of the grain boundary phase continued to increase. Considerable change in the appearance of the fracture





- (a) Ni₅₀Al_{49.25}Nb_{0.5}Ti_{0.25}
- (b) Ni_{49.25}Al_{49.5}Nb_{0.75}Ti_{0.5}
- (c) Ni_{43.5}Al_{44.5}Nb_{6.5}Ti_{5.5}
- (d) Ni_{13.75}Al_{24.5}Nb₃₃Ti_{29.25}
- (e) Nb₄₅Al₁₅Ti₄₀

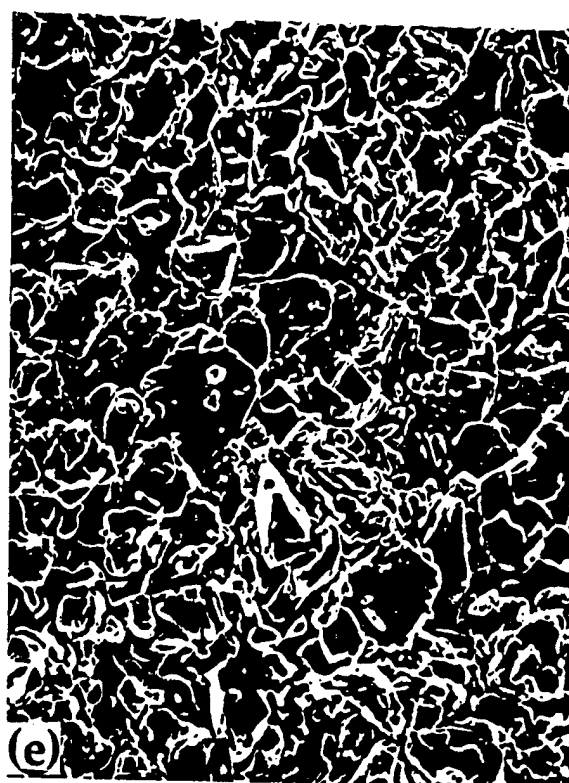
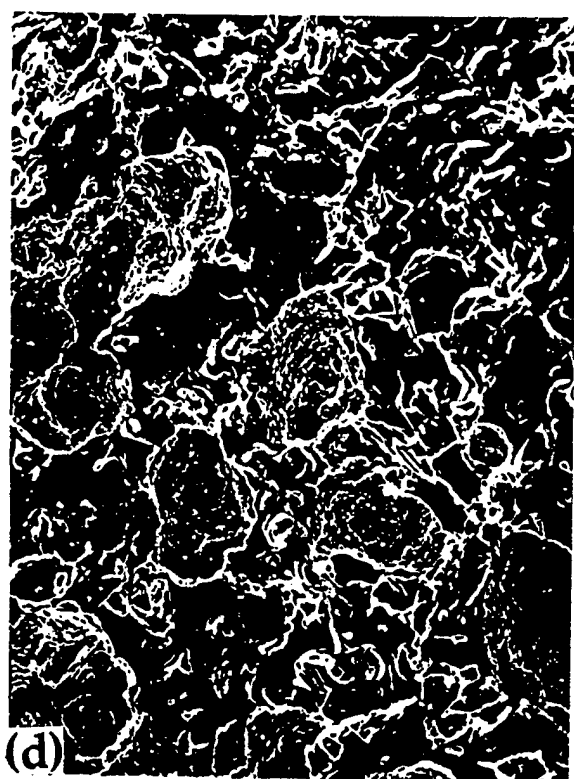


Fig. V. 4 Factograph showing the fracture surface of the different alloys.

surface could be seen once the ductile B2 phase made its appearance. Once the volume fraction of the ductile B2 phase increased the fracture morphology transformed to the ductile mode. The fracture surface of the alloy is shown in figure V. 4. It can be seen that the fracture surface has a dimple like appearance in most of the regions.

V. 3. 5 Oxidation Behavior of the Alloys

Nb based alloys are known to undergo rapid oxidation [103]. One of the objectives of this study has been to examine the effect of the alloying additions on the oxidation resistance of the alloys. The oxidation resistance of some of the alloys were measured by the weight gain technique. For the sake of comparison, only the binary NiAl and the Ni free B2 alloy and two other compositions with NiAl as the base and Nb and Ti as alloying additions were chosen. The oxidation rates of the different alloys at a temperature of 1373 K is shown in Figure V. 5. It can be seen that the Ni free B2 alloy has the highest oxidation rate, whereas the binary NiAl has the lowest oxidation rate. The oxidation rate of the NiAl alloy falls as Nb and Ti is added. Nb based alloys are known to undergo rapid oxidation.

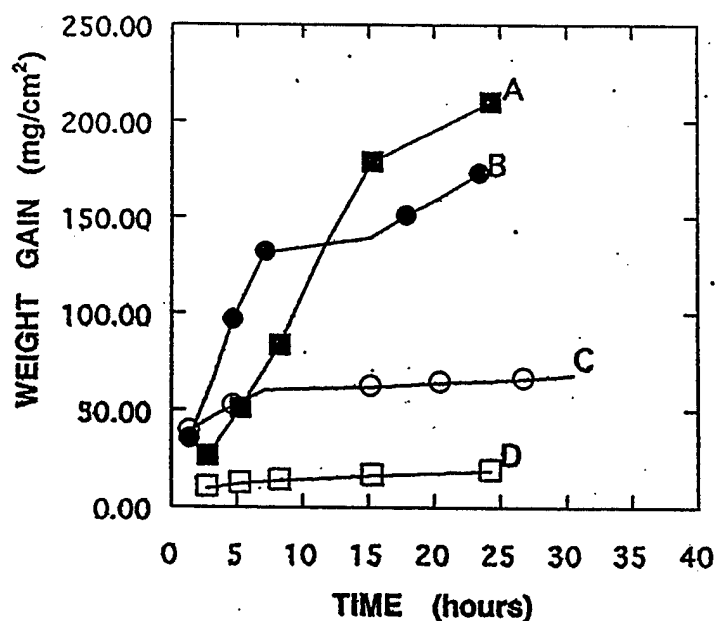


Fig. V. 5 Plots showing the rate of oxidation of different alloys at a temperature of 1373 K. A - Nb₄₅Al₁₅Ti₄₀, B - Ni_{13.75}Al_{24.5}Nb₃₃Ti_{29.25}, C - Ni_{43.5}Al_{44.5}Nb_{6.5}Ti_{5.5} and D - Ni₅₀Al₅₀.

V. 4 Conclusions

Based on the observations made in this study, the following conclusions can be drawn. The combustibility of the alloys was found to decrease with the addition of Nb and Ti. The microstructure comprises B2 NiAl along with Nb and Ti bearing phases in alloys having smaller amounts of Nb and Ti. The fracture toughness of the alloys increased with the addition of very small amounts of Nb and Ti. The oxidation resistance of the alloys deteriorated with increase in Nb and Ti content in the alloys.

VI. MECHANISM OF MICROPYRETIC SYNTHESIS IN NiAl AND Nb₄₅Al₁₅Ti₄₀

The mechanism of synthesis in micropyretic synthesis of NiAl and Nb₄₅Al₁₅Ti₄₀ has been established by carrying out microstructural examination of partially combusted specimens. In the former alloy a partially combusted specimen has been obtained by stopping the combustion front by squeezing the specimen between two copper plates. In the latter alloy, which combusts only after considerable preheating of the specimen, a partially combusted specimen has been obtained by withdrawing preheat after some amount of combustion has occurred. Extensive microstructural examination has been carried out around the stopped combustion front in order to establish the sequence of synthesis. In the case of NiAl, the formation of the product phase has been found to be preceded by the formation of an intermediate complex. In the case of Nb₄₅Al₁₅Ti₄₀, it has been observed that the single phase microstructure forms by a two step process involving a reaction between two aluminide phases.

VI. 1 Introduction

In order to exploit the use of micropyretic synthesis to synthesize advanced materials, basic mechanisms must be identified. Crucial questions such as role of the liquid formation as a trigger of the reaction, the effect of the transient phases on the reaction kinetics, pore formation and restructuring of the product phase can be answered only after a systematic study of the mechanism of synthesis [104]. This can best be done by following the changes occurring in the various zones relative to the location of the reaction front. A method to study the mechanisms of combustion synthesis

consists of rapidly quenching the reaction front while it is progressing through the reactant mixture. A layer by layer analysis of the sample is then performed in order to characterize chemical reactions and structural transformations giving rise to the final product [104]. Various methods are available for the quenching of the reaction front. In some of the early studies the reacting sample was dropped into liquid argon. However, owing to the formation of a gaseous layer around the burning sample, only relatively low cooling rates could be achieved. Higher cooling rates are possible when heat losses are induced by conduction through a cold wall [92, 105]. This can be done by squeezing the specimen between two copper plates, a technique that has been used in this study.

VI. 2 Experimental

High purity powders (purity and size indicated in Table VI. I) were weighed accurately and mixed in a Spex model 8000 ball mill for twenty minutes without any addition of a liquid medium. Subsequently, the mixed powders were pressed into rectangular bar specimens in a double acting press at a pressure of ~ 160 MPa. The pressed compacts were synthesized in an inert atmosphere by igniting with induction heating. A Cambridge SEM equipped with a Princeton Gamma-Tech detector was used for the examination of the microstructure and for carrying out microanalysis by EDS. Specimens for TEM observation were made by two different techniques. The specimens made by melting and solidification were found to be dense and thin foils for TEM examination could be made for these using the twin jet electropolishing technique using an electrolyte containing 10% sulfuric acid and 90% methanol. The electrolyte temperature was kept below 240 K. In the case of specimens synthesized by micropyretic synthesis, on account of the presence

of porosity, thin foils could not be made by the twin jet electropolishing technique. Specimens were therefore made by dimple grinding followed by ion milling in a Gatan ion mill. The foils were examined in a Philips CM 20 microscope operating at 200 kV.

Table. VI. 1 Purity and Particle Size of the Powders Used

| Element | Purity | Powder size |
|---------|--------|-----------------------------|
| Ni | 99.7 | 3 μm , -100 mesh |
| Al | 99.5 | -325 mesh |
| Cr | 99.0 | -325 mesh |
| Fe | 99.9 | 10 μm |
| Nb | 99.7 | -325 mesh |
| Ti | 99.0 | -325 mesh |
| V | 99.5 | -325 mesh |

VI. 3 Results and Discussion

VI. 3. 1 Mechanism of Synthesis in NiAl

In order to study the mechanism of microstructure formation during the synthesis process in the specimens containing the diluents it was necessary to freeze the reaction front. When an attempt was made to freeze the front in specimens made with 3 μm Ni powder by squeezing the sample between two copper plates, it was observed that the front traverses the entire length of the specimen without freezing. It was then decided to use a larger Ni particle size. Without the copper plates, the front did not stop even when larger Ni powders were used because of the effect of the diluents. However, the front could be made to stop with the use of the copper plates as shown in figure 9. In order to examine the sequence of formation of NiAl from the powder particles, a detailed microstructural characterization was carried out of the different regions on a specimen where the reaction front has been stopped by squeezing the specimen in between two copper plates. Quenching the reaction

front during its passage through the sample is a very powerful tool for studying the mechanism and different stages of synthesis. This approach has been used by Lebrat et al. [104] to study the formation of Ni_3Al from its alloying ingredients. Though an attempt has been made to examine the sequence of formation of NiAl from powders by Li et al. [12], this study differs from the earlier ones in two important respects namely (1) the front has been stopped by the use of copper plates. By changing the process conditions like green density and preheating temperature though the extent of reaction can be altered and some intermediate compounds existing during the synthesis can be isolated, this approach fails to provide a detailed account of the mechanism of formation of the final product [104], and more importantly 2. The mechanism of formation is being studied after adding the diluents like Cr, Fe and V. This study attempts to identify the sequence of formation of the different phases on way to the final formation of the NiAl phase. The earlier studies have not elaborated the entire sequence [12, 30] and mentioned the formation of an intermediate complex only. Figure VI. 2 shows temperature profiles at three different locations along the length of the specimen. The first thermocouple is located just outside the copper block. At this point the temperature rises to a value of 1850 K and drops down quickly. The other two thermocouple are located inside the copper block. Inside the copper block, the front stopped after propagating for some distance and the peak temperature decreased in the successive locations. Microstructural examination was carried out at different locations starting from the ignited end. Figure VI. 3 shows the microstructure of the end which has been ignited by the torch. This region has mostly dendritic microstructure. The formation of the dendritic microstructure is because of the fact that this end of the sample was preheated substantially before ignition by exposure to the torch and it has melted

substantially as a result of the preheating. As the combustion front progressed forward, the morphology of the grains changed substantially and gradually the dendritic grains changed to equiaxed grains .

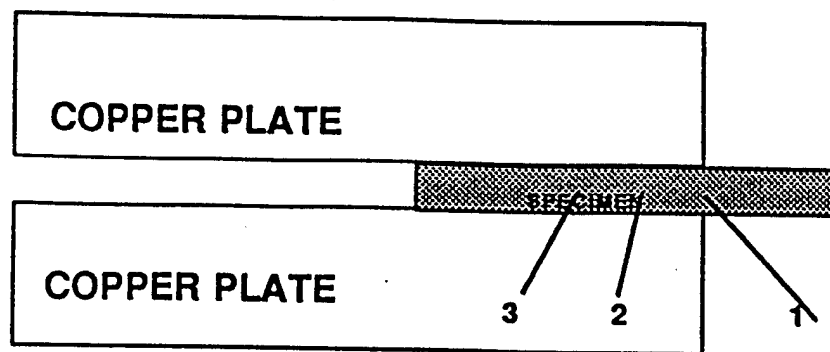


Fig. VI. 1 Schematic diagram showing the use of the copper plates for stopping the reaction front. The position of the thermocouples are indicated by different numbers.

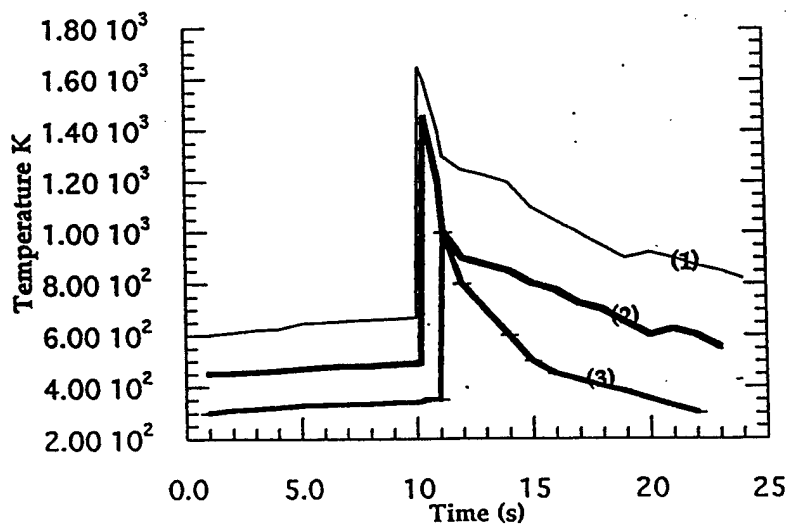


Fig. VI. 2 Temperature profiles generated across the length of the sample. The numbered position indicates the position of the thermocouples.

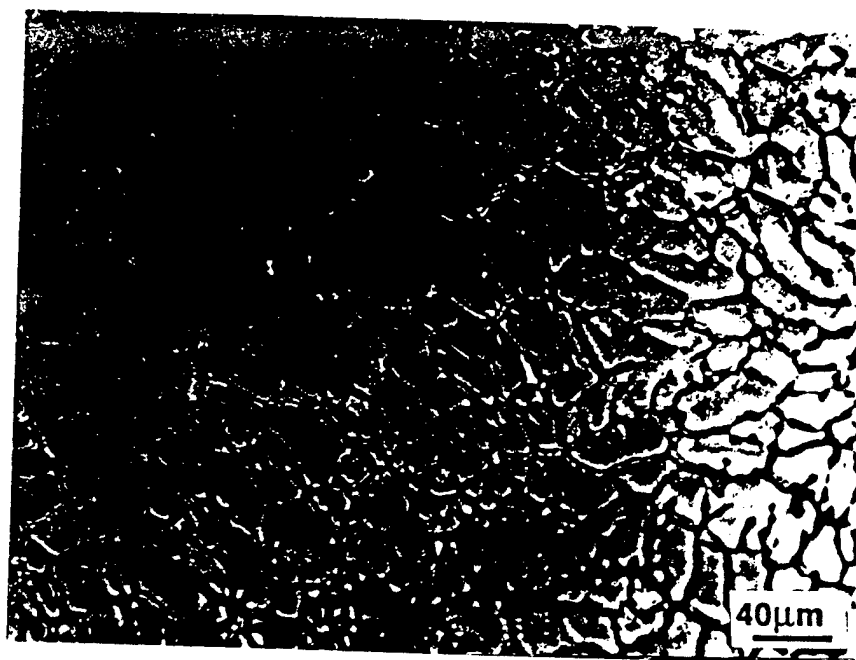


Fig. VI. 3 Optical microstructure of the end of the sample at which ignition has been done.

In order to examine the nature of the reaction occurring at the front, the microstructure of the specimen was examined away from the front on the powder side, at the front and finally on the intermetallic side of the front. Figure VI. 4(a) shows the frozen combustion front with the arrow indicating the approximate position of the front. Depending upon the extent of reaction, the specimen could be divided into three distinct regions- **unreacted region**, **partially reacted region** and **fully reacted region**. A description of the microstructure of these three regions follows:

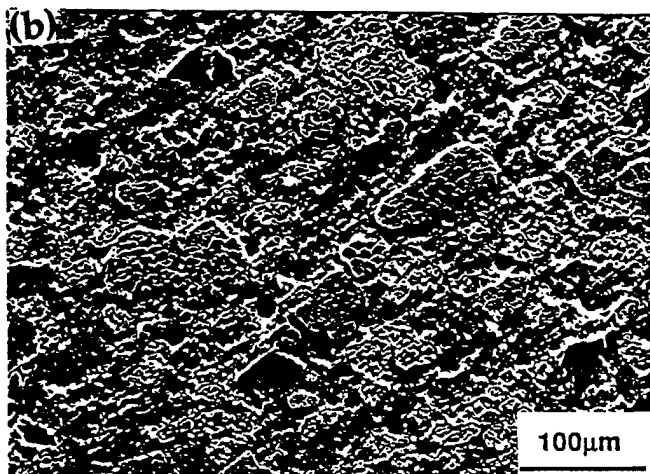
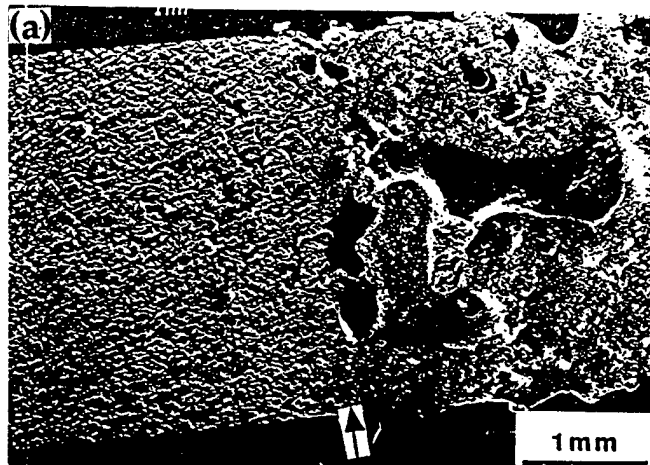
Unreacted region: Figure VI. 4(b) shows the powder side of the front at a distance at which the microstructure is not effected by the heat generated at the front. The Al and the Ni powders can readily be distinguished by comparing the secondary electron image with x-ray mapping. It may be noted

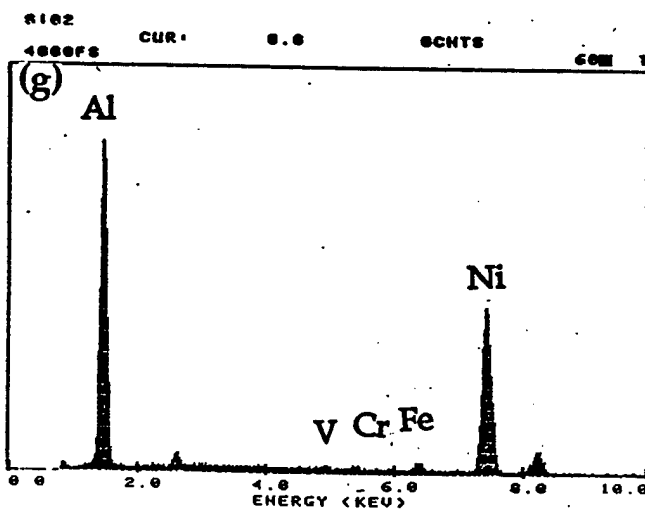
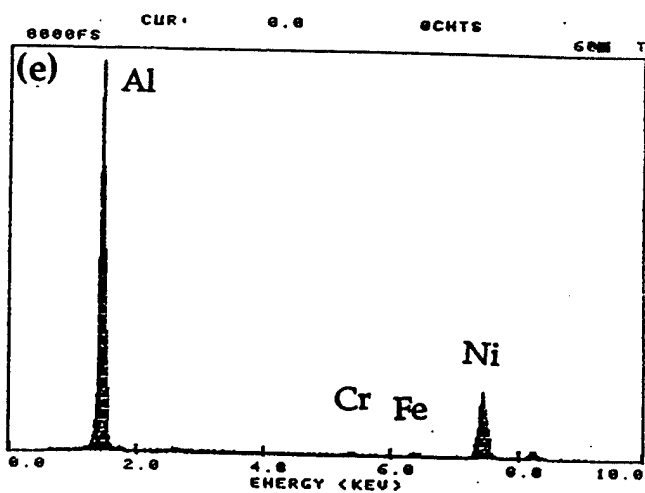
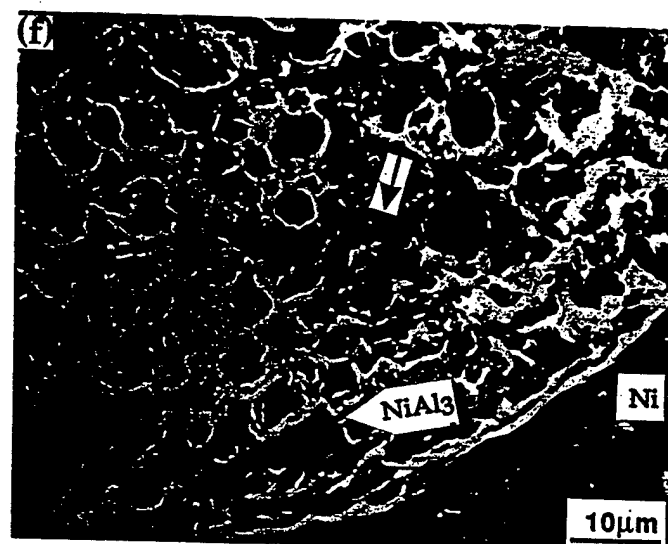
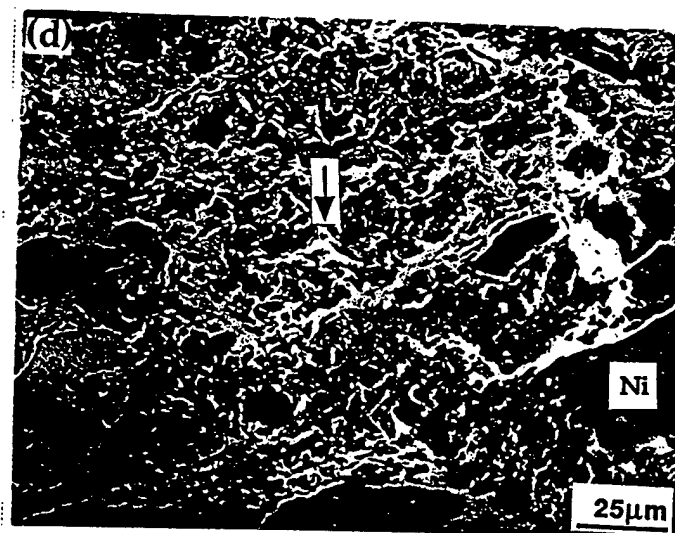
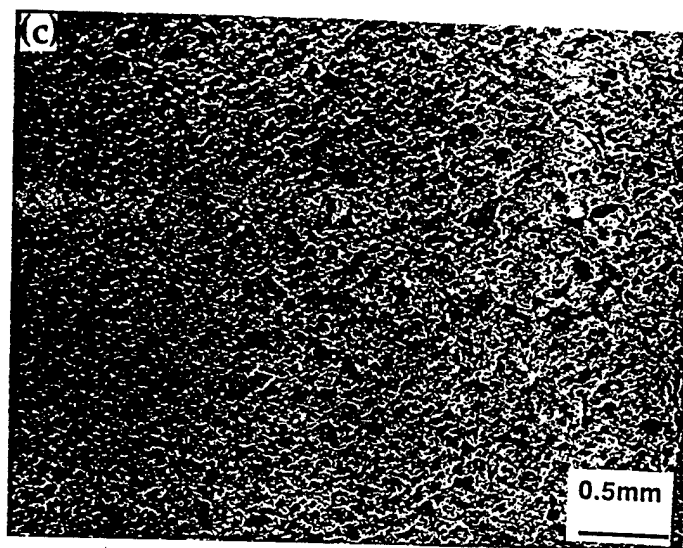
that the Ni powder size is about three times larger than Al powder. The Ni powder particles are all surrounded by Al particles and instances of a Ni particle touching another Ni particle were very few. The distribution of the other alloying elements could not be ascertained because of their small concentration. However, it can be speculated that these behind in contact with each other will be low and the probability of these either touching a Ni or a Al particle will be high. Al is the lowest melting ingredient and therefore is likely to melt first and surround the particles of Ni, Fe, Cr and V during the initial stages of synthesis. The occurrence of a reaction between molten Al and other elements will depend on the enthalpy of reaction, the adiabatic temperature and the temperature of ignition of the reactions. The Ni-Al reaction is known to have high adiabatic temperature, enthalpy of formation and low ignition temperature [10] and is thus the most favorable combustion reaction is between Ni and Al. It can therefore be expected that the reaction between Ni and Al starts first. The other alloying dissolve in the intermediate products of reaction between Ni and Al. The complete and homogeneous dissolution of the alloying elements is evident from microstructural studies carried out in the TEM.

Partially reacted region: The stopped combustion front is the region where a single phase microstructure has formed (indicated by arrow in figure VI. 4(a)). To the left of it is a region where Al has melted and reacted with the other elements either fully or partially. The melting of Al occurs quite some distance ahead of the front. This region extends from the place where a complete single phase microstructure can be seen to the point where the Al has just melted without undergoing any substantial reaction. Figure VI. 4(c)

gives a better view of the end of the partially reacted region. The beginning of the region can be seen in figure VI. 4(a). Figure VI. 4(d) shows the microstructure towards the end of the partially reacted region. This is very close to the location of the third thermocouple. It can be seen that the Ni particles are coexisting along with Al rich region which contains Ni as well as the other alloying elements in solid solution. The reaction of molten Al with Ni and the other elements leads to the formation of Al rich phases. The EDS point count analysis from a region marked on the micrograph is shown in the figure VI. 4(e). The approximate stoichiometry of the region is as follows: 91.33 at% Al, 0.01 at% V, 0.23 at% Cr, 0.4 at% Fe and 8.03 at% Ni. This stoichiometry did not correspond to that of any of the known phases in the Ni-Al phase diagram. The Al rich phases formed are quickly consumed, as we move towards the front, to yield phases which contain more Ni. Figure VI. 4(f) shows the microstructure of a region closer to the stopped reaction front. Unconsumed Ni particles along with Al rich phase mixture could be seen. The phase mixture was found to comprise NiAl_3 and an Al rich phase having the other alloying elements (EDS profile in figure VI. 4(g)). As the temperature increases the molten Al reacts more with Ni and the Al rich phases to yield phases containing higher amounts of Ni such as Ni_2Al_3 . The identity of all the intermediate phases forming should ideally be dictated by the tie line drawn on the equilibrium diagram at that temperature. However, since the conditions are far from equilibrium, the kinetic factors will have a very important role and only those phases will form which are kinetically favored. Figure VI. 4(h) is from a region very close to the front and the location of the second thermocouple. The dissolution of the Ni particles becomes clear once a comparison is made between figures VI. 4(h) and figure VI. 4(a) which suggests the shrinkage of the cores of Ni in the former. It may

be noted that the observation of different amount of reaction for each Ni particle does not only depend on where the particle is located relative to the front but is also related to its size. The Ni particle size is quite large as compared to that of the other elements and in the larger Ni particles the reaction is not able to get to completion because the reaction has been stopped. Such a large particle at the front is shown in figure VI. 4(i). A variety of things can be seen in this Ni particle. EDS indicated that at the center of the particle, the concentration of Al is very low. The center of the particle is surrounded by a rim in which the Al concentration is higher and is very close to NiAl. This is followed by a region which is relatively richer in Al and has a stoichiometry close to that of Ni_2Al_3 .





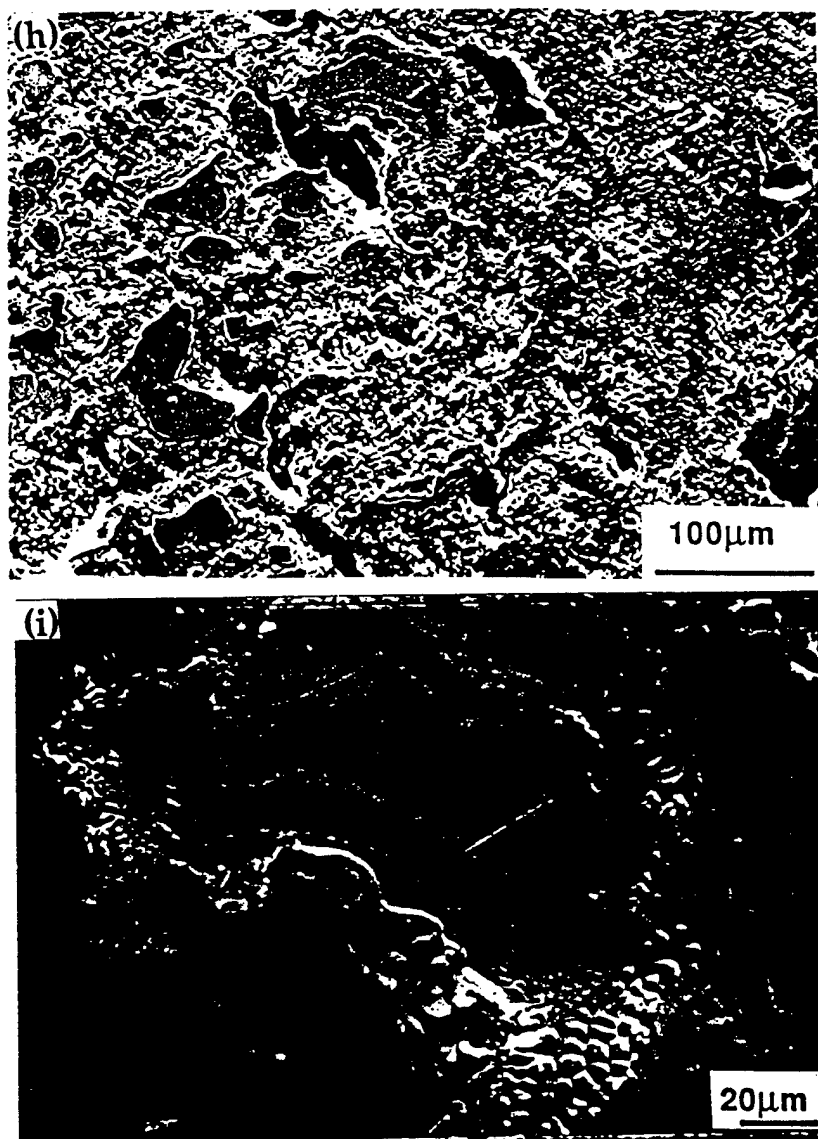


Fig. VI. 4 (a) SEM micrograph showing the powder region (left), synthesized region (right) and the stopped combustion front (indicated by an arrow) (b) SEM micrograph of the powder region (c) SEM micrograph showing the end of the partially reacted region. (d) SEM micrograph showing the microstructure towards the end of the partially reacted region (e) EDS spectrum from a region marked on the micrograph shown in (d), (f) Micrograph showing the microstructure of a region closer to the stopped reaction front (g) EDS spectrum from a region marked on the micrograph shown in (f), (h) Micrograph showing the shrinkage of the Ni cores (i) Micrograph showing a large Ni particle at the stopped reaction front.

Fully reacted region The microstructure of this region is very similar to that of the fully reacted specimen in which the combustion front has not been stopped. The size of the NiAl grains close to the front were found to be smaller than those away from the front. The reason for this difference in the grain size is the coarsening of the grains in order to minimize the grain boundary area. The grains near the front do not see any substantial coarsening because the temperature rise is lower and the cooling is faster.

Based on the aforementioned observations, the sequence of formation of the NiAl phase from the powder particles is discussed. The formation of the NiAl phase is triggered by the melting of the Al particles which then engulfs the Ni particles as well as particles of Fe, Cr and V. At first Al rich phases such as NiAl₃ and metastable phases form. The Al rich phases react with more of Ni and yield phases which are progressively richer in Ni. Ultimately as the temperature increases, Al reacts with Ni₂Al₃ and Ni to form stoichiometric NiAl. The other alloying additions do not form their aluminides, instead these get incorporated in the Al rich phases to begin with and finally end up in the NiAl phase. In their study on Ni₃Al, Lebrat et al. [104] have noticed the formation of progressively Ni rich intermetallic compound on way to the final formation of the Ni₃Al phase. In this study, the sequence of formation of the NiAl phase also involves formation of phases which are Al rich to begin with but are replaced by phases containing higher and higher amounts of Ni till the formation of NiAl occurs. This observed mechanism is similar to that observed by Lebrat et al. [104] in the case of Ni₃Al. The presence of active diluents like Fe, Cr and V does not seem to influence the basic mechanism of formation of the NiAl phase from powder particles though these diluents influence the peak temperature and the propagation velocity.

VI. 3. 2 Mechanism of Synthesis in Nb₄₅Al₁₅Ti₄₀

Nb based alloys are known to undergo rapid oxidation at high temperatures. The compacted samples of the Nb₄₅Al₁₅Ti₄₀ composition were found to be very difficult to synthesize in air. When attempts were made to synthesize the specimen in air, severe oxidation of the specimen occurred. The synthesis was therefore attempted in a quartz chamber which was first evacuated by means of a mechanical pump and later a steady flow of high purity argon was maintained in the chamber. The ignition of the sample was accomplished by heating one end of the specimen only by means of a small induction coil. Induction heating was discontinued once the synthesis wave began its propagation.

The mechanism of synthesis was established by examining the microstructure of a specimen in which only a part of the specimen had undergone micropyretic synthesis. The process of micropyretic synthesis in this alloy seems to involve two different reactions. This could be inferred from examination of the cross-sections of the synthesized specimen (Figure VI. 5). The region on top (Figure VI. 5) is referred to as region A and the region at the bottom as region B in the rest of the text. The specimen was found to undergo a reaction which swept through the entire cross-section (as seen in region B). This was followed by the second reaction which could not traverse the full cross-section because of the lack of thermal energy sufficient enough to propagate this second reaction front, thus establishing a very well defined boundary between the region which had seen two reactions (region A) and the region which had seen just one reaction (region B). The location of region A and region B within the sample is shown in the schematic of Figure VI. 6.

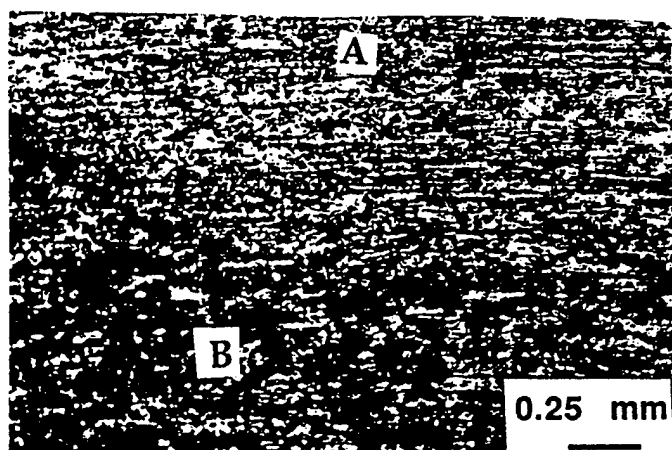


Fig. VI. 5. Cross section of the synthesized specimen showing region A and region B.

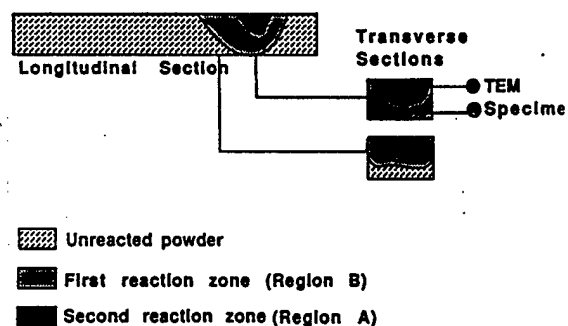


Fig. VI. 6. Schematic diagram showing the specimen and the different regions formed after synthesis.

The first reaction led to the formation of the two phases. Figures VI. 7(a) and (b) show the microstructure of region B in which only the first reaction had occurred. The presence of two distinct phases can be clearly seen in this region. The back scattered SEM image shows very sharp elemental contrast indicating the compositional difference of the two regions. EDS X-ray mapping for the elements (Figure VI. 7(c), (d) and (e)) shows that one of the phases is Nb rich and the other phase is Ti rich. Al seems to be present in both phases. The mapping also suggests that the Nb rich regions carry very little Ti and that the Ti rich regions have very little Nb. It could be inferred from the elemental X-ray mapping that the two phases are aluminides of Ti and Nb. The Nb aluminide regions seemed to form a continuous matrix. This is not surprising in view of the fact that the amount of Nb is larger in the alloy. The Ti aluminide regions were elongated grain shaped and generally had the Nb

aluminide regions inbetween. Note that the size of the Ti aluminide regions compares well with the size of the Ti powder particles used in this study. These are, therefore, aggregates of Ti grains with boundaries which can be seen in the secondary electron image (Figure VI. 7(b)). The nature of these boundaries point towards a solidification type microstructure in the alloy. The Ti aluminide regions had pores inside as well as at the boundaries with the Nb bearing regions. In comparison, the Nb aluminide regions had less pores and the pores were smaller in size.

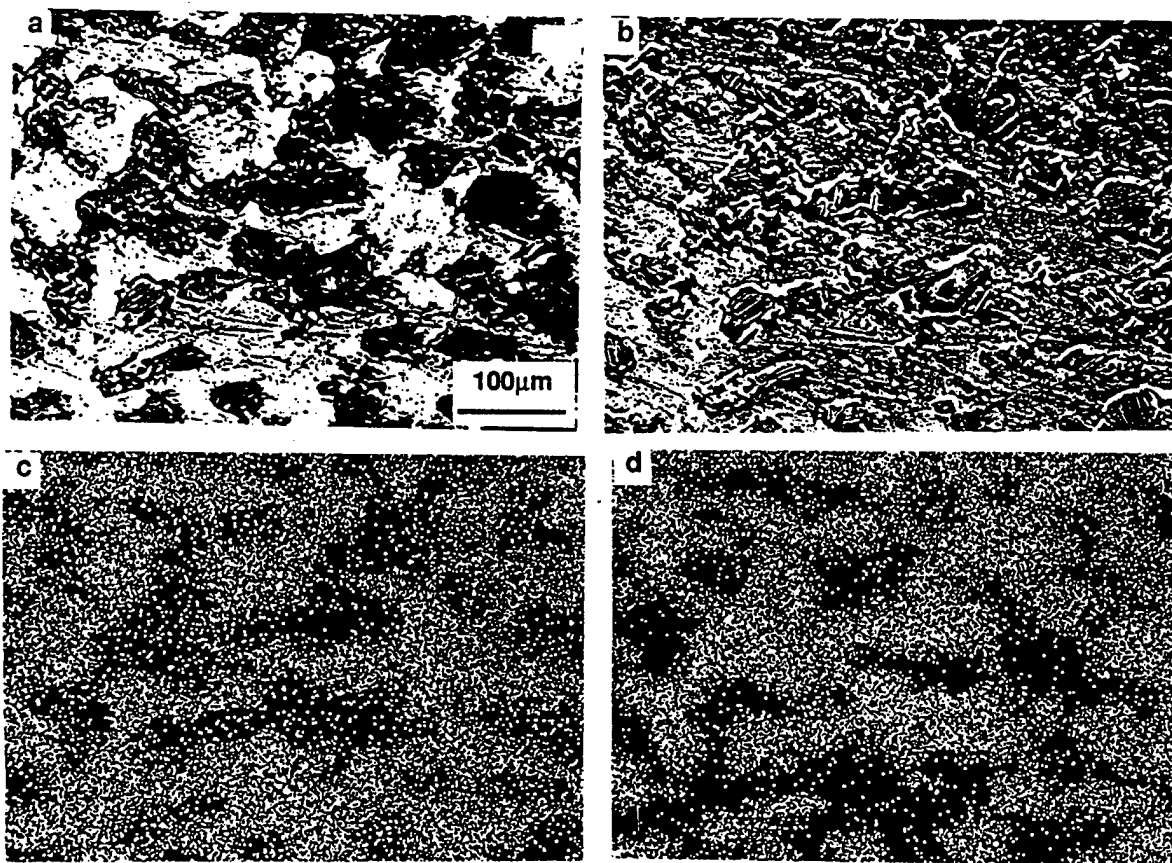


Fig. VI. 7 SEM image of a region in region B showing the Nb and Ti bearing regions, (a) backscattered image (b) Secondary electron image, (c) Nb X-ray map (d) Ti X-ray map and (e) Al X-ray map.

The backscattered electron micrograph from the region A is shown in Figure VI. 8(a). The secondary electron image, as well as the backscattered electron images from this region, gave the impression that this region has a single phase microstructure. EDS X-ray mapping (Figure VI. 8(b)-(d)) indicated that this region has a uniform distribution of the three elements, Nb, Ti and Al . The pores in this region were much larger than those observed in region B.

In order to ascertain the crystal structure of the phases, TEM studies were done on specimens made from region A and region B (Figure VI. 6). Figure VI. 9 (a) shows the TEM micrograph from the Ti rich area of region B.

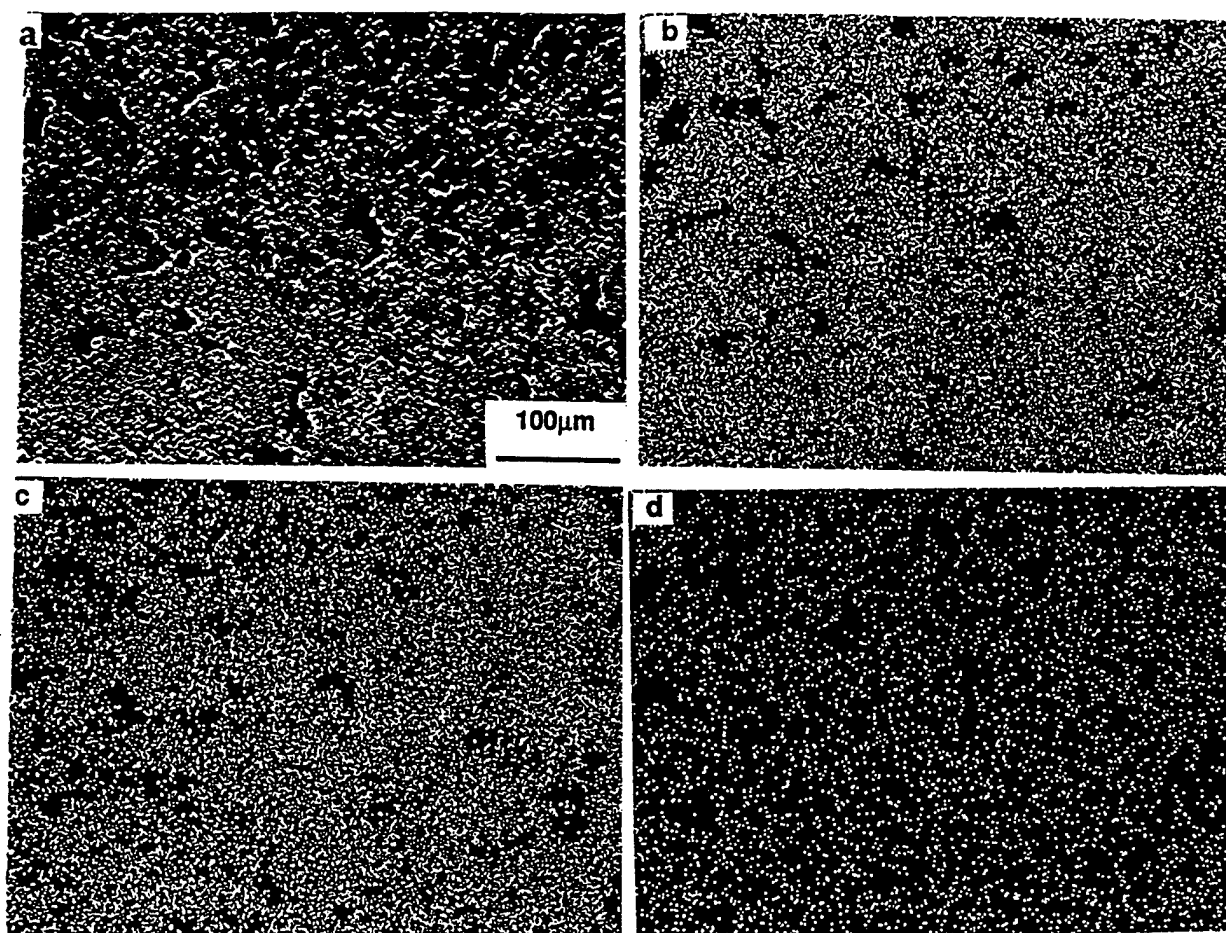


Fig. VI. 8 (a) Secondary electron image of region A, (b) Nb X-ray map, (c) Ti X-ray map and (d) Al X-ray map.

A diffraction pattern from this area is shown in Figure VI. 9(b). It is possible to index this diffraction pattern and many others from this area in terms of the Ti_3Al phase (hexagonal structure, $P6_3/mmc$, $a = 0.5775 \text{ nm}$ and $c = 0.4638 \text{ nm}$). The diffraction pattern from the adjacent grain is shown in Figure VI. 9(c). This pattern could be indexed in terms of the Nb_3Al structure (cubic structure, $Pm\bar{3}n$ (223), $a = 0.5184 \text{ nm}$).

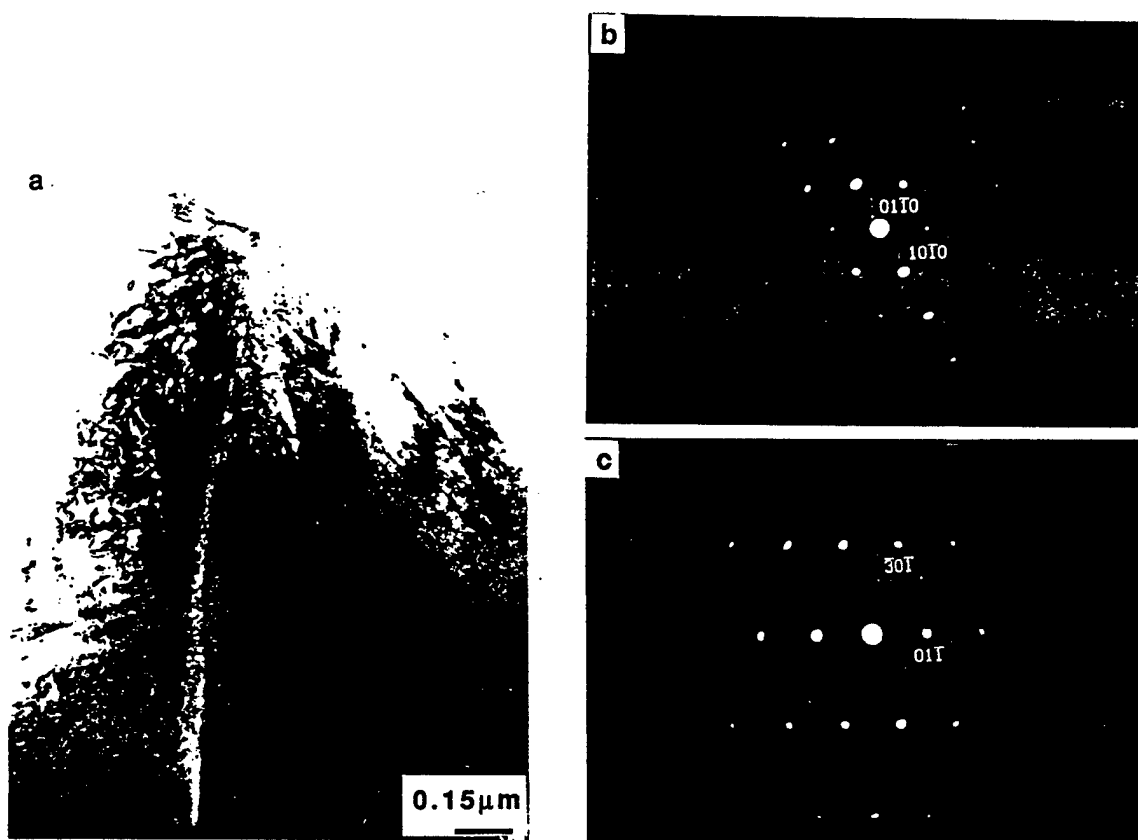


Fig. VI. 9 (a) TEM micrograph from Ti rich area in region B (b) Diffraction pattern from Ti rich area, zone axis $[0001] \text{Ti}_3\text{Al}$ (c) Diffraction pattern from the Nb rich area, zone axis $[\sim 133] \text{Nb}_3\text{Al}$.

A TEM study of region A showed the presence of a single phase alone. A diffraction pattern from this region is shown in Figure VI. 10. This pattern and many others from this region could be indexed in terms of the B2 phase with a lattice parameter $a = 0.225$ nm. This phase has been observed in this alloy in the cast and heat treated condition by other workers [1, 6]. A comparison of the microstructure of this region with the microstructure of the cast alloy indicated similarities in the composition and the structure of the phases .

The specimen in which the aforementioned studies were carried out had two boundaries demarcating different reaction zones - (1) a very sharp well defined one between region A and region B which has been investigated in considerable detail in this study and (2) a diffuse boundary between the

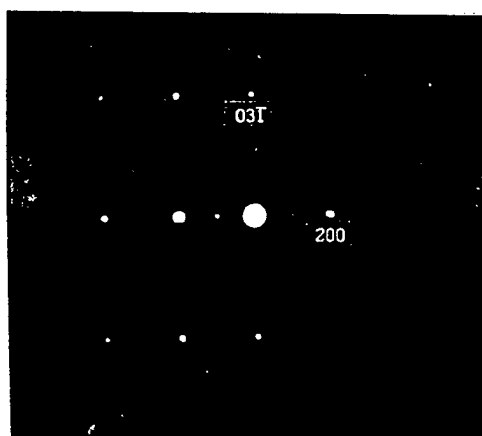


Fig. VI. 10 Diffraction pattern from region A, zone axis $[\sim 112]$ B2.

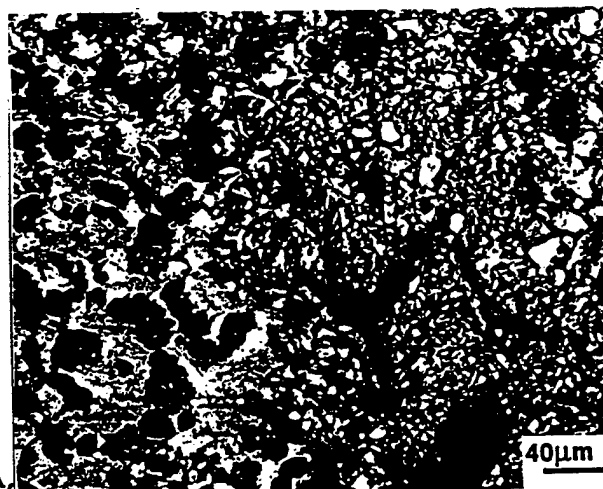


Fig. VI. 11 SEM micrograph showing the boundary between the unreacted powders and region B.

unreacted powders and region B (Figure VI. 11). The latter resulted because of the fact that the Al melted to some distance and enveloped the Ti and Nb particles leading to the formation of aluminides. A second reaction also occurred at a higher temperature to yield region A and involved the formation of the single phase due to a reaction between the two aluminide phases. The momentary and rapid heating done by the induction coil was very local. The second reaction, though exothermic, required considerable preheating which was not available in regions outside the coil. As a result, the second reaction was found to occur over a much smaller region.

VI. 4 Conclusions

The formation of the NiAl phase during micropyretic synthesis is preceded by the melting of aluminum, followed by the diffusion of Al in the solid Ni particles leading to the formation intermediate complex. The intermediate complex reacts with more Ni resulting in the formation of NiAl. The mechanism of formation of the NiAl phase is not effected by the presence of diluents like Fe, Cr and V.

During micropyretic synthesis of the composition Nb₄₅Al₁₅Ti₄₀, a single phase microstructure results on account of a two stage process- the first stage involves the melting of Al and the rapid formation of Ti and Nb aluminides. The second stage involves the formation of the single phase, with a B2 structure, formed from the reaction between Ti and Nb aluminides.

References

1. N. S. Stoloff and D. E. Alman, in *Intermetallic Matrix Composites* (edited by D. L. Anton, P. L. Martin, D. B. Miracle, and R. McMeeking), p. 31. MRS, Pittsburgh, Pennsylvania (1990).
2. M. F. Amateau and R. B. Bhagat, in *Advances in Powder Metallurgy & Particulate Materials-1992: Volume 9* (compiled by J. M. Capus and R. M. German), p. 223. MFIP/APMI, Princeton, New Jersey (1992).
3. J. A. Cornie, Y. M. Chiang, D. R. Uhlmann, A. Mortensen, and J. M. Collins, *Am. Ceram. Soc. Bull.* 65, 293 (1986).
4. Y. M. Chiang, J. S. Haggerty, R. P. Messner, and C. Demetry, *Am. Ceram. Soc. Bull.* 68, 420 (1989).
5. W. F. Frankhouser, K. W. Brendley, M. C. Kieszek, and S. T. Sullivan, *Gasless Combustion Synthesis of Refractory Compounds*. Noyes Publications, New Jersey (1985).
6. Z. A. Munir, *Am. Ceram. Soc. Bull.* 67, 342 (1988).
7. Z. A. Munir and U. Anselmi-Tamburini, *Mater. Sci. Reports* 3, 277 (1989).
8. A.G. Merzhanov, in *Combustion and Plasma Synthesis of High-Temperature Materials* (edited by Z. A. Munir and J. B. Holt), p. 1. VCH Publishers, New York (1990).
9. H. C. Yi and J. J. Moore, *J. Mater. Sci.* 25, 1159 (1990).
10. J. B. Holt and S. D. Dunmead, *Annu. Rev. Mater. Sci.* 21, 305 (1991).

11. J. Subrahmanyam and M. Vijayakumar, *J. Mater. Sci.* 27, 6249 (1992).
12. H. P. Li, S. Bhaduri, and J. A. Sekhar, *Metall. Trans.* 23A, 251 (1992).
13. H. P. Li and J. A. Sekhar, *J. Mater. Res.* 8, 2515 (1993).
14. M. G. Lakshmikantha, A. Bhattacharya, and J. A. Sekhar, *Metall. Trans.* 23A, 23 (1992).
15. M. G. Lakshmikantha and J. A. Sekhar, *Metall. Trans.* 24A, 617 (1993).
16. M. G. Lakshmikantha and J. A. Sekhar, *J. Am. Ceram. Soc.* 77, 202 (1994).
17. M. G. Lakshmikantha and J. A. Sekhar, *J. Mater. Sci.* 28, 6403 (1993).
18. C. T. Ho and J. A. Sekhar, in *High Temperature Ordered Intermetallic Alloys, IV* (edited by L. A. Johnson, D. P. Pope, and J. O. Stiegler), p. 1057. MRS, Pittsburgh, Pennsylvania (1991).
19. C. T. Ho, M. G. Lakshmikantha, and J. A. Sekhar, in *Processing and Fabrication of Advanced Materials for High Temperature Applications* (edited by V. A. Ravi and T. S. Srivatsan), p. 23. TMS, Warrendale, Pennsylvania (1992).
20. A. Bhattacharya, C. T. Ho, and J. A. Sekhar, *J. Mater. Sci. Lett.* 11, 475 (1992).
21. J. A. Sekhar, A. K. Bhattacharya, and H. P. Li, *U. S. Pat. No. 5, 110, 688*, May 5, 1992.

22. H. P. Li and J. A. Sekhar, in *Advanced Synthesis of Engineered Structural Materials* (edited by J. J. Moore, E. J. Lavernia, and F. H. Froes), p. 25. ASM International, Materials Park, Ohio (1993).
23. H. P. Li and J. A. Sekhar, *Mater. Sci. Eng. A160*, 221 (1993).
24. J. A. Sekhar, S. Bhaduri, H. P. Li, and N. S. Canarslan, U. S. Pat. No. 5, 188, 678, February 23, 1993.
25. H. P. Li, N. Prasad, J. Liu, and J. A. Sekhar, in *Processing and Fabrication of Advanced Materials III* (edited by V. A. Ravi, T. S. Srivatsan, and J. J. Moore), p. 841. TMS, Warrendale, Pennsylvania, 1994.
26. A. G. Merzhanov, *Combust. Flame* 13, 143 (1969).
27. A. P. Hardt and P. V. Phung, *Combust. Flame* 21, 77 (1973).
28. B. J. Matkowsky and G. I. Sivashinsky, *SIAM J. Appl. Math.* 35, 465 (1978).
29. S. B. Margolis, *SIAM J. Appl. Math.* 43, 351 (1983).
30. J. Puszynski, J. Degreve, and V. Hlavacek, *Ind. Eng. Chem. Res.* 26, 1424 (1987).
31. A. G. Merzhanov and B. I. Khaikin, *Prog. Energy Combust. Sci.* 14, 1 (1988).
32. R. M. German, in *Thermal Analysis in Metallurgy* (edited by R. D. Shull and A. Joshi), p. 205. TMS, Warrendale, Pennsylvania (1992).

33. Ming Fu and J. A. Sekhar, to be submitted for publication.
34. U. Anselmi-Tamburini and Z. A. Munir, in *Combustion and Plasma Synthesis of High-Temperature Materials* (edited by Z. A. Munir and J. B. Holt), p. 100. VCH Publishers, New York (1990).
35. I. P. Borovinskaya, A. G. Merzhanov, N. P. Novikov, and A. K. Filonenko, *Combust. Explos. Shock Waves* 10, 2 (1974).
36. S. Zhang and Z. A. Munir, *J. Mater. Sci.* 27, 5789 (1992).
37. A. V. Dvoryankin, A. G. Strunina, and A. G. Merzhanov, *Combust. Explos. Shock Waves* 21, 421 (1985).
38. A. V. Dvoryankin and A. G. Strunina, *Combust. Explos. Shock Waves* 27, 168 (1991).
39. K. G. Shkadinskii, B. I. Khaikin, and A. G. Merzhanov, *Combust. Explos. Shock Waves* 7, 15 (1971).
40. R. W. Rice, *J. Mater. Sci.* 26, 6533 (1991).
41. O. Odawara, J. Ikeuchi, *J. Am. Ceram. Soc.* 69, C-85 (1986).
42. O. Odawara, *J. Am. Ceram. Soc.* 73, 629 (1990).
43. Y. Miyamoto, T. Nakamoto, M. Koizumi, and O. Yamada, *J. Mater. Res.* 1, 7 (1986).
44. B. H. Rabin, *J. Am. Ceram. Soc.* 75, 131 (1992).
45. Z. A. Munir and J. B. Holt, *J. Mater. Sci.*, vol. 22, pp. 710-714, (1987).

46. E. A. Nekrasov, Y. M. Maksimov, M. K. Ziatdinov, and A. S. Shteinberg, *Combust. Explos. Shock Wave*, 1978, vol.14, pp. 575-581.
47. *Metals Handbook, vol. 7: Powder Metallurgy*, (ASM International, Materials Park, OH, 1985), pp. 296-304.
48. V. M. Shkiro, G. A. Nersisyan, I. P. Borovinskaya, *Combust. Explos. Shock Waves USSR* 14, 455 (1978).
49. H. J. Feng, J. J. Moore, and D. G. Wirth, *Metall. Trans. A* 23 A, 2373 (1992).
50. E. G. Klimchuk, K. G. Gazaryan and A. G. Merzhanov, *Combust. Explos. Shock Waves* 27, 597 (1991).
51. A. Bose, B. H. Rabin, and R. M. German, *Powder Metall. Inter.*, 20, 3, (1988).
52. S. Kumar, Ph. D. Dissertation, State University of New York, Buffalo, (1988).
53. R. Trivedi, J. A. Sekhar, and V. Seetharaman: *Metall. Trans. A*, 20A, 769 (1989).
54. Y. M. Maksimov, A. T. pak, G. B. Lavrenchuk, Y. S. Naiborodenko, and A. G. Merzhanov, *Combust. Explos. Shock Wave* 15 (4), 415 (1979).
55. R. W. Rice, G. Y. Richardson, J. M. Kunez, T. Schroeter and W. J. McDonough; *Advanced Ceramic Mater.*, 2, 222 (1987) .
56. S. C. Singhal , *J. of Mat. Sci.*, 11, 500 (1976).

57. H. P. Li, S. Bhaduri, and J. A. Sekhar, "Processing Ti-B-Cu Composites by Combustion Synthesis", *Processing and Fabrication of Advanced Materials for High Temperature Applications*, ed. V. A. Ravi and T. S. Srivatsan, (Warrendale, PA: The Minerals, Metals & Materials Society, 1992) 45-59.
58. M. Dollar, S. Dymek, S. J. Hwang, and P. Nash, *Metallurgical Transactions A*, 24A (1993).
59. E. P. Busso and F. A. McClintock, *Acta Metall. Mater.* 42,3263 (1994).
60. R. Jayram and M. K. Miller, *Acta. Metall. Mater.* , 42, 1561 (1994).
61. A. R. C. Westwood, *Metall. Trans. A*, 19A, 749 (1988).
62. R. D. Field, D. F. Lahman and R. Darolia, *Acta. Metall. Mater.*, 39, 2951(1991).
63. T. Hong and A. J. Freeman, *Phys. Rev. B*43, 6446 (1991).
64. D. F. Lahrman, R. D. Field and R. Darolia, *High Temperature Ordered Intermetallic Alloys IV*, ed. L.A. Johnson, et al., p. 603, MRS, Pittsburgh (1991).
65. R. D. Field, D. F. Lahrman and R. Darolia, *Acta. Metall. Mater.*, 39, 2961 (1991).
66. H. P. Li and J. A. Sekhar, *J. Mater. Res.*, 10, 2471 (1995).
67. H. P. Li and J. A. Sekhar, *J. Mater. Sci.*, 8, 2515 (1995).

68. G. K. Bansal and W. H. Duckworth, *Fracture Mechanics Applied to Brittle Materials*, ASTM STP 678, p. 38, American Society for Testing and Materials, (1979).
69. R. D. Noebe, R. R. Bowman, and M. V. Nathal, *International Materials Reviews*, 38, 193 (1993).
70. K. S. Kumar, S. K. Mannan and R. K. Viswanadham, *Acta. Met. Mat.*, 40, 1201 (1992).
71. R. W. Rice, *Ceramic Engineering and Science*, 7-8, 589 (1985).
72. G. Sauthoff, *Intermetallic Compounds*, Vol. 1, p. 911, John Wiley, New York, (1994).
73. S. Chakravorty and C. M. Wayman, *Metall. Trans.* 7A, 555 (1976).
74. C. B. Franks, *Phil. Mag.*, 29, 375 (1980).
75. G. K. Dey and J. A. Sekhar, unpublished work.
76. M. H. Loretto and R. J. Wasilewski, *Philos. Mag.*, 23, 1311 (1971).
77. R. Darolia, D. Lahrman and R. Field, *Scripta. Met. Mater.*, 26, 1007 (1992).
78. P. Veyssiere and R. Noebe, *Phil. Mag.*, 65, 1 (1992).
79. J. D. Cotton, Ph. D thesis, University of Florida, 1991.
80. S. M. Merchant and M. R. Notis, *Mater. Sci. Eng.*, 66, 47 (1984).

81. D. K. Patrick, K. M. Chang, D. B. Miracle, and H. A. Lipsitt in "High Temperature Ordered Intermetallic Alloys IV, (ed. L. Jhonson et al.) Mater. Res. Soc. Symp. Proc., 213, 267 (1991).
82. S. Guha, P. R. Munro and I. Baker, Mater. Sci. Eng., A131, 27 (1991).
83. J. D. Cotton, M. J. Kaufman and R. D. Noebe, Scr. Met. Mat., 25, 1827 (1991).
84. C. S. Jayanth, M. S. Thesis, Illinois Institute of Technology, (1983).
85. T. Hong and A. J. Freeman, in High Temperature Ordered Intermetallic Alloys III, (ed. C. T. Liu et al.) Mater. Res. Soc. Symp. Proc., 133, 75 (1989).
86. J. D. Cotton, M. J. Kaufman, R. D. Noebe and M. Bhebehani, in 'HITEMP Review - 1991', NASA CP-10082, 23 (1991).
87. D. J. Gaydosch and M. A. Crimp, "High Temperature Ordered Intermetallic Alloys IV", (ed. C. C. Koch et al.) Mat. Res. Soc. Symp. Proc., 39, 429 (1984).
88. V. Gupta, M S Thesis, University of Cincinnati, (1995).
89. E. S. K. Menon, P. R. Subramanian and D. M. Dimiduk, Scr. Met. Mat., 27, 265 (1992).
90. E. R. Slaughter and S. K. Das, Proc. of Second International Conference on Rapid Solidification Processing, Claitor's Publ. Div., Baton Rouge, LA , p. 354 ((1980).
91. C. T. Liu and C. L. White, Scripta Met., 20, 1613 (1986).

92. G. K. Dey and J. A. Sekhar, Communicated to Metallurgical and Materials Transactions.
93. G. K. Dey and J. A. Sekhar, unpublished work.
94. E. P. George and C. T. Liu, J. Mater. Res., 5, 754 (1990).
95. J. Shyue, D-H Hou, M. Aindow and H. Fraser, Mater. Sci. Engg., A170, 1 (1993).
96. K. Yasuda, T. Fujiwara, H. Kodoma and M. Suwa, High Temperature Ordered Intermetallic Alloys IV, MRS Proc. Vol. 213, p. 865, Materials Research Society, Pittsburgh, PA, (1991).
97. H. Kohmoto, J. Shyue, M. Aindow and H. L. Fraser, Scripta Metall. et Materialia, 29, 1271 (1993).
98. J. Shyue, D-H Hou, S. Johnson, M. Aindow and H. Fraser, High Temperature Ordered Intermetallic Alloys IV, MRS Proc. Vol. 288, p. 573, Materials Research Society, Pittsburgh, PA, (1993).
99. Powder Diffraction File, Alphabetical Indexes, International Center for Diffraction Data, (1994).
100. Pearson's Handbook of Crystallographic Data for Intermetallic Phases, P. Villars and L. D. Calvert, American Society for Metals, Metals Park, (1992).
101. S. Reuss and H. Vehoff, in " Intermetallische Phasen Strukturwerkstoffe fur Hohe Temperaturen, (ed. F. J. Bremer), Forschungszentrum Julich GmbH, 1991, 65 (1991).

102. W. A. Kaysser, R. Laag, J. C. Murray, and G. E. Petzow, *Int. J. Powder Metall.*, 27, 43 (1991).
103. M. P. Brady, R. J. Hanrahan, Jr., and E. D. Verink, Jr., *Processing and Fabrication of Advanced Materials for High Temperature Applications* - II, V. A. Ravi and T. S. Srivatsan, *The Minerals, Metals & Materials Society*, p 419 (1993).
104. J. P. Lebart, A. Varma and P. J. McGinn, *J. Mater. Res.*, 9, 1184 (1994).
105. G. K. Dey and J. A. Sekhar, communicated to *Scripta Metallurgica et Materialia*.